Electroactive Nanoarrays for the Biospecific-Ligand Mediated Study of Single Cell Adhesion and Polarization

Diana Kay Hoover

A dissertation submitted to the faculty of the University of North Carolina at Chapel Hill in partial fulfillment of the requirements for the degree of Doctor of Philosophy in the Department of Chemistry (Analytical Chemistry).

Chapel Hill
2009

Approved by,

Advisor: Professor Muhammad N. Yousaf
Chair: Professor Mark H. Schoenfisch
Professor Michel R. Gagné
Professor Marcey L. Waters
Professor R. Mark Wightman

Abstract

Diana Kay Hoover: Electroactive Nanoarrays for the Biospecific-Ligand Mediated
Study of Single Cell Adhesion and Polarization
(Under the direction of Prof. Muhammad N. Yousaf)

Cell adhesion, polarization, and migration are vital to numerous biological

phenomena. Therefore, a greater understanding of the mechanisms of these

processes will have broad impacts in fields ranging from developmental biology to

medicine. This work has focused on developing a nanoscale model system that will

allow one to study the effect of the spatial presentation of immobilized ligands on the

nanoarchitecture of adherent cells.

In Chapter 2, the development of electroactive nanoarrays of hydroquinone-

terminated alkanethiol, produced by dip-pen nanolithography (DPN) is described.

These nanoarrays, in conjunction with an oxime-chemistry based chemoselective

immobilization strategy and high-resolution fluorescence microscopy, were used to

study biospecific-ligand mediated single cell adhesion. The difference in ligand

affinity of linear and cyclic Arg-Gly-Asp (RGD) was shown to have a dramatic affect

on the intracellular nanoarchitecture of adherent fibroblasts.

The production of asymmetric nanoarrays used to study single cell polarization is

described in Chapter 3. Asymmetric nanoarrays presenting linear RGD were found

to induce net directional cell polarization in adherent fibroblasts, while linear RGD-

presenting symmetric nanoarrays did not induce net polarity. This demonstrates a direct correlation between the spatial distribution of cell adhesive ligand and the establishment and maintenance of directional cell polarization. In addition, there was no net directional cell polarity found on asymmetric nanoarrays presenting a higher affinity ligand cyclic RGD, indicating that ligand affinity also has a profound effect on cell polarization. The relationship between ligand affinity and spatial distribution of immobilized ligand was further explored through double asymmetric nanoarrays presenting cyclic RGD, which were shown to impose directional cell polarization.

In order to extend this methodology to examine other aspects of cell adhesion and polarization on electroactive nanoarrays other methods of visualization were considered. There have been conflicting reports regarding the use of total internal reflection fluorescence microscopy (TIRFM) to visualize cells near thin metal layers. In Chapter 4, it was determined that TIRFM is an effective method to examine intercellular structures of cells adhered to patterned SAMs on gold surfaces. This was demonstrated through the use of microcontact printing and DPN patterning methods. Future applications of this research are presented in Chapter 5.

To Jack Morningstar (Pappy Jack) who taught me the value of hard work and education. Thank you "Great" - I miss you every day.

&

To Amanda, for showing how much a positive attitude in the face of adversity can make a difference. You are an inspiration.

ACKNOWLEDGEMENTS

First I would like to thank Dr. Muhammad Yousaf for allowing me the opportunity to research in his lab. Without his guidance, I would not be where I am today. I am also indebted to the past and present members of the Yousaf group. Graduate school is a road best walked with friendly company – thank you all and best of luck!

I would like to thank Dr. Susan Deupree and Laurel Averett of the Schoenfisch research group, Dr. Ryan Fuierer of Asylum Research, and Dr. Erika Pearson and Vanessa DeRocco of the Erie research group for their expertise and helpful discussions in the completion of my dissertation research.

I am also grateful to the professors in the chemistry department at Edinboro University of Pennsylvania, for their continued support and advice. Thank you to Drs. Naod Kebede, Nancy S. Mills, Monica Valentovic, and Tom Guetzloff for introducing me to research. Thank you to all who have supported my career goals.

I have to thank my family and friends for the love, support, patience, and perspective they have shown throughout my academic career. I would like to especially thank my parents, Donald and Peggy Hoover. They have always supported me in every endeavor, and have taught me that the traditional yardsticks of success are not always the most important in life. I would not have made it this far without such a support system. I hope you enjoy the final product.

"Cells die, scientists rejoice."

TABLE OF CONTENTS

LIST OF SCHEMES

LIST OF FIGURES

LIST OF ABBREVIATIONS

~	approximately
Å	Ångström(s)
δ	chemical shift (NMR)
λ	wavelength
μm	micrometer(s)
θ_i	incident angle
θ_c	critical angle
AFM	atomic force microscope
Ag/AgCl	silver / silver chloride reference electrode
AIBN	2,2'-azobisisobutyronitrile
AOAA	(aminooxy) acetic acid (also known as *O*-(carboxymethyl)-hydroxylamine hemichloride)
aq	aqueous
BBr_3	boron tribromide
Boc	butyloxycarbonyl
°C	degree(s) Celsius
CCD	charge coupled device
$CDCl_3$	deuterated chloroform
CO_2	carbon dioxide
cm	centimeter(s)
CRP	cysteine rich protein

C_{16}-SH	hexadecanethiol
CV	cyclic voltammetry (or voltammogram)
Cy-2	cyanine 2 dye
d	evanescent wave depth of penetration
Da	dalton(s)
DAPI	4',6-diamidino-2-phenylindole dihydrochloride
DCM	dichloromethane
DIEA	N,N-diisopropylethylamine
DMEM	Dulbecco's modified Eagle's medium
DMF	dimethylformamide
DPN	dip-pen nanolithography
ds (in NMR characterization)	doublet of singlets
ECM	extracellular matrix
e.g.	*exempli gratia,* "for example"
EG_4-C_{11}-SH	23-mercapto-3,6,9,12-tetraoxatricosan-1-ol
eq.	equivalents
ESI+	positive electrospray ionization source
et al.	*et alii,* "and others"
etc.	*et cetera,* "and so forth"
EtOAc	ethyl acetate

EtOH	ethanol
FAK	focal adhesion kinase
FITC	fluorescein isothiocyanate
Fmoc	9-fluorenylmethoxycarbonyl
Fmoc-Arg(Pbf)-OH	N-α-Fmoc-N^G-(2,2,4,6,7-pentamethyl-dihydrobenzofuran-5-sulfonyl)-L-arginine
Fmoc-Asp(OtBu)-OH	N-α-Fmoc-L-aspartic acid β -t-butyl ester
Fmoc-Gly-OH	N-α-Fmoc-glycine
Fmoc-Ser(tBu)-OH	N-α-Fmoc-O-t-butyl-L-serine
g	gram(s)
^{1}H NMR	proton nuclear magnetic resonance spectroscopy
HBTU	O-benzotriazole-N,N,N',N'-tetramethyl-uronium-hexafluorophosphate
HCl	hydrochloric acid
$HClO_4$	perchloric acid
H_2O	(distilled) water
H_2O_2	hydrogen peroxide
H_2Q-C_{11}-SH	11-(2,5-dihydroxylphenyl)-1-mercaptoundecane
h	hour(s)
H_2SO_4	sulfuric acid
Hz	Hertz (second^{-1})

I	intensity
i.e.	*id est,* "that is"
IgG	immunoglobulin G
ILK	integrin-linked kinase
J	J coupling constant
K_d	dissociation constant
kW	kilowatt(s)
LFM	lateral force microscopy
LIM	cysteine-rich protein structural domains
m	meter(s)
m (in NMR characterization)	multiplet
M	molar
MeOH	methanol
mg	milligram(s)
MHz	megaHertz
min	minute(s)
mL	milliliter(s)
mm	millimeter(s)
mM	millimolar
mmol	millimole(s)
mol	mole(s)
MS	mass spectrometry
mV	millivolt(s)

n	refractive index
N	Newton(s)
N_2	molecular nitrogen
NA	numerical aperture
NaOH	sodium hydroxide
Na_2SO_4	sodium sulfate
nm	nanometer(s)
nM	nanomolar
q (in NMR characterization)	quartet
QQQ	triple quadrupole mass spectrometer
PBS	phosphate buffered saline
PDMS	polydimethylsiloxane
RGD	arginine-glycine-aspartic acid tripeptide
RT	room temperature (~25 ℃)
s	second(s)
s (in NMR characterization)	singlet
SAM(s)	self-assembled monolayer(s)
Src	family of proto-oncogenic tyrosine kinases
t (in NMR characterization)	triplet
TFA	trifluoroacetic acid
THF	tetrahydrofuran

TIR	total internal reflection
TIRFM	total internal reflection fluorescence microscopy
TIPS	triisopropylsilane
TRITC	tetramethylrhodamine B isothiocyanate
UV	ultraviolet
vs.	versus
v:v	volume to volume ratio

CHAPTER 1

INTRODUCTION: BIOLOGICAL SIGNIFICANCE OF CELL ADHESION, POLARIZATION, AND MIGRATION

1.1 Influence of Cell Adhesion, Polarization, and Migration *in vivo*

1.1.1 Eukaryotic cells in vivo: the extracellular matrix. In nature, eukaryotic cells exist in a complex environment known as the extracellular matrix (ECM). The ECM is composed primarily of two main classes of biomacromolecules: fibrous proteins (*e.g.* fibronectin, collagen, fibrinogen, elastin, and laminin) and proteoglycans (*e.g.* glycosaminoglycans covalently bound to proteins). The ECM is permeable to small molecules and also provides mechanical strength to connective tissues. This complex matrix is mainly secreted and organized by the cells growing within it. For example, in mammalian connective tissues most of the ECM is produced and maintained by a cell type known as fibroblasts.[1,2]

In order to undergo vital biological functions such as embryogenesis, differentiation, and proliferation, the cell must first adhere to the underlying ECM.[3,4] Cell adhesion and migration are also central in normal tissue repair processes including the immune response,[5-7] wound healing,[8-10] and angiogenesis.[11] Moreover, improper cell adhesion and migration has been implicated in disease states, such as cancer cell metastasis.[12,13] Therefore, a greater understanding of the mechanisms of cell adhesion, polarization, and migration will have broad impacts in fields as diverse as medicine and developmental biology.

1.1.2 Directed eukaryotic cell migration. In order for cells to undergo directional migration a complex series of events must take place. These actions can be grouped into three major categories: adhesion, polarization, and migration. First, the cell surface receptors must recognize and adhere to components of the ECM. Then, the cell must interpret both external and internal signals in order to "choose" a direction to migrate. Finally, the cell can begin migration by forming extensions of the leading edge of the cell membrane while releasing contacts in the rear of the cell body.[14-16] There are a multitude of factors that influence this process, thereby creating an intricate network of interactions. As a consequence, the exact mechanism of directional cell migration is still an area of active study.[17-19] A more thorough description of cell adhesion will be presented in Section 1.2, and a discussion of cell polarization will be offered in Chapter 3.

1.2 Cell Adhesion: Focal Adhesion Formation

1.2.1 The role of integrin receptors in cell adhesion. As previously mentioned, in order to migrate a cell must first adhere to ligands presented in the ECM. While numerous cell surface receptors are known, the integrin family of cell surface receptors is key in cell – ECM interactions. Since the identification of the integrin family of cell-surface receptors in the late 1980s,[20,21] there has been keen interest in the study of integrin receptor – ligand interactions.

1.2.2 The structure of integrin receptors. Integrin receptors are heterodimeric transmembrane glycoproteins that are composed of α and β subunits. Currently, there are 18 α and 8 β known subunits in mammals, which selectively combine in

the form $\alpha\beta$. It is interesting to note that, based on the number of α and β subunits known, there are nearly 150 permutations possible, yet there have been only 24 distinct integrin receptors identified to date. This is partially due to the fact that the α and β subunits that have been identified are not all expressed in the same manner – some are expressed universally, while others are more restricted to certain tissue types or developmental stages of the organism.[22,23]

The extracellular domains of integrin receptors recognize a wide range of ECM components, as well as some divalent cations.[24] Some of the specific peptide sequences responsible for integrin receptor recognition of ECM components have been identified, while many others are still unknown. The short peptide sequence Arg-Gly-Asp-Ser (RGDS) was identified as a binding motif in several ECM components including fibronectin, fibrinogen, vitronectin, laminin, and some collagens. It was later discovered that the minimum sequence necessary to promote cell adhesion was RGD, with some flexibility allowed in the fourth amino acid position.[25,26] Approximately half of the known integrin receptors recognize the RGD sequence when binding to ECM ligands.[27]

1.2.3 Focal adhesion structure. The individual affinity of an integrin receptor ligand pair is quite low ($K_d = 10^{-6}$ to 10^{-7}).[28] Therefore, a number of integrin receptors must cluster together in order to create a strong enough interaction between the cell surface and the surrounding ECM to promote adhesion. During the clustering process a wide range of intracellular proteins are recruited in order to produce a physical connection between the filamentous actin fibers of the cytoskeleton and the ECM through the cytoplasmic tails of the integrin receptor subunits. This large,

dynamic collection of proteins is known as a focal adhesion. A representative diagram of a focal adhesion is shown in Figure 1.1.

At least 50 distinct proteins have been identified in focal adhesions.[29] Actin, α-actinin, filamin, talin, tensin and vinculin have all been identified as serving a structural role in focal adhesions,[30] while some LIM-domain containing proteins (*e.g.* paxillin, CRP, and zyxin), as well as many enzymes (*e.g.* ILK, FAK, and Src enzymes) have been shown to exhibit regulatory functions.[31,32] In the past three decades many research groups have worked to identify the multitude of interactions within focal adhesions.

The term "focal adhesion" will be used within this dissertation to describe the cluster of proteins that are visualized through fluorescence immunocytochemistry staining for the adaptor protein paxillin. Paxillin is known to be present in mature focal adhesions.[33] There are currently four distinctions used to describe cell-matrix adhesions in the literature. These categories are based, in part, on the dynamics of the protein cluster, the morphology exhibited, and the cell type under investigation. The first, most transient cell-matrix contact is known as a focal complex; small (~100 nm), dot-like structures found in migrating cells. Focal complexes will either experience rapid turnover, or will mature to focal adhesions (also known as focal contacts). Focal adhesions are larger (~100 μm), more established cell – matrix contact points typically found in cells with lower motility. The third category is a subset of focal adhesions known as fibrillar adhesions that are characterized by the arrangement of ECM proteins in relation to the intercellular focal adhesion structures.[34-36] Finally, in some specialized cell lines (*e.g.* osteoblasts and
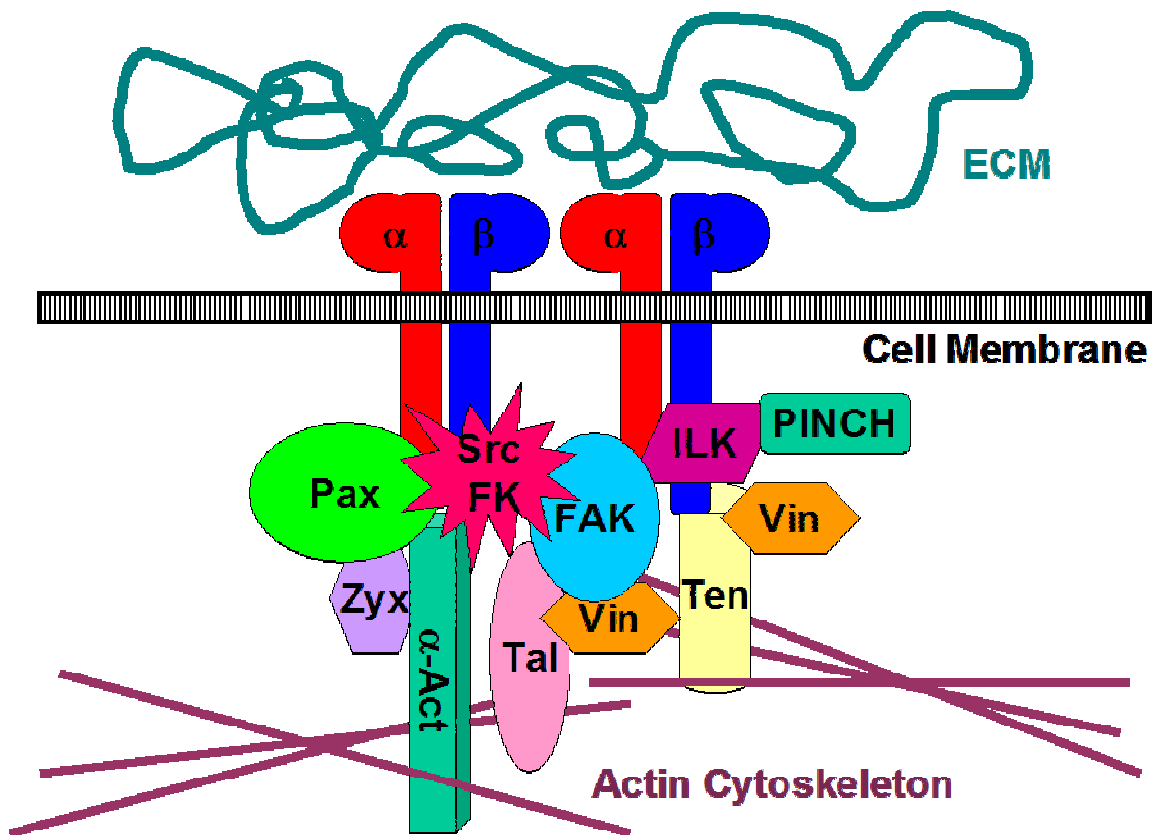
Figure 1.1   Simplified diagram of focal adhesion structure (not drawn to scale). Some selected focal adhesion proteins include integrin receptor heterodimers (individual subunits designated by α and β), α -actinin (α-Act), focal adhesion kinase (FAK), integrin-linked kinase (ILK), paxillin (Pax), particularly interesting new Cys-His protein (PINCH), Src-family kinases (Src FK), talin (Tal), tensin (Ten), vinculin (Vin), and zyxin (Zyx). Of note is paxillin (Pax), the protein that will be used as a marker for focal adhesions in Chapters 2, 3, and 4.

neutrophils) the cell-matrix adhesion structures are known as podosomes.[37]

1.3 Current Methods Used to Study Cell Adhesion, Polarization, and Migration

As was previously described in Section 1.2.3, a number of biospecific interactions between extracellular ligands and cell surface receptors are required for cell adhesion and migration. The molecular level process of focal adhesion formation, and its subsequent influence on the organization of the intercellular nanoarchitecture, is an area of intense investigation. It has been recognized for several years that nanoscale clustering of integrin receptors are important for cell adhesion and migration.[38,39] However, the understanding of the mechanisms within these processes remains elusive due to the lack of nanoscale, molecularly well-defined model substrates.[40] The following subsections will describe several examples of micro- and nanoscale model systems that have been employed to study cell adhesion.

1.3.1 Microscale cell adhesion studies: cell culture surfaces coated with adsorbed ECM proteins. One of the most commonly employed methods to study cell adhesion is the use of flat surfaces (often glass or polystyrene cell culture dishes) that are coated with an ECM protein (*e.g.* collagen, fibronectin, laminin, or vitronectin). Cells are then added, allowed to adhere, migrate, grow, or differentiate, depending on the cell type under study.[41] For example, this methodology has been used to investigate the formation of focal adhesion in osteoblasts on a variety of substrata, including glass and titanium coated with fibronectin or serum.[42]

1.3.2 Microscale cell adhesion studies: microcontact printing. Microcontact printing has been used to pattern self-assembled monolayers (SAMs) on metal thin film metal surfaces for cell biology studies for the past decade. Microcontact printing involves the transfer of an "ink" solution (*e.g.* hydrophobic alkanethiolate solutions) from an elastomeric stamp to a surface (*e.g.* thin films of gold and silver). The background areas of metal can be passivated by the adsorption of poly(ethylene glycol) (PEG)-terminated alkanethiolates. Proteins (*e.g.* fibronectin and vitronection) can then be adsorbed and cell adhesion is observed through immunostaining and microscopy.[43] Microcontact printing has been used to pattern single cells in various geometries,[44] as well as producing micropatterned substrates presenting ≤ 1 μm^2 patches of fibronectin to study cell spreading.[45]

1.3.3 Nanoscale cell adhesion studies: fibronectin patterned by nanosphere lithography. Recently, Slater and Frey have used nanosphere lithography to produce arrays of gold "nanoislands" with diameters of 90 − 400 nm. Silica spheres are deposited in mono- or bilayers on a glass substrate and then gold is thermally evaporated onto the surface. Following removal of the spheres through sonication, the patterned gold "nanoislands" can be functionalized by immersion in alkanethiolate solutions. Silane-based PEG passivates the remaining bare areas of glass. The size and spacing of the "nanoislands" can be controlled by the diameter of silica spheres used, as well as the configuration of the mono- and bilayers. The authors adsorbed intact fibronectin on the "nanoislands" and observed the influence of the lateral spacing of adhesive patches on cell adhesion.[46]

1.3.4 Nanoscale cell adhesion studies: comb polymers presenting clusters of

RGD ligands. It has been recognized in the field of biomaterials development that cellular responses to an engineered surface may vary widely based on the spatial distribution of biospecific ligands. Griffith *et al.* have developed comb copolymers of methyl methacrylate and poly(oxyethylene) methacrylate (P(MMA-*r*-POEM)) that can be modified through conjugation chemistry to present RGD peptides. By combining modified and non-modified combs, nanoclusters of RGD ligands can be presented on a background that is resistant to non-specific protein and cell adhesion, due to the poly(oxyethylene) methacrylate combs. Thin films of the comb copolymers were produced on glass or polystyrene cell culture materials, and cell adhesion behavior was studied. It was found that the nanoscale clustering of RGD ligands on the polymer thin films was able to support cell adhesion. This platform has also been investigated as a possible route to three dimensional tissue scaffolds.[47,48] The presentation of RGD ligands on these comb polymer surfaces can be partially controlled by adjusting the amount of modified comb polymer added, the degree to which that comb is modified with ligand, and the molecular weight of the comb polymer.

    1.3.5 Nanoscale cell adhesion studies: patterned gold nanoparticles presenting RGD ligands. Spatz and co-workers have developed a method to study the effects of spatial distribution of cell adhesive ligands on cell adhesion, spreading, and migration based on the self-assembly of diblock copolymer micelles containing gold nanoparticles. A diblock copolymer (polystyrene-*block*-poly[2-vinylpyridine $(HAuCl_4)_{0.5}$]) is first deposited on a glass surface. After the polymer background is removed *via* plasma treatment, nearly uniform arrangements of gold nanoparticles

remain on the surface. The gold nanoparticles are then functionalized with thiol-terminated cyclic RGD peptides, while the areas between nanoparticles are passivated using PEG. The authors have theorized that the diameter of the gold nanoparticles (typically 5 – 8 nm) coincide with the reported size of a single integrin receptor heterodimer based on published crystallography data. Through this work, Spatz *et al.* have reported that the optimal lateral spacing between integrin receptors to be approximately 60 nm, based on focal adhesion formation as shown through immunostaining and the observation of cell spreading and migration rates through live cell microscopy.[49-51] These reports are among the first to study the effects of the spatial presentation of cell adhesive ligands with some control over the orientation of the immobilized ligand.

1.3.6   Nanoscale cell adhesion studies: dip-pen nanolithography and protein adsorption. Since the introduction of dip-pen nanolithography (DPN) in the late 1990s,[52] there have been several studies using this powerful technique to directly pattern biologically relevant molecules, including ECM proteins[53] and antibodies.[54, 55] However, there has been a significant lack of studies using DPN-generated surfaces for cell adhesion studies. Mirkin, Mrksich, and co-workers reported a proof-of-concept study based on protein nanoarrays produced by DPN. In this work, hexadecanethiol is patterned in nanoarrays of dots (200 nm diameter, 700 nm pitch, total patterned area of 6400 μm^2). A fusion protein based on the ECM protein fibronectin is then adsorbed to the nanoarrays, and fibroblasts are seeded to the surface.[56] This report is significant in that it is the first to report the adhesion of cells to nanoarrays created using DPN.

1.3.7 Potential downfalls of previous methods used to study cell adhesion, polarization, and migration. Each of the previously mentioned micro- and nanoscale patterning techniques do offer a variety of advantages. For example, using ECM coated cell culture dishes and microcontact printing is both affordable and easily accessible for many research groups. However, both of these methods lack well-defined interactions between the cells and the model substrate. It is known that cells have a great impact on the organization of the surrounding ECM. Following adhesion, the cells patterned on fibronectin or other ECM proteins will rearrange the orientation of the presented ligands, thus changing the interactions between the cell and the model substrate.[1] In the case of ECM coated substrates, cell-cell interactions will also likely influence the behavior of single cells.

Several of the nanoscale methods addressed some of these limitations by patterning single, biospecific ligands. Ultimately, there was little control over the exact orientation and distribution of cell adhesive ligands on the surface in these methods. The work of Mirkin, Mrksich, *et al.* showed promise by using DPN® to control the location of ligands at the nanoscale. However, the use of retronectin as the cell adhesive ligand presented caused ill-defined interactions between the cells and the surfaces, such that there were multiple interactions occurring through a variety of cell surface receptors. Also, the use of only optical microscopy excluded the observation of the effects of the nanoscale presentation of ligands on the internal nanoarchitecture of the adherent cells. The focus of my dissertation research is aimed at developing a nanoscale model system for cell adhesion and polarization that addresses these limitations, as described below.

1.4 Significance and Goals of this Research

Several examples of the many efforts made to design a nanoscale model system to study cell adhesion and migration were described in Section 1.3. My dissertation research has focused on developing a nanoscale model surface that will allow the study of the effect of the spatial presentation of immobilized ligands on the nanoarchitecture of adherent cells. I propose that such a model substrate must meet several criteria. First, the feature sizes of the ligands must be in the nanometer regime. Next, the spatial distribution of immobilized ligands must be precisely defined. In addition, the interactions between the cell surface receptors and the immobilized ligands of interest must be biospecific. Finally, the substrate must be compatible with cell culture and high-resolution fluorescence microscopy.

Chapter 2 will describe the model system and nanopatterning method chosen and the development of symmetric electroactive nanoarrays to study single cell adhesion.[57] In Chapter 3 the extension of this technology to the development of asymmetric electroactive nanoarrays in order to induce and observed single cell polarization will be presented.[58] The goal of Chapter 4 is to discuss proof-of-principle experiments demonstrating the use of total internal reflection fluorescence microscopy to study cell adhesion on nanopatterned surfaces.[59] The summary, conclusions, and future directions of this work will be discussed in Chapter 5.

REFERENCES

(1)   Alberts, B.; Johnson, A.; Lewis, J.; Raff, M.; Roberts, K.; Walter, P. *Molecular Biology of the Cell;* Garland Science: New York, **2002**.

(2)   Rhodes, J. M.; Simons, M. The extracellular matrix and blood vessel formation: not just a scaffold. *J. Cell Mol. Med.* **2007**, *2,* 176-205.

(3)   Huttenlocher, A.; Sandborg, R. R.; Horwitz, A. E. Adhesion in cell migration. *Curr. Opin. Cell Biol.* **1995**, *7,* 697-706.

(4)   Halbleib, J. M.; Nelso, W. J. Cadherins in development: cell adhesion, sorting, and tissue morphogenesis. *Genes & Dev.* **2006**, *20,* 3199-3214.

(5)   Hogg, N. Row, row, row your leucocyte gently down the vein... *Immunol. Today* **1992**, *13,* 113-115.

(6)   Hogg, N.; Landis, R. C. Adhesion molecules in cell interactions. *Curr. Opin. Immunol.* **1993**, *5,* 383-390.

(7)   Cyster, J. G. Homing of antibody secreting cells. *Immunol. Rev.* **2001**, *194,* 48-60.

(8)   Raghow, R. The role of extracellular matrix in postinflammatory wound healing and fibrosis. *FASEB J* **1994**, *8,* 823-831.

(9)   Mutsaers, S. E.; Bishop, J. E.; McGrouther, G.; Lauret, G. J. Mechanisms of tissue repair: from wound healing to fibrosis. *Int. J. Biochem. Cell Biol.* **1997**, *29,* 5-17.

(10)   Jacinto, A.; Martinez-Arias, A.; Martin, P. Mechanisms of epithelial fusion and repair. *Nat. Cell Biol.* **2001**, *3,* E117-E123.

(11)   Sottile, J. Regulation of angiogenesis by extracellular matrix. *Biochim. Biophys. Acta* **2004**, *1654,* 13-22.

(12)   Hood, J. D.; Cheresh, D. A. Role of integrins in cell invasion and migration. *Nat. Rev. Cancer* **2002**, *2,* 91-100.

(13)   Bogenrieder, T.; Herlyn, M. Axis of evil: molecular mechanisms of cancer metastasis. *Oncogene* **2003**, *22,* 6524-6536.

(14)   Lauffenburger, D. A.; Horwitz, A. F. Cell migration: a physically integrated molecular process. *Cell* **1996**, *84,* 359-369.

(15)   Palecek, S. P.; Schmidt, C. E.; Lauffenburger, D. A.; Horwitz, A. F. Integrin dynamics on the tail region of migrating fibroblasts. *J. Cell Sci.* **1996**, *109,* 941-952.

(16)   Ridley, A. J.; Schwartz, M. A.; Burridge, K.; Firtel, R. A.; Ginsberg, M. H.; Borisy, G.; Parsons, J. T.; Horwitz, A. R. Cell migration: integrating signals from front to back. *Science* **2003**, *302,* 1704-1709.

(17)   van Haastert, P. J. M.; Devreotes, P. N. Chemotaxis: signaling the way forward. *Nat. Rev. Mol. Cell Biol.* **2004**, *5,* 626-634.

(18)   Insall, R. H.; Jones, G. E. Moving matters: signals and mechanisms in directed cell migration (Report of the EMBO Workshop on Cell Migration). *Nat. Cell Biol.* **2006**, *8,* 776-779.

(19)   Stephens, L.; Milne, L.; Hawkins, P. Moving towards a better understanding of chemotaxis. *Curr. Biol.* **2008**, *18,* R485-R494.

(20)   Tamkun, J. W.; DeSimone, D. W.; Fonda, D.; Patel, R. S.; Buck, C.; Horwitz, A. F.; Hynes, R. O. Structure of integrin, a glycoprotein involved in the transmembrane linkage between fibronectin and actin. *Cell* **1986**, *46,* 271-282.

(21)   Hynes, R. O. Integrins: a family of cell surface receptors. *Cell* **1987**, *48,* 549-554.

(22)   van der Flier, A.; Sonnenberg, A. Function and interactions of integrins. *Cell Tissue Res.* **2001**, *305,* 285-298.

(23)   Berrier, A. L.; Yamada, K. M. Cell-matrix adhesion. *J. Cell. Physiol.* **2007**, *213,* 565-573.

(24)   Luo, B.; Carman, C. V.; Springer, T. A. Structural basis of integrin regulation and signaling. *Annu. Rev. Immunol.* **2007**, *25,* 619-647.

(25)   Pierschbacher, M. D.; Ruoslahti, E. Cell attachment activity of fibronectin can be duplicated by small synthetic fragments of the molecule. *Nature* **1984**, *309,* 30-33.

(26)   Pierschbacher, M. D.; Ruoslahti, E. Variants of the cell recognition site of fibronectin that retain attachment-promoting activity. *Proc. Natl. Acad. Sci. U.S.A.* **1984**, *81,* 5985-5988.

(27)   Ruoslahti, E. RGD and other recognition sequences for integrins. *Ann. Rev. Cell Dev. Biol.* **1996**, *12,* 697-715.

(28)   Hynes, R. O. The emergence of integrins: a personal and historical perspective. *Matrix Biology* **2004**, *23,* 333-340.

(29)   Zamir, E.; Geiger, B. Components of cell-matrix adhesions. *J. Cell. Sci.* **2001**, *114,* 3577-3579.

(30)   Arnaout, M. A.; Goodman, S. L.; Xiong, J. Structure and mechanics of integrin-based cell adhesion. *Curr. Opin. Cell Biol.* **2007**, *19,* 495-507.

(31)   Jockusch, B. M.; Bubeck, P.; Giehl, K.; Kroemker, M.; Moschner, J.; Rothkegel, M.; Rudiger, M.; Schluter, K.; Stanke, G.; Winkler, J. The molecular architecture of focal adhesions. *Annu. Rev. Cell Dev. Biol.* **1995**, *11,* 379-416.

(32)   Brakebusch, C.; Fassler, R. The integrin-actin connection, an eternal love affair. *EMBO J.* **2003**, *22,* 2324-2333.

(33)   Turner, C. E.; Glenney, J. R.,Jr.; Burridge, K. Paxillin: a new vinculin-binding protein present in focal adhesions. *J. Cell Biol.* **1990**, *111,* 1059-1068.

(34)   Zamir, E.; Menachem, K.; Posen, Y.; Erez, N.; Yamada, K. M.; Katz, B. -.; Lin, S.; Lin, D. C.; Bershadsky, A.; Kam, Z.; Geiger, B. Dynamics and segregation of cell-matrix adhesions in cultured fibroblasts. *Nat. Cell Biol.* **2000**, *2,* 191-196.

(35)   Wehrle-Haller, B.; Imhof, B. A. The inner lives of focal adhesions. *Trends Cell Biol.* **2002**, *12,* 382-389.

(36)   Wiesner, S.; Legate, K. R.; Fassler, R. Integrin-actin interactions. *CMLS-Cell. Mol. Life Sci.* **2005**, *62,* 1081-1099.

(37)   Linder, S.; Aepfelbacher, M. Podosomes: adhesion hot-spots of invasive cells. *Trends in Cell Biol.* **2003**, *13,* 376-385.

(38)   Maheshwari, G.; Brown, G.; Lauffenburger, D. A.; Wells, A. and Griffith, L.G. Cell adhesion and motility depend on nanoscale RGD clustering. *J. Cell Sci.* **2000**, *113,* 1677-1686.

(39)   Koo, L. Y.; Irvine, D. J.; Mayes, A. M.; Lauffenburger, D. A.; Griffith, L. G. Co-regulation of cell adhesion by nanoscale RGD organization and mechanical stimulus. *J. Cell. Sci.* **2002**, *115,* 1423-1433.

(40)   Hersel, U.; Dahmen, C.; Kessler, H. RGD modified polymers: biomaterials for stimulated cell adhesion and beyond. *Biomaterials* **2003**, *24,* 4385-4415.

(41)   Walpita, D.; Hay, E. Studying actin-dependent processes in tissue culture. *Nat. Rev. Mol. Cell Biol.* **2002,** *3,* 137-141.

(42)   Schneider, G.; Burridge, K. Formation of focal adhesions by osteoblasts adhering to different substrata. *Exp. Cell Res.* **1994,** *214*(1), 264-269.

(43)   Mrksich, M.; Dike, L. E.; Tien, J.; Ingber, D. E.; Whitesides, G. M. Using microcontact printing to pattern the attachment of mammalian cells to self-assembled monolayers of alkanethiolates on transparent films of gold and silver. *Exp. Cell Res.* **1997**, *235,* 305-313.

(44)   Kane, R. S.; Takayama, S.; Ostuni, E.; Ingber, D. E.; Whitesides, G. M. Patterning proteins and cells using soft lithography. *Biomaterials* **1999**, *20,* 2363-2376.

(45)   Lehnert, D.; Wehrle-Haller, B.; David, C.; Weiland, U.; Ballestrem, C.; Imhof, B. A.; Bastmeyer, M. Cell behaviour on micropatterned substrata: limits of extracellular matrix geometry for spreading and adhesion. *J. Cell. Sci.* **2004**, *117,* 41-52.

(46)   Slater, J. H.; Frey, W. Nanopatterning of fibronectin and the influence of Integrin clustering on endothelial cell spreading and proliferation. *J. Biomed. Mater. Res. Part A* **2008**, *87A,* 176-195.

(47)   Irvine, D. J.; Mayes, A. M.; Griffith, L. G. Nanoscale clustering of RGD peptides at surfaces using comb polymers. 1. Synthesis and characterization of comb thin films. *Biomacromolecules* **2001**, *2,* 85-94.

(48)   Irvine, D. J.; Ruzette, A. G.; Mayes, A. M.; Griffith, L. G. Nanoscale clustering of RGD peptides at surfaces using comb polymers. 2. Surface segregation of comb polymers in polylactide. *Biomacromolecules* **2001**, *2,* 545-556.

(49)   Arnold, M.; Cavalcanti-Adam, E. A.; Glass, R.; Blu mmel, J.; Eck, W.; Kantlehner, M.; Kessler, H.; Spatz, J. P. Activation of integrin function by nanopatterned adhesive surfaces. *ChemPhysChem* **2004**, *5,* 383-388.

(50)   Cavalcanti-Adam, E. A.; Micoulet, A.; Blümmel, J.; Auernheimer, J.; Kessler, H.; Spatz, J. P. Lateral spacing of integrin ligands influences cell spreading and focal adhesion assembly. *Eur. J. Cell Biol.* **2006**, *85,* 219-224.

(51)   Cavalcanti-Adam, E. A.; Volberg, T.; Micoulet, A.; Kessler, H.; Geiger, B.; Spatz, J. P. Cell spreading and focal adhesion dynamics are regulated by spacing of integrin ligands. *Biophys. J.* **2007**, *92,* 2964-2974.

(52)   Piner, R. D.; Zhu, J.; Xu, F.; Hong, S. H.; Mirkin, C. A. "Dip-pen" nanolithography. *Science* **1999**, *283,* 661-663.

(53)   Wilson, D. L.; Martin, R.; Hong, S.; Cronin-Golomb, M.; Mirkin, C. A.; Kaplan, D. L. Surface organization and nanopatterning of collagen by dip-pen nanolithography. *Proc. Natl. Acad. Sci. U.S.A.* **2001**, *98,* 13660-13664.

(54)   Lee, K.; Lim, J.; Mirkin, C. A. Protein nanostructures formed via direct-write dip-pen nanolithography. *J. Am. Chem. Soc.* **2003**, *125,* 5588-5589.

(55)   Lee, K.; Kim, E.; Mirkin, C. A.; Wolinsky, S. M. The use of nanoarrays for highly sensitive and selective detection of Human Immunodeficiency Virus Type 1 in plasma. *Nano Lett.* **2004***, 4,* 1869-1872.

(56)   Lee, K.; Park, S.; Mirkin, C. A.; Smith, J. C.; Mrksich, M. Protein nanoarrays generated by dip-pen nanolithography. *Science* **2002**, *295,* 1702-1705.

(57)   Hoover, D. K.; Lee, E.-J.; Chan, E. W. L.; Yousaf, M. N. Electroactive nanoarrays for biospecific ligand mediated studies of cell adhesion. *ChemBioChem* **2007**, *8,* 1920-1923.

(58)   Hoover, D. K.; Chan, E. W. L.; Yousaf, M. N. Asymmetric peptide nanoarray surfaces for studies of single cell polarization. *J. Am. Chem. Soc.* **2008**, *130,* 3280-3281.

(59)   Hoover, D. K.; Lee, E.-J.; Yousaf, M. N. Total internal reflection fluorescence microscopy of cell adhesion on patterned self-assembled monolayers on gold. *Langmuir* **2009**, *25*(5), 2563-2566.

CHAPTER 2

SYMMETRIC ELECTROACTIVE NANOARRAYS FOR SINGLE CELL ADHESION STUDIES

2.1 Introduction

In order to study the nanoarchitecture of adherent cells in response to biospecific interactions, four main criteria must be defined. The first criterion addresses that the interactions between the cell surface receptors and the immobilized ligands must be well defined and free of nonspecific influences. Second, the substrate must be compatible with standard cell culture conditions and the use of high-resolution fluorescence microscopy for visualization. Finally, the feature sizes of the presented ligands must be in the nanometer scale, and the spatial distribution of immobilized ligands must be precisely defined. The following subsections will describe self-assembled monolayers (SAMs) of alkanethiols on gold as a proposed model system to fulfill the first two requirements, as well as the use of dip-pen nanolithography (DPN) as a nanopatterning tool to satisfy the latter two criteria.

2.1.1 Self-assembled monolayers as a model system for cell biology. While the concept of self-assembly of organic molecules on surfaces was first recognized in the 1940s,[1] the first report of SAMs on gold was not published until Nuzzo and Allara described the adsorption of ω-substituted dialkyl disulfides on gold in 1983.[2] There has been a significant amount of research devoted to elucidating the structure of

SAMs on gold and other materials, describing the kinetics of the self-assembly process, and further developing these surfaces as platforms for a range of applications.[1,3] In particular, SAMs have been under consideration as potential model systems in biology for several years. SAMs of siloxanes on hydroxylated surfaces and alkanethiols on gold (111), as well as on other noble and coinage metals have been widely investigated.[3]

2.1.1.1 Silane-based SAMs on hydroxylated surfaces. SAMs of silanes are produced by the formation of polysiloxane connections between the silanes in solution (typically alkyl chlorosilanes, alkyl alkoxysilanes, or alkyl aminosilanes) and the surface silanol groups. The hydroxylated surfaces that have been investigated include silicon dioxide (SiO_2), mica, glass, and quartz. While these surfaces are compatible with cell culture and microscopy, there are several limitations that hinder the use of such model surfaces in cell biology. First, the silane chemistry that is employed in creating these SAMs is not trivial and is extremely sensitive to fluctuations in moisture, pH, and temperature.[1] It is also difficult to tailor the surface chemistry to a specific application because many functional groups are not compatible with silane chemistry. Also, the substrates used are amorphous, and the SAMs are not as mobile on the surface (due to the formation of numerous –O-Si-O-bonds), which leads to less-ordered SAMs.[1] Typically the substrates used with siloxane SAMs are transparent, easily enabling the use of microscopy to visualize adhered cells. However, the non-conductive nature of the surface hinders the use of several other techniques, including surface plasmon resonance spectroscopy (SPR) and electrochemistry. While silane-based SAMs are more thermally stable than

18

SAMs of alkanethiols on gold,[4] the experimental difficulties and the reproducibility problems of a silane-based system are a significant hindrance to its widespread applicability.

2.1.1.2 SAMs of alkanethiols on noble and coinage metals other than gold. Sulfur is known to have a high affinity for transition metals.[5] The properties of SAMs of alkanethiols on gold (111) surfaces have been historically the most studied system. Other popular systems that have been studied included SAMs of alkanethiols on silver (111), with SAMs on copper (111) and palladium garnering less attention. There are two major disadvantages to using SAMs on silver (111) as a platform for cell biology studies. First, silver oxidizes readily in air under ambient conditions, forming a native oxide layer that can lead to surface defects and, eventually, SAM degradation. Also, cytotoxic silver cations (Ag^+) can leach into the media. On the other hand, copper (111) surfaces oxidize even more rapidly in air to form copper oxides at the surface. In contrast, palladium surfaces offer a unique opportunity: palladium does not oxidize readily at room temperature, and is approximately equivalent in price as gold. However, the physical properties of SAMs on palladium are currently not as well known as those on gold (111).[3,6]

2.1.2 Physical characteristics of SAMs of alkanethiols on gold. It has been shown that long-chain ω-substituted alkanethiols of the form $HS(CH_2)_nX$ (where $0 \leq n \leq 21$ and X = CH_3, $CH=CH_2$, COOH, OH, etc.) will spontaneously form well-ordered monolayers on gold (111) surfaces.[5] The thiol functionality binds to the gold surface through chemisorption. The long alkyl chains stabilize the SAM through intermolecular interactions such as van der Waals forces. The head group at the ω

19

position can also help stabilize the structure through other intermolecular interactions (*e.g.* dipolar forces or hydrogen-bonding), depending on the nature of the functionality introduced. Due to the difference in the distance between chemisorbed sulfur atoms (~5 Å) and the optimum distance between the alkane chains to maximize interchain interactions (~4.25 Å), the SAM takes on a well-ordered structure with a 30° tilt normal to the surfa ce, as shown in Figure 2.1.[1,5,6] Another advantage of this system is the ease of producing alkanethiols with a range of head groups, due to the compatibility of many standard organic synthetic methods with thiol chemistry.[6]

2.1.2.1 Protein resistant SAMs of alkanethiols on gold. In order to study a biospecific interaction between only the immobilized ligand of interest and cell-surface receptors, it is critical that the remainder of the model surface be inert to the nonspecific adsorption of proteins and cells. Surfaces that are comprised of polyethylene oxide (PEO) or polyethylene glycol (PEG) are among the most commonly studied protein-resistant surfaces for the development of biomedical devices.[7] This study has been extended into the use of SAMs of oligo-(ethylene glycol)-terminated alkanethiols (EG_n-C_{11}-SH, where n is 2 − 7) on gold as an inert background for cell biological platforms. Characterization studies have shown that EG_n-C_{11}-SH self-assembles on gold much like *n*-alkanethiols, retaining a 30° tilt, thus forming a well-ordered structure.[6] SAMs of EG_n-C_{11}-SH (n = 2 − 7) on gold have been shown to resist nonspecific adhesion of proteins of various sizes.[8] Under cell culturing conditions, SAMs of EG_n-C_{11}-SH (n = 3 and 6) on gold have been shown to
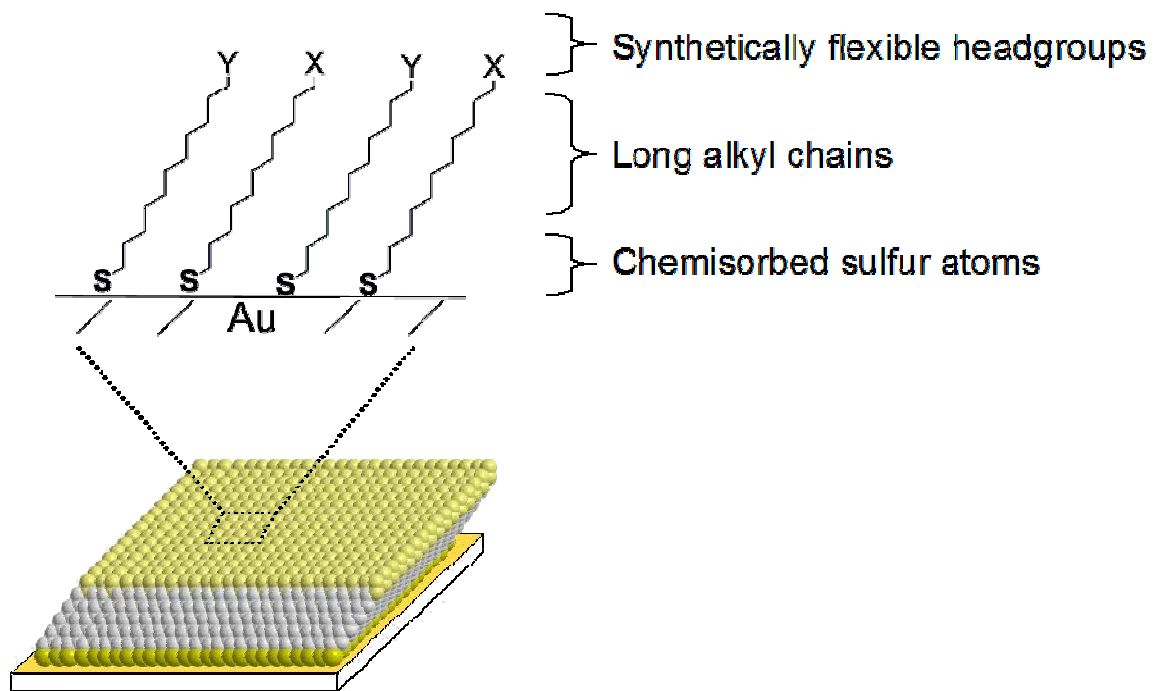
Figure 2.1 Self-assembled monolayers of alkanethiols on gold. Adapted from (1).

remain inert to cell adhesion and migration for up to 2 weeks.[9] While there have been many studies addressing several factors involved in the resistance of such surfaces to nonspecific protein adsorption, the exact mechanism of this process is still under investigation.[10,11]

2.1.2.2 Chemoselective immobilization of ligands. The ease of introducing chemical functionality into a SAM of alkanethiols on gold can be combined with the electroactive nature of the gold surface to produce an immobilization methodology. The Yousaf research group has developed a strategy using hydroquinone-terminated alkanethiols to form SAMs on gold substrates that takes advantage of the well-known hydroquinone/quinone redox couple (Figure 2.2A).[12-14] When the hydroquinone is oxidized electrochemically, the corresponding quinone can chemoselectively react with oxyamine functionalized ligands (R-ONH$_2$). This reaction proceeds at room temperature, under physiological conditions to produce a stable, covalent oxime product. The resulting oxime is also redox active, yielding a diagnostic oxidation peak that provides a method of monitoring the extent of reaction at the surface via cyclic voltammetry (Figure 2.2B).[15,16]

2.1.3 Dip-pen nanolithography as a nanopatterning tool. Dip pen nanolithography (DPN) can be used to pattern SAMs with precise spatial control in the nanometer regime. DPN is a technique based on atomic force microscopy (AFM) that is capable of forming features that are tens of nanometers wide.[17,18] In DPN, an AFM tip is used as a pen to directly write a molecule of interest (often referred to as the "ink") onto the surface. The "ink" solution is physically coated onto the AFM tip and is transported to the surface through diffusion processes. There are many factors that
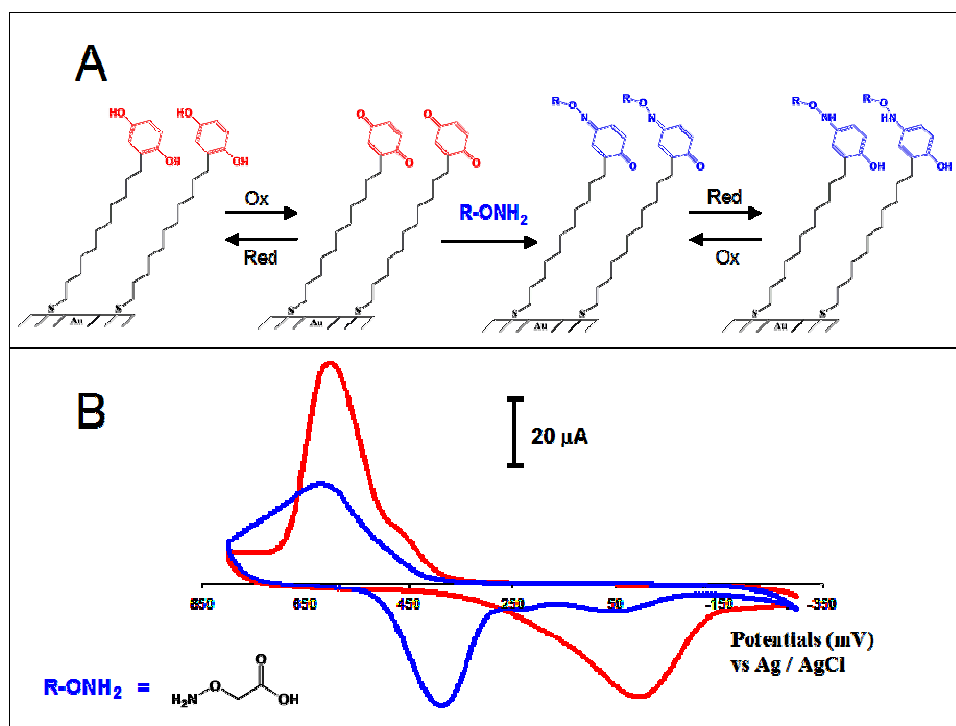
Figure 2.2 (A) SAMs of H_2Q-C_{11}-SH are oxidized to the quinone, which can then undergo a chemoselective reaction with an oxyamine-tethered ligand (R-ONH_2) to form a redox active oxime linkage. **(B)** Cyclic voltammograms (50 mV/s, 1 M $HClO_4$) show the shift in redox potentials from the hydroquinone / quinone couple (red trace) to the oxime product couple (blue trace).

affect the patterning of "ink" molecules in DPN, including humidity, temperature, tip-substrate contact force, tip-substrate contact time (dwell time), writing speed, tip geometry, and other chemical and physical properties of the "ink" and substrate.[19,20]

2.1.4 Nanoscale model system for single cell studies. This project combines SAM surfaces, chemoselective immobilization, and DPN technology to produce nanopatterned substrates that meet all of the requirements necessary to study the nanoarchitecture of adherent cells. This model system also allows for quantifying the amount of ligand immobilized through cyclic voltammetry. SAMs of alkanethiols on gold are compatible with typical cell culture conditions and high-resolution fluorescence microscopy,[21] thus enabling the observation of the internal structures of adherent cells.

2.2 Experimental Materials and Methods

2.2.1 Synthesis of 11-(2,5-dihydroxylphenyl)-1-mercaptoundecane (Scheme 2.1). All reagents were purchased from Sigma (St. Louis, MO) and used as received. ^{1}H NMR spectra were obtained on a Bruker 400 MHz Avance spectrometer. Flash column chromatography was performed using silica as a stationary phase.

2.2.1.1 Synthesis of 11-(2,5-dimethoxyphenyl)-1-undecene. A solution of 1,4-dimethoxybenzene (3.026 g, 21.9 mmol) in anhydrous THF (20 mL) was cooled to -78 ℃ in a dry ice / acetone bath under an inert atmosphere of N_2. A solution of *tert*-butyllithium (3.1 mL, 1.7 M in pentane, 5.27 mmol) was added *via* syringe. The reaction was stirred for 1 h, and then warmed to RT. 11-Bromo-1-undecene (3.0 mL, 0.0137 mol) was added *via* syringe, and again stirred for 18 h, then concentrated *in*
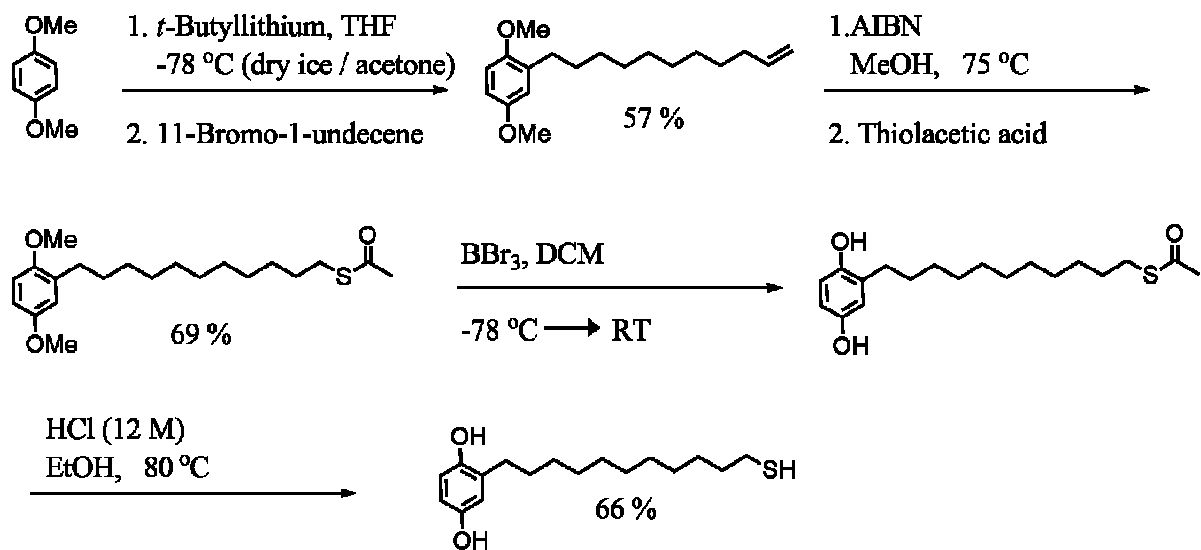
Scheme 2.1 Synthesis of 11-(2,5-dihydroxylphenyl)-1-mercaptoundecane (H$_2$Q-C$_{11}$-SH).

vacuo, yielding a yellow-orange liquid. The product was purified by flash column chromatography (20:1 hexanes : EtOAc mobile phase), yielding a clear, colorless oil (0.870 g, 3.00 mmol, 57%). ^{1}H NMR spectrum (CDCl$_3$, 400 MHz): δ 1.25 (m, 12H, **CH$_2$**), 1.60 (m, 2H, Ar-CH$_2$-**CH$_2$**-, J = 7.4 Hz), 2.00 (m, 2H, -**CH$_2$**-CH=CH$_2$, J = 6.7 Hz), 2.55 (t, 2H, Ar-**CH$_2$**-, J = 8.1 Hz), 3.80 (ds, 6H, -O**CH$_3$**), 4.90 (m, 2H, -CH=**CH$_2$**), 5.80 (m, 1H, -**CH**=CH$_2$), 6.75 (m, 3H, Ar-**H**).

2.2.1.2 Synthesis of 11-(2,5-dimethoxyphenyl)-1-(thioacetyl)undecane. A solution of 11-(2,5-dimethoxyphenyl)-1-undecene (0.870 g, 3.00 mmol) was dissolved in anhydrous THF (25 mL) and heated to reflux (75 – 80 °C). A catalytic amount of AIBN was added, and the reaction continued to stir under N$_2$. Thiolacetic acid (3 eq., 0.75 mL, 0.0105 mol) was added dropwise to the reaction mixture. The reaction was stirred under reflux for 18 h, and then concentrated *in vacuo* to a yellow liquid. The product was purified by flash column chromatography (6:1 hexanes : EtOAc mobile phase), yielding a light brown oil (0.756 g, 2.06 mmol, 69%). ^{1}H NMR spectrum (CDCl$_3$, 400 MHz): δ 1.25 (m, 14H, -**CH$_2$**-), 1.55 (m, 4H, Ar-CH$_2$-**CH$_2$**- and -CH$_2$-**CH$_2$**-S, J = 7.2 Hz), 2.30 (s, 3H, -**CH$_3$**), 2.55 (t, 2H, Ar-**CH$_2$**-, J = 7.6 Hz), 2.83 (t, 2H, -**CH$_2$**-S-, J = 7.2 Hz), 3.75 (ds, 6H, -O**CH$_3$**), 6.70 (m, 3H, Ar-**H**).

2.2.1.3 Synthesis of 11-(2,5-dihydroxylphenyl)-1-(thioacetyl)undecane. 11-(2,5-Dimethoxyphenyl)-1-(thioacetyl)undecane (0.756 g, 2.06 mmol) was dissolved in anhydrous DCM (25 mL) and cooled to -78 °C in a dry ice / acetone bath under an inert atmosphere of N$_2$. BBr$_3$ (1.2 mL, 12.7 mmol) was added *via* syringe after which the reaction was warmed to RT and allowed to stir for 2 h. The reaction was cooled again to -78 °C in a dry ice / acetone bath and excess B Br$_3$ was quenched by adding

a mixture of H_2O and diethyl ether *via* syringe. The reaction mixture was washed with H_2O (2 x 20 mL) and brine (1 x 20 mL). The organic layer was dried over Na_2SO_4 and concentrated *in vacuo* to yield a light brown oil (1.259 g crude), which afforded a yellowish-white solid after 18 h of refrigeration (4 °C). The lack of the singlets at δ 3.75 (-OC**H₃**) in the crude ^1H NMR spectrum ($CDCl_3$, 400 MHz) indicated that the deprotection reaction was successful.

2.2.1.4 Synthesis of 11-(2,5-dihydroxylphenyl)-1-mercaptoundecane (H_2Q-C_{11}-SH). 11-(2,5-Dihydroxylphenyl)-1-(thioacetyl)undecane (crude yield, 1.259 g) was dissolved in ethanol (50 mL) and heated to reflux (80 °C). Hydrochloric acid (5 mL, 12 M, 60.5 mmol) was added dropwise and the reaction was allowed to stir at reflux for 18 h. The reaction mixture was then concentrated *in vacuo* to a yellow oil which was dissolved in EtOAc (50 mL), washed with H_2O (1 x 20 mL, 1 x 40 mL), dried over Na_2SO_4 and concentrated *in vacuo*. The product was purified by flash column chromatography (3:1 hexanes : EtOAc mobile phase) to yield a white solid (0.400 g, 1.35 mmol, 66% yield from expected yield of 11-(2,5-dimethoxyphenyl)-1-(thioacetyl)undecane starting material). ^1H NMR spectrum ($CDCl_3$, 400 MHz): δ 1.30 (m, 14H, -C**H₂**-), 1.55 (m, 5H, -S**H,** Ar-CH_2-C**H₂**- and -C**H₂**-CH_2-S, J = 7.6 Hz), 2.51 (m, 4H, Ar-C**H₂**- and -CH_2-C**H₂**-S, J = 7.6 Hz), 4.32 (ds, 2H, Ar-O**H**), 6.56 (m, 3H, Ar-**H**).

2.2.2 Synthesis of 23-mercapto-3,6,9,12-tetraoxatricosan-1-ol (Scheme 2.2). All reagents were purchased from Sigma (St. Louis, MO) and used as received, unless otherwise noted. ^1H NMR spectra were obtained on a Bruker 400 MHz Avance
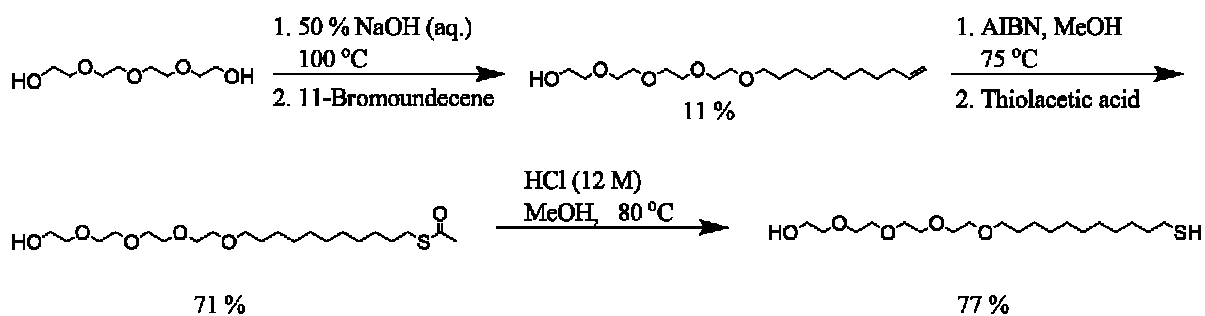
Scheme 2.2 Synthesis of 23-mercapto-3,6,9,12-tetraoxatricosan-1-ol (EG$_4$-C$_{11}$-SH).

spectrometer. Flash column chromatography was performed using silica as a stationary phase.

2.2.2.1 Synthesis of 3,6,9,12-tetraoxatricos-22-en-1-ol tetra(ethylene glycol). 2,2'-(2,2'-oxybis(ethane-2,1-diyl)bis(oxy))diethanol, 11.0 mL, 63.7 mmol) was heated to 100 ℃, after which 1.0 mL of 50% NaOH (aq) was added and stirred for 30 min. 11-Bromo-1-undecene (8.5 mL, 38.7 mmol) was added and the reaction mixture was stirred for 15 h at 100 ℃. After the reaction mixtur e was cooled to RT, hexanes (3 x 25 mL) was added, stirred vigorously for 30 min, and separated from the aqueous layer. The aqueous layer was extracted a final time with hexanes (1 x 15 mL). The organic layers were combined and concentrated *in vacuo* to a dark yellow liquid. The product was purified by flash column chromatography (1:1 hexanes : EtOAc mobile phase, followed by pure EtOAc, and pure methanol) to yield a pale yellow oil (1.50 g, 4.33 mmol, 11%). ^{1}H NMR spectrum (CDCl$_3$, 400 MHz): δ 1.30 (m, 12H, -C**H$_2$**-), 1.50 (m, 2H, -O-CH$_2$-C**H$_2$**-CH$_2$, J = 6.8 Hz), 2.00 (m, 2H, -C**H$_2$**-CH=CH$_2$, J = 5.6 Hz), 2.60 (t, 1H, -O**H**, J = 6.4 Hz), 3.40 (t, 2H, -O-C**H$_2$**-CH$_2$-CH$_2$-, J = 6.8 Hz), 3.60 (m, 16H, -O-C**H$_2$**-C**H$_2$**-O-), 4.90 (m, 2H, -CH=C**H$_2$**, J = 8.8 Hz), 5.70 (m, 1H, -C**H**=CH$_2$, J = 10 Hz).

2.2.2.2 Synthesis of S-1-hydroxy-3,6,9,12-tetraoxatricosan-23-yl ethanethioate. A solution of 3,6,9,12-tetraoxatricos-22-en-1-ol (1.50 g, 4.33 mmol) in methanol (25 mL) was heated to 75 ℃ under reflux with stirring. A catalytic amount of AIBN was added. Thiolacetic acid (0.6 mL, 8.39 mmol) was added *via* syringe. The solution was refluxed for 18 h. After the reaction cooled to RT, the solution was concentrated *in vacuo* to afford a light yellow solid precipitate. Prior to further purification, EtOAc

was added to the solution and the yellow solid (~30 mg) was removed by gravity filtration. The yellow solution was then purified by flash column chromatography (1:1 hexanes : EtOAc mobile phase, followed by 4:1 EtOAc : methanol, and pure methanol) and afforded a yellow oil (1.30 g, 3.08 mmol, 71%). ^{1}H NMR spectrum (CDCl$_3$, 400 MHz): δ 1.23 (m, 14H, -C**H$_2$**-), 1.50 (m, 4H, -O-CH$_2$-C**H$_2$**-CH$_2$- and -C**H$_2$**-CH$_2$-S, J = 6.8 Hz), 2.75 (s, 3H, -C**H$_3$**), 2.82 (t, 2H, -CH$_2$-C**H$_2$**-S, J = 7.2 Hz), 3.40 (t, 2H, -O-C**H$_2$**-CH$_2$-CH$_2$-, J = 6.8 Hz), 3.57 (m, 14H, -O-C**H$_2$**-C**H$_2$**-O-), 3.68 (m, 2H, HO-C**H$_2$**-, H = 4.4 Hz).

2.2.2.3 Synthesis of 23-mercapto-3,6,9,12-tetraoxatricosan-1-ol (EG$_4$-C$_{11}$-SH). Hydrochloric acid (10.0 mL, 12 M, 0.120 mol) was added to a solution of *S*-1-hydroxy-3,6,9,12-tetraoxatricosan-23-yl ethanethioate (1.30 g, 3.08 mmol) in methanol (30 mL). This solution was stirred and heated to reflux (80 °C) for 18 h, then cooled to RT and concentrated *in vacuo* to yield a light yellow-brown oil. This oil was redissolved in EtOAc (20 mL), washed with NaHCO$_3$ (3 x 15 mL), brine (1 x 15 mL), dried over Na$_2$SO$_4$ and concentrated *in vacuo* to yield light yellow oil (0.900 g, 2.36 mmol, 77%). ^{1}H NMR spectrum (CDCl$_3$, 400 MHz): δ 1.30 (m, 14H, -C**H$_2$**-), 1.50 (m, 4H, -O-CH$_2$-C**H$_2$**-CH$_2$- and -C**H$_2$**-CH$_2$-S), 2.49 (q, 2H, -C**H$_2$**-S, J = 7.2 Hz), 3.42 (t, 2H, -O-C**H$_2$**-CH$_2$-, J = 6.8 Hz), 3.60 (m, 14H, -O-C**H$_2$**-C**H$_2$**-O-), 3.70 (t, 2H, HO-C**H$_2$**-, J = 4.4 Hz).

2.2.3 Synthesis of linear RGD-oxyamine peptide (Scheme 2.3). Standard Fmoc-based solid-phase peptide synthesis was used to produce oxyamine-terminated linear RGD using an automated peptide synthesizer (C S Bio Co., Menlo Park, CA). Rink amide 4-methylbenzhydrylamine (MBHA) resin (0.58 mmol/g), amino acids
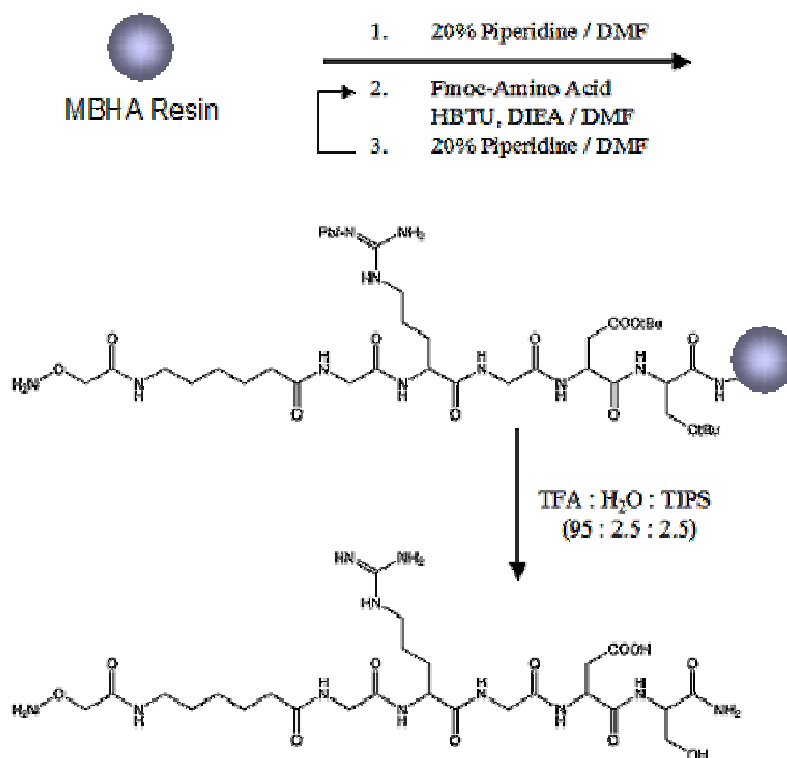
Scheme 2.3 Fmoc-based solid-phase peptide synthesis of the cell adhesive peptide, oxyamine-terminated linear RGD.

(Fmoc-Arg(Pbf)-OH, Fmoc-Asp(OtBu)-OH, Fmoc-Gly-OH, and Fmoc-Ser(tBu)-OH), Boc-aminooxy acetic acid, and HBTU were purchased from AnaSpec (San Jose, CA). DIEA and TIPS were purchased from Acros Organics. Fmoc-6-aminohexanoic acid was purchased from Sigma. Piperidine was purchased from Fluka, and solvents (DMF, DCM) were purchased from Fisher.

Rink amide MBHA resin (0.127 g, 0.1 mmol) was placed in an automated peptide synthesizer chamber. The amino acids Fmoc-Arg(Pbf)-OH, Fmoc-L-Asp(OtBu)-OH, Fmoc-L-Gly-OH, Fmoc-Ser(tBu)-OH), Boc-aminooxy acetic acid, and Fmoc-6-aminohexanoic acid were measured in threefold excess (0.30 mmol) and dissolved in 5 mL of DMF for each time the amino acid appears in the desired sequence. All other reagents were prepared in DMF: 0.1 M HBTU, 0.1 M DIEA, and 20% (by volume) piperidine. Following peptide elongation, the resin was placed in a N_2 bubbling chamber with a cleavage cocktail of TFA : H_2O : TIPS (95% : 2.5% : 2.5%, by volume) for 60 min. The resin was then removed by filtration and the peptide containing solution was concentrated *in vacuo*. The peptide was precipitated by ice-cold diethyl ether, centrifuged, and the peptide pellet redissolved in H_2O. The H_2O solution was frozen and lyophilized to yield a white solid. Direct infusion MS (QQQ, ESI+): expected exact mass 675.33 Da, observed exact mass 675.4 Da.

Cyclic RGD peptide was prepared by Eun-ju Lee (Yousaf group, University of North Carolina at Chapel Hill) and used without further purification.

2.2.4 Gold-coated substrate preparation. Glass cover slips, concentrated H_2SO_4, and 30% H_2O_2 were purchased from Fisher. Gold and titanium evaporation slugs

were purchased from Aldrich. Distilled water was obtained using a Millipore Direct-Q UV system (Millipore Corporation, Bedford, MA). All thin layer metal deposition was performed using a vacuum evaporator system with a 3 kW electron beam gun (Model VE-100, Thermionics Laboratory, Inc., Port Townsend, WA).

Glass cover slips (Fisher) were cleaned with Piranha solution (3:1 (v:v) concentrated H_2SO_4 : 30% H_2O_2). An adhesion layer of titanium (5-6 nm) and a transparent layer of gold (15-24 nm) were then thermally evaporated onto the surface. After preparation, the gold-coated substrates were again cleaned with Piranha solution (1:1 (v:v) concentrated H_2SO_4 : 30% H_2O_2) for ~1 min, thoroughly rinsed with H_2O, and either stored in H_2O or dried with compressed air and used directly.

2.2.5 Dip-pen nanolithography (DPN) methodology. Silicon AFM tips (nominal spring constants: 0.03 - 0.08 N/m) were purchased from MikroMasch USA, Wilsonville, OR. Acetonitrile (Optima grade) was purchased from Fisher. All DPN and lateral force microscopy (LFM) measurements were made using a MFP-3D Stand Alone atomic force microscope (Asylum Research, Santa Barbara, CA). DPN pattern design and image analysis was performed using IgorPro software (WaveMetrics, Inc., Portland, OR) and MicroAngelo™ LithoStep nanolithography software (Aslyum Research).

AFM tips were immersed in a solution of H_2Q-C_{11}-SH (5 mM in acetonitrile, 40 s) and then gently dried with compressed air. MicroAngelo™ LithoStep program was used to produce nanoarray patterns. Square nanoarrays of H_2Q-C_{11}-SH on bare gold (20 x 20, 3.0 μm pitch, dwell time 30.0 s, diameter ~500 nm, total patterned

area of 60 μm x 60 μm) were produced by DPN for cell adhesion studies. The nanoarrays were imaged directly following printing at a scan rate of 4 Hz. IgorPro software was used for image analysis and feature size measurements. The remaining bare regions of gold were passivated by immersing the substrate in a solution of EG_4-C_{11}-SH (1 mM in ethanol, ~12 h). The nano-patterned substrates were either stored in H_2O for less than 36 h prior to use, or were hydrated in H_2O for 1 – 1.5 h prior to immediate ligand immobilization.

2.2.6 Characterization of electroactive nanoarrays by cyclic voltammetry (CV). All CV experiments were performed using a three-electrode potentiostat (BAS 100B/W Electrochemical Analyzer, Bioanalytical Systems, Inc., West Lafayette, IN) with a Ag/AgCl reference electrode, platinum wire auxiliary electrode, and the gold-coated substrate as the working electrode. $HClO_4$ was purchased from Fisher and AOAA was purchased from Sigma.

Four nanoarrays (20 x 20) of dots of H_2Q-C_{11}-SH (3.0 $\square$m pitch, dwell time 30.0 s, diameter ~500 nm) were produced on a gold-coated glass substrate, as previously described. The remaining bare regions of gold were passivated by immersing the substrate in a solution of EG_4-C_{11}-SH (1 mM in ethanol, ~12 h), followed by immersion in H_2O for 1 h prior to use. CVs of the unmodified H_2Q-C_{11}-SH nanoarrays were obtained in 1.0 M $HClO_4$ (potential window: −150 to 750 mV vs. Ag/AgCl, scan rate: 50 mV/s). The hydroquinone groups were oxidized to the quinone by applying a potential of 750 mV (vs Ag/AgCl) for 15 s. Following the immobilization reaction of AOAA (150 mM in H_2O, 4 h), CVs were taken with the same parameters as previously described.

2.2.7 Immobilization of peptide ligands to electroactive nanoarrays. The H_2Q-C_{11}-SH nanoarrays were oxidized by applying a potential of 750 mV (vs. Ag/AgCl, 1.0 M $HClO_4$) for 15 s. Following electrochemical oxidation of the nano-patterned substrates, the resulting quinone was then reacted with oxyamine-terminated linear RGD peptide (10 mM in PBS) or cyclic RGD peptide (10 mM in PBS) for 5 h.

2.2.8 Cell seeding and staining techniques. 3T3 Swiss Albino mouse fibroblasts[22] were obtained from the Tissue Culture Facility, the University of North Carolina at Chapel Hill. DMEM, bovine calf serum, Dulbecco's PBS, Triton X – 100, DAPI and phalloidin-TRITC were purchased from Sigma, and paraformaldehyde solution (32%) was purchased from Fisher. Penicillin/streptomycin was purchased from Gibco. Mouse anti-paxillin antibody was purchased from B D Biosciences (San Jose, CA), normal goat serum and Cy-2 conjugated goat anti-mouse IgG was purchased from Jackson ImmunoResearch Laboratories, Inc. (West Grove, PA). Fluorescence mounting medium was purchased from Dako (Carpinteria, CA).

3T3 Swiss Albino mouse fibroblasts were seeded on the patterned substrates in serum-free DMEM for 3 h, followed by incubation for ~18 h in DMEM containing 10% bovine calf serum and 1% penicillin/streptomycin (37 ⁰C, 5% CO_2 atmosphere). The patterned cells were then fixed with 3.2% formaldehyde in Dulbecco's PBS and permeated with PBS containing 0.1% Triton X – 100. Both dye mixtures were made in 5% normal goat serum in PBS containing 0.1% Triton X –100. The substrates were placed in a humidified chamber and incubated with the first dye mixture (mouse anti-paxillin, 1:1000 dilution; phalloidin-TRITC, 1:50 dilution) for 2 h, then washed with PBS (3 x 10 min). The substrates were then incubated in the humidified

chamber with a second dye mixture (DAPI, 1:500 dilution; phalloidin-TRITC, 1:50 dilution; Cy-2 conjugated goat anti-mouse IgG, 1:100 dilution). The substrates were then prepared for microscopy by securing the nano-patterned substrate gold-coated side down in fluorescence mounting medium on a glass coverslip.

2.2.9 Fluorescence microscopy of patterned cells. Fluorescence images were taken using a Nikon Eclipse TE2000-E inverted microscope (Nikon USA, Inc., Melville, NY). Image analysis was performed using MetaMorph software (Molecular Devices, Downingtown, PA). Oil immersion images were obtained using a Plan Fluor 40X oil immersion objective with a 1.30 NA (Nikon USA). Immersion oil was purchased from Carl Zeiss MicroImaging, Inc. (Thornwood, NY) and lens paper was purchased from Fisher. All images were obtained within 36 h of the staining procedure and substrates were kept in a dark, dry environment when not in use.

2.3 Results and Discussion

2.3.1 DPN method development. Silicon AFM tips were inked by immersion in a solution of H_2Q-C_{11}-SH. MicroAngelo^{TM} LithoStep, a program for lithography and nano-manipulation from Asylum Research (Santa Barbara, CA), was used to produce arrays of spots. This program controls various parameters of DPN including the number of grid points in the x- and y-axis, the pitch (separation between the centers of adjacent spots), and the dwell time (tip – substrate contact time) at each point. The effect of dwell time on the deposition of H_2Q-C_{11}-SH on gold was studied under ambient conditions (Figure 2.3A). A 5 x 5 nanoarray with a pitch of 1 µm was printed with a dwell time that began at 3.0 s and increased by 3.0 s with each

A

B

Dwell Time (s)	Average Spot Diameter (nm)
3.0	198 ± 94
9.0	284 ± 121
12.0	312 ± 125
15.0	352 ± 158
30.0	447 ± 161
45.0	532 ± 231
60.0	552 ± 200
75.0	586 ± 171
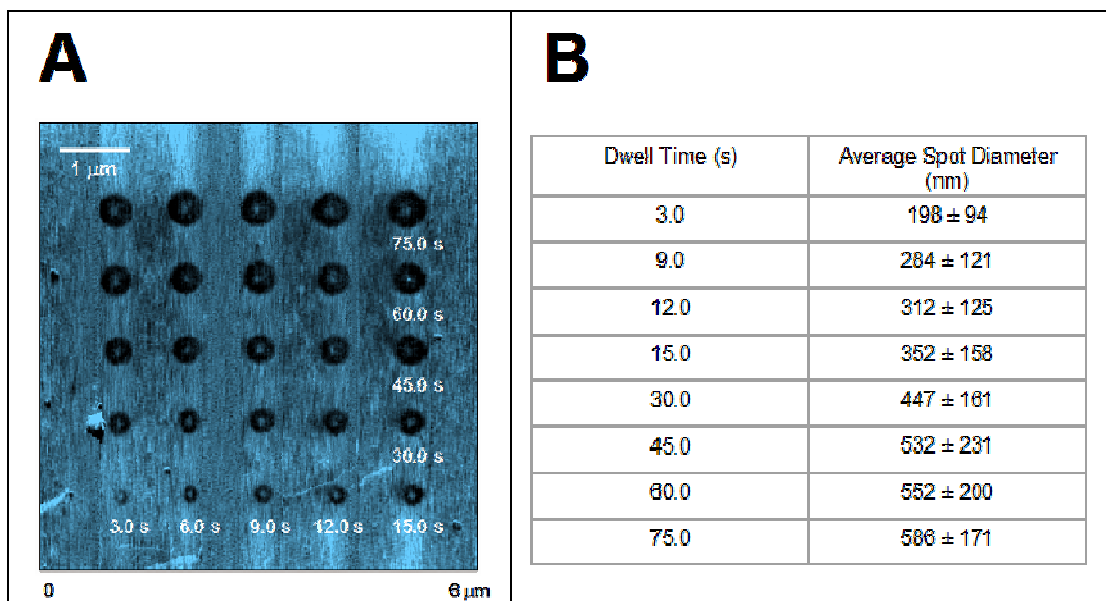
Figure 2.3 (A) LFM image demonstrating the effect of dwell time on average spot size in nanoarrays produced *via* DPN. The nanoarray of H_2Q-C_{11}-SH was printed with an increasing dwell time (beginning dwell time of 3.0 s, increasing by steps of 3.0 s). Average spot diameter for a dwell time of 30.0 s is approximately 500 nm. **(B)** The effect of dwell time (s) on average spot diameter in DPN. As dwell time is increased, the average spot diameter increases, and appears to plateau at around 30.0 s (n = 3 arrays).

subsequent spot. As can be seen in Figure 2.3B, the spot diameter increased with increasing dwell time. Prior to printing each 20 x 20 nanoarray for cell adhesion studies, a test nanoarray was produced and the dwell time adjusted accordingly to create ~500 nm diameter spots. A dwell time of 30.0 s was typically determined to be the optimal under ambient conditions required to produce spots with an average diameter of 500 nm.

2.3.2 Lateral force microscopy characterization of electroactive nanoarrays. A 20 x 20 nanoarray was produced following the procedure described above. The nanoarrays were imaged directly following printing using the same tip at a scan rate of 4 Hz and a scan angle of 90.0°, producing the late ral force image in Figure 2.4A. The nanoarray is composed of 400 spots, with a total patterned area of 60 μm X 60 μm. The lateral force profile taken across the expanded area of the nanoarray in Figure 2.4B demonstrates that each spot is similar in terms of diameter and lateral force. The average diameter of the dots in this array is ~500 nm.

2.3.3 Electrochemical characterization of electroactive nanoarrays. Four nanoarrays (20 x 20, ~500 nm diameter spots) of $H_2Q-C_{11}-SH$ were produced on a gold-coated glass substrate, as described above. A BAS 100B/W Electrochemical Analyzer was used to generate CVs of the hydroquinone / quinone redox couple, as shown in Figure 2.5 (red trace). The hydroquinone groups presented in the nanoarrays underwent a reversible oxidation at 660 mV and reduction at -20 mV. Previous reported CVs of full SAMs of H_2Q-CH_n-SH have shown a CV peak-to-peak potential separation of ~500 mV and ~600 mV for $H_2Q-CH_{10}-SH$ and $H_2Q-CH_{12}-SH$,
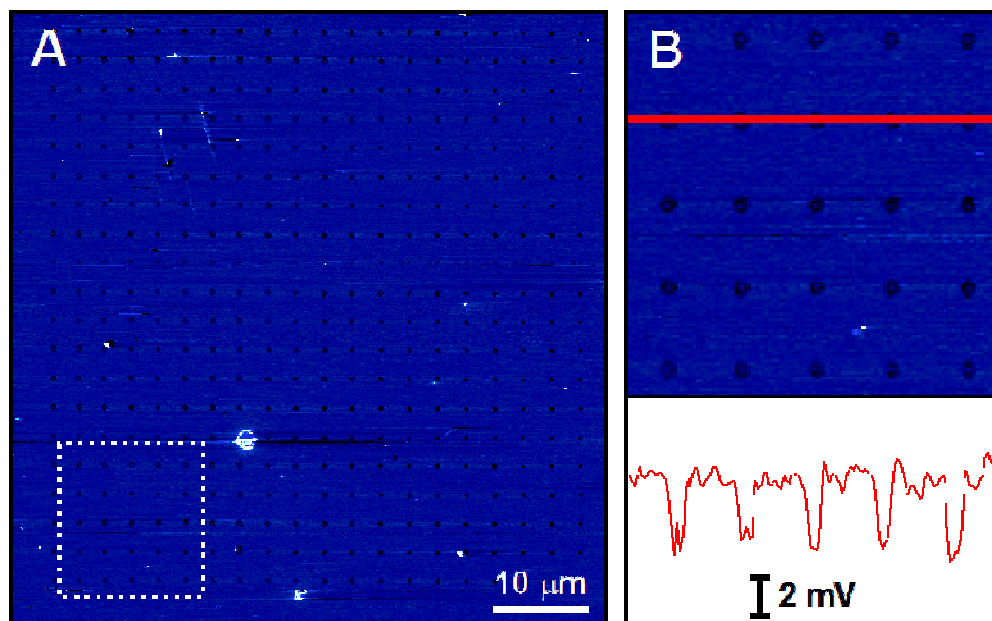
Figure 2.4 (A) LFM image of an electroactive nanoarray of H_2Q-C_{11}-SH on gold generated by DPN. The 20 x 20 nanoarray consists of 400 spots with an average spot diameter of 500 nm. **(B)** A lateral force profile for the line drawn across the expanded image (region in white box in **A**) is shown below the expanded image, indicating that each spot is consistent, both in diameter and lateral force.
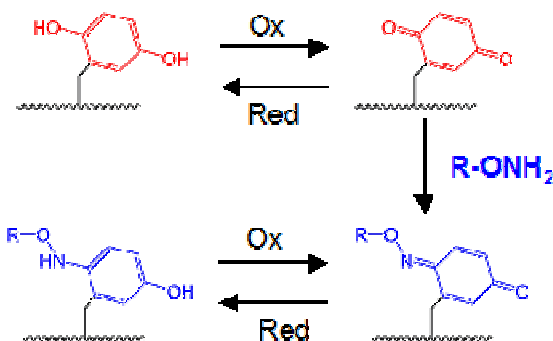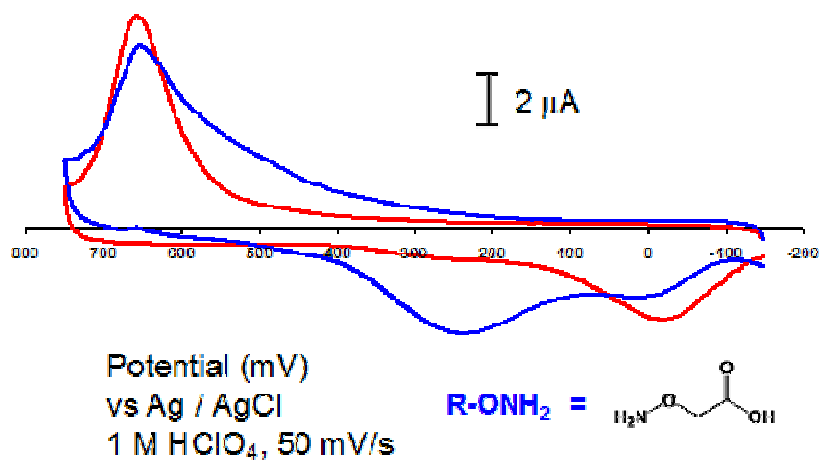
Figure 2.5 Electroactive nanoarrays of H_2Q-C_{11}-SH are first oxidized to the corresponding quinone, which can then chemoselectively react with (aminooxy) acetic acid (R-ONH_2). Cyclic voltammograms show the shift from the hydroquinone / quinone redox couple (red trace) to the oxime product redox couple (blue trace).

respectively.[23,24] The oxidation and reduction potentials found for nanoarrays of H_2Q-C_{11}-SH are also comparable to the previously reported oxidation and reduction potentials (580 mV and –30 mV, respectively) of 100% monolayers of H_2Q-C_{11}-SH.[12] The hydroquinone groups were then oxidized to the quinone by applying a potential of 750 mV (vs. Ag/AgCl, 1 M $HClO_4$) for 15 s. CVs taken following the immobilization of AOAA resulted in a shift in the oxidation and reduction peaks corresponding to oxime product to 520 mV and 235 mV, respectively. This result, taken in conjunction with the decrease in the oxidation and reduction peaks of the parent hydroquinone – quinone couple, indicate that the chemoselective immobilization reaction occurred.

2.3.4 Cell adhesion studies on symmetric electroactive nanoarrays.[25] Figure 2.6 represents a schematic of the experimental design used to study single cell adhesion on electroactive nanoarrays. Symmetric electroactive nanoarrays of H_2Q-C_{11}-SH were prepared as described above, yielding a total patterned area of 60 μm x 60 μm. Following electrochemical oxidation of the substrates, the resulting quinone was reacted with an oxyamine-terminated peptide. 3T3 Swiss Albino mouse fibroblasts were seeded on the patterned substrates, incubated in serum-containing DMEM (37 °C, 5% CO_2, ~18 h), fixed, and then permeated in PBS containing 0.1% Triton X-100. The cells were visualized using three fluorescent dyes targeting the nuclei, actin cytoskeleton, and focal adhesions. The focal adhesion structure was analyzed by staining with an anti-paxillin antibody. Paxillin is a protein found in focal adhesions.[26] Fluorescent micrographs were taken using a Nikon Eclipse TE2000-E inverted microscope.
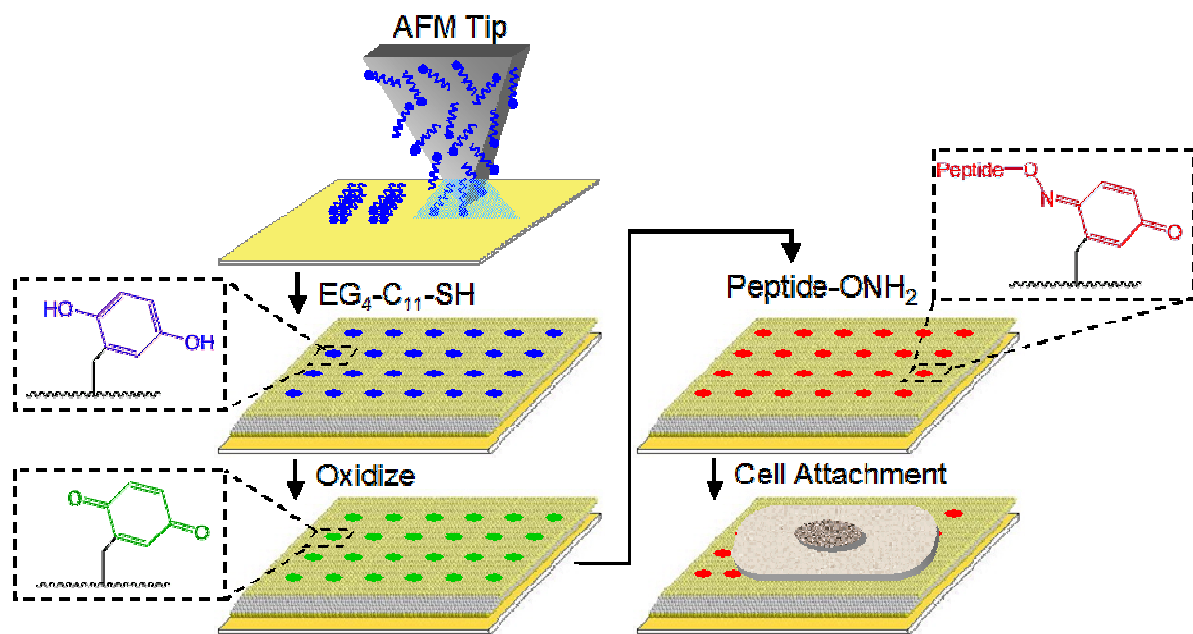
Figure 2.6 Schematic diagram for the preparation of electroactive nanoarrays by DPN. Nanoarrays of H_2Q-C_{11}-SH are patterned by DPN. After the remaining bare gold region is backfilled with EG_4-C_{11}-SH, the hydroquinone is oxidized to produce the quinone. An oxyamine-terminated peptide is chemoselectively immobilized via an oxime conjugate to promote cell adhesion on the electroactive nanoarray.

The first electroactive nanoarrays for cell adhesion studies were functionalized with immobilized oxyamine-terminated linear RGD (Figure 2.7A). The purpose of these experiments was twofold. First, this study was to ensure that the nanoarray presenting cell-adhesive ligand could support cell adhesion. The second objective was to observe the influence of the spatial presentation of linear RGD on the nanoarchitecture of the adherent cell through staining for paxillin.

Several representative micrographs of 3T3 Swiss Albino mouse fibroblasts adhered to nanoarrays of immobilized linear RGD peptide are shown in Figure 2.8. The cells were stained with three fluorescent dyes: DAPI (nuclei, blue), phalloidin-TRITC (actin cytoskeleton, red), and anti-paxillin with Cy-2 secondary fluorescent antibody (focal adhesions, green). The cells adopt a square to rectangular morphology which closes corresponds to the size of a single nanoarray (~60 μm x ~60 μm). Interestingly, the focal adhesion structures are localized primarily to the periphery of the adherent cell. This lack of well-formed focal adhesions throughout the cell likely results from the relatively low affinity for integrin receptors for linear RGD peptide, which has a K_d of ~10^{-6} (μM).[27] This low affinity leads to the cell staying in a more motile state, such that the cell is sampling the environment at a higher rate. In order to further investigate this phenomenon and to study the effect of ligand affinity on focal adhesion structures of adherent cells, a series of symmetric electroactive nanoarrays of the same dimensions as those produced for linear RGD studies were produced and an oxyamine-terminated cyclic RGD (Figure 2.7B) peptide was immobilized, as described below.
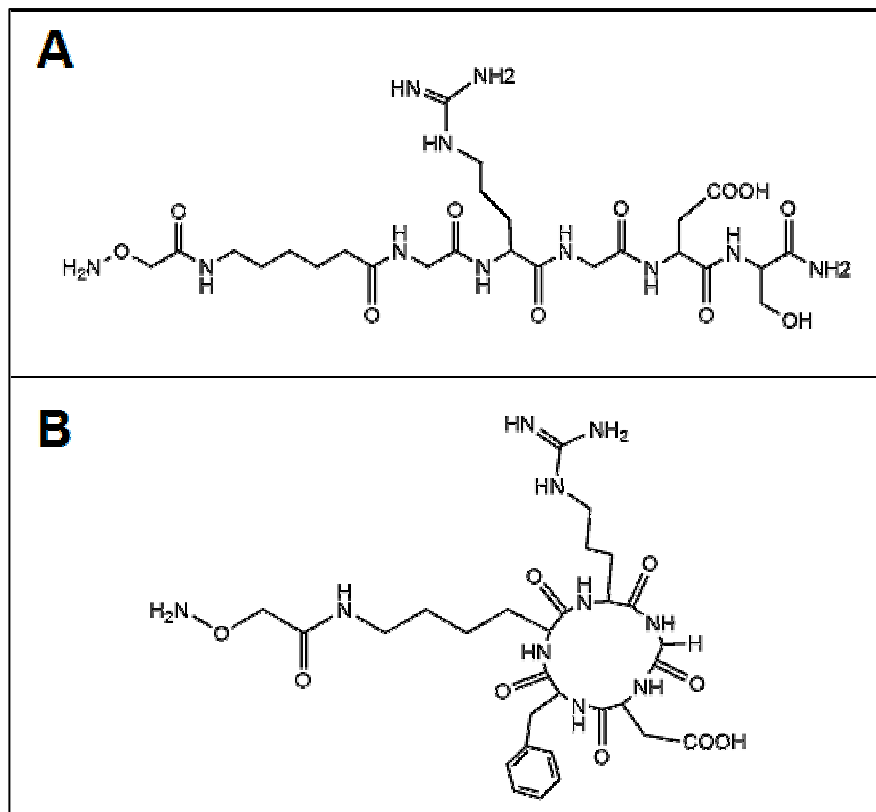
Figure 2.7 Structures of two cell-adhesive peptides that were immobilized to electroactive nanoarrays for cell adhesion studies. Integrin receptors are known to have a lower affinity to linear RGD peptide **(A)** than cyclic RGD peptide **(B)**.
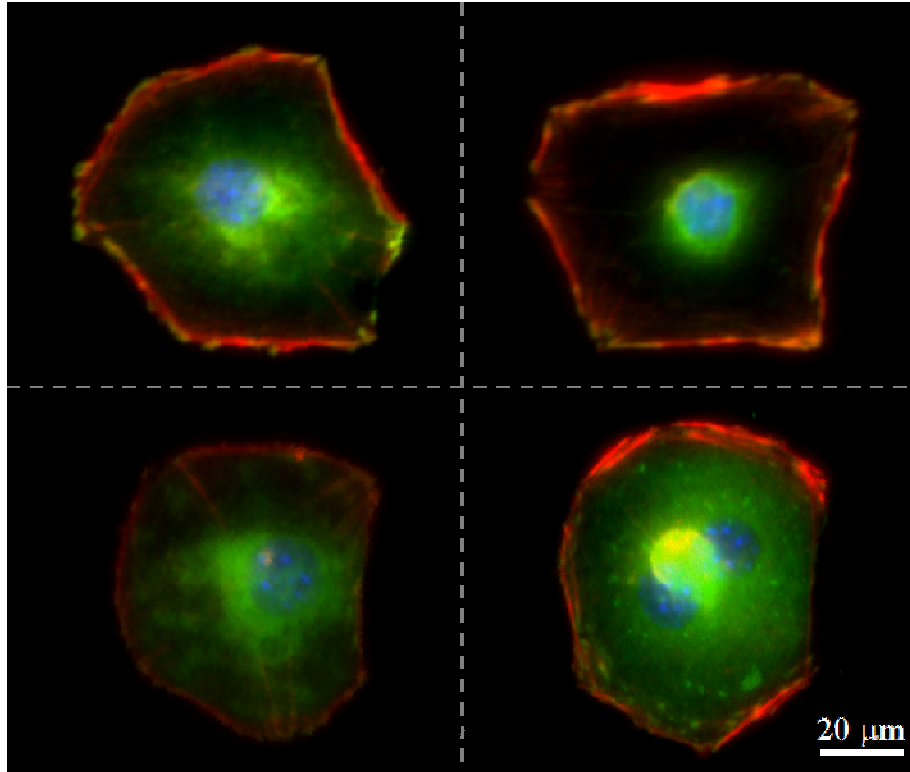
Figure 2.8 Representative fluorescent micrographs of 3T3 Swiss Albino fibroblasts on immobilized oxyamine-terminated linear RGD nanoarrays. Cells were stained for nuclei (blue), actin (red), and paxillin (green). The majority of the focal adhesions (green dots) are located at the periphery of the cells.

2.3.5 Effects of ligand affinity on cell adhesion to immobilized peptide nanoarrays. The affinity of integrin receptors for cyclic RGD is known to be much stronger than that of linear RGD (K_d of nM versus µM, respectively).[27] It has been suggested that this difference in binding is due to the conformation and flexibility inherent in the linear and cyclic forms of the RGD motif. A predominant hypothesis is that cyclic peptides more closely mimic the native environment of the RGD motif in ECM proteins, therefore inducing a higher affinity for integrin receptors.[28] It has been previously shown to dramatically affect focal adhesion patterning in adherent cells on model substrates presenting linear and cyclic RGD peptides homogeneously.[29]

Figure 2.9 shows representative fluorescent micrographs of 3T3 Swiss Albino fibroblasts adhered to single nanoarrays of immobilized cyclic RGD. The adherent cells were again stained with the same three fluorescent dyes: DAPI (nuclei, blue), phalloidin-TRITC (actin cytoskeleton, red), and anti-paxillin with Cy-2 secondary fluorescent antibody (focal adhesions, green). Again, the cells adopt a square morphology of approximately the same size as the single nanoarray (~60 µm x ~60 µm), indicating that the cell has been immobilized by a single nanoarray. In this instance, there are many more distinct focal adhesions that are distributed throughout the interior of the cells.

A two-step mechanism has been proposed to describe the assembly of focal adhesions. The first step, termed nucleation, is the gathering of integrin receptors into a condensed cluster structure. The second step, growth, is achieved by the recruitment of many single integrin receptors and clusters to form a mature focal adhesion.[29] It has been observed that the difference in ligand affinity between linear
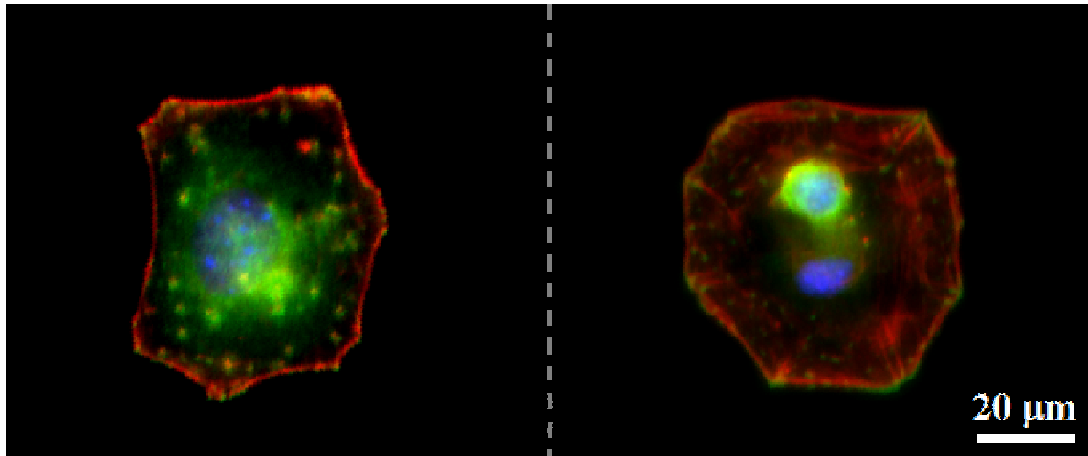
Figure 2.9 Representative fluorescent micrographs of 3T3 Swiss Albino fibroblasts on immobilized cyclic oxyamine-terminated RGD nanoarrays. Cells were stained for nuclei (blue), actin (red), and paxillin (green). The majority of the focal adhesions (green dots) are distributed throughout the cells.

and cyclic RGD peptides could possibly be due to the difference in these two steps. In adherent cells on linear RGD peptides, the integrin receptors are more mobile as a result of the lower affinity (lower K_d). Therefore, the nucleation of focal adhesions is decreased, while the growth of focal adhesions is increased. This results in fewer mature focal adhesions in the cells. On the other hand, in cells adhered to cyclic RGD peptides, there is increased nucleation of focal adhesions, because it takes fewer clustered integrin receptors to form clusters due to the higher affinity of the ligand. However, the growth of the focal adhesions is slower, resulting in more numerous, yet smaller focal adhesions distributed throughout the cell.

2.4 Conclusions

It was determined that the combination of the patterning of electroactive SAMs through DPN, a chemoselective immobilization strategy, and high-resolution fluorescence microscopy is a valid method to study single cell adhesion. The difference in integrin receptor affinity for linear and cyclic RGD peptides was shown to have a dramatic affect on the organization of intracellular nanoarchitecture in adherent fibroblasts. This work shows promise in a range of applications in the fields of drug discovery and live-cell migration studies. These future directions will be described in further detail in Chapter 5.

REFERENCES

(1)   Ulman, A. Formation and structure of self-assembled monolayers. *Chem. Rev.* **1996**, 96, 1533-1554.

(2)   Nuzzo, R. G.; Allara, D. L. Adsorption of bifunctional organic disulfides on gold surfaces. *J. Am. Chem. Soc.* **1983**, 105, 4481-4483.

(3)   Schreiber, F. Self-assembled monolayers: from 'simple' model systems to biofunctionalized interfaces. *J. Phys.: Condens. Matter* **2004**, 16, R881-R900.

(4)   Mrksich, M.; Whitesides, G. M. Using self-assembled monolayers to understand the interactions of man-made surfaces with proteins and cells. *Annu. Rev. Biophys. Biomol. Struct.* **1996**, 25, 55-78.

(5)   Dubois, L. H.; Nuzzo, R. G. Synthesis, structure, and properties of model organic surfaces. *Ann. Rev. Phys. Chem.* **1992**, 43, 437-463.

(6)   Love, J. C.; Estroff, L. A.; Kriebel, J. K.; Nuzzo, R. G.; Whitesides, G. M. Self-assembled monolayers of thiolates on metals as a form of nanotechnology. *Chem. Rev.* **2005**, 105, 1103-1170.

(7)   Kingshott, P.; Griesser, H. J. Surfaces that resist bioadhesion. *Curr. Opin. Solid State Mater. Sci.* **1999**, 4, 403-412.

(8)   Prime, K. L.; Whitesides, G. M. Self-assembled organic monolayers: model systems for studying adsorption of proteins at surfaces. *Science* **1991***, 252*, 1164-1167.

(9)   Jiang, X.; Bruzewicz, D. A.; Thant, M. M.; Whitesides, G. M. Palladium as a substrate for self-assembled monolayers used in biotechnology. *Anal. Chem.* **2004**, 76, 6116-6121.

(10)   Harder, P.; Grunze, M.; Dahint, R.; Whitesides, G. M.; Laibinis, P. E. Molecular conformation in oligo(ethylene glycol)-terminated self-assembled monolayers on gold and silver surfaces determines their ability to resist protein adsorption. *J. Phys. Chem. B* **1998**, 102, 426-436.

(11)   Herrwerth, S.; Eck, W.; Reinhardt, S.; Grunze, M. Factors that determine the protein resistance of oligoether self-assembled monolayers – internal hydrophilicity, terminal hydrophilicity, and lateral packing density. *J. Am. Chem. Soc.* **2003**, 125, 9359-9366.

(12)   Chan, E. W. L.; Yousaf, M. N. Immobilization of ligands with precise control of density to electroactive surfaces. *J. Am. Chem. Soc.* **2006**, 128, 15542-15546.

(13)   Park, S.; Yousaf, M. N. An interfacial oxime reaction to immobilize ligands and cells in patterns and gradients to photoactive surfaces. *Langmuir* **2008,** *24*(12), 6201-6207.

(14)   Westcott, N. P.; Yousaf, M. N. Synergistic microfluidic and electrochemical strategy to activate and pattern surfaces selectively with ligands and cell. *Langmuir,* **2008,** *24*(6), 2261-2265.

(15)   Chan, E. W. L.; Park, S.; Yousaf, M. N. An electroactive catalytic dynamic substrate that immobilizes and releases patterned ligands, proteins, and cells. *Angew. Chem.-Int. Edit.* **2008,** *47*(33), 6267-6271.

(16)   Lamb, B. M.; Westcott, N. P.; Yousaf, M. N. Microfluidic lithography to create dynamic gradient SAM surfaces for spatio-temporal control of directed cell migration. *ChemBioChem* **2008,** *9*(16), 2628-2632.

(17)   Piner, R. D.; Zhu, J.; Xu, F.; Hong, S. H.; Mirkin, C. A. "Dip-pen" nanolithography. *Science* **1999**, 283, 661-663.

(18)   Mirkin, C. A.; Hong, S. H.; Demers, L. Dip-pen nanolithography: Controlling surface architecture on the sub-100 nanometer length scale. *ChemPhysChem* **2001**, 2, 37-39.

(19)   Rozhok, S.; Piner, R.; Mirkin, C. A. Dip-pen nanolithography: what controls ink transport? *J. Phys. Chem. B* **2003**, 107, 751-757.

(20)   Ginger, D. S.; Zhang, H.; Mirkin, C. A. The evolution of dip-pen nanolithography. *Angew. Chem. Int. Ed.* **2004**, 43, 30-45.

(21)   Hodgson, L.; Chan, E. W. L.; Hahn, K. M.; Yousaf, M. N. Combining surface chemistry with a FRET-based biosensor to study the dynamics of RhoA GTPase activation in cells on patterned substrates. *J. Am. Chem. Soc.* **2007**, 129, 9264-9265.

(22)   Todaro, G. L.; Green, H. Quantitative studies of the growth of mouse embryo cells in culture and their development into established lines. *J. Cell Biol.* **1963**, 17, 299-313.

(23)   Hong, H.G.; Park, W.; Yu, E. Voltammetric determination of electron transfer kinetic parameters in hydroquinone-terminated self-assembled monolayers on gold. *J. Electroanal. Chem.* **1999,** 476(2), 177-181.

(24) Hong, H.G.; Park, W. Electrochemical characteristics of hydroquinone-terminated self-assembled monolayers on gold. *Langmuir.* **2001,** 17(8), 2485-2492.

(25) Hoover, D.K.; Lee, E.-J.; Chan, E.W.L.; Yousaf, M.N. Electroactive nanoarrays for biospecific ligand mediated studies of cell adhesion. *ChemBioChem* **2007,** 8(16), 1920-1923.

(26) Turner, C. E.; Glenney, J. R.,Jr.; Burridge, K. Paxillin: A new vinculin-binding protein present in focal adhesions. *J. Cell Biol.* **1990**, 111, 1059-1068.

(27) Hynes, R. O. The emergence of integrins: a personal and historical perspective. *Matrix Biol.* **2004**, 23, 333-340.

(28) Kumagai, H.; Tajima, M.; Ueno, Y.; Giga-Hama, Y.; Ohba, M. Effect of cyclic RGD peptides on cell adhesion and tumor metastasis. *Biochem. Biophys. Res. Comm.* **1991,** 177, 74-82.

(29) Kato, M.; Mrksich, M. Using model substrates to study the dependence of focal adhesion formation on the affinity of integrin–ligand complexes. *Biochem. (N.Y.)* **2004**, 43, 2699-2707.

CHAPTER 3

ASYMMETRIC ELECTROACTIVE NANOARRAYS FOR SINGLE CELL POLARIZATION STUDIES

3.1 Introduction

3.1.1 Cell polarity: asymmetry in form and function. The simplest definition of cell polarization is the establishment of morphologically and functionally distinguishable regions of the internal structures of the cell.[1] The proper operation of this process is vital in many biological phenomena, as was described in Chapter 1 (Section 1.1.1). The ability to polarize has been shown to be important in a wide range of cell types, from simple budding yeast to specialized eukaryotic cells including epithelial cells, fibroblasts, helper T cells, and neurons.[2-5] While the molecular mechanism is thought to be highly conserved in eukaryotic cells,[6] there have been extensive studies demonstrating that many of the pathways and components involved are specific in relation to the cell line under study, as well as experimental conditions.[7,8]

Polarization is an essential step in cell migration. In order to move in a directional manner, the cell must adopt and maintain a polarized shape. This asymmetry manifests as a polarization of several key organelles, resulting in a distinctive cell front and rear.[9-11] A depiction of a polarized, migratory fibroblast is shown in Figure 3.1. The leading edge of the cell is characterized by the presence of protrusions of the plasma membrane; flattened, wide projections known as lamellipodia, and smaller, spike-like filopodia. These membrane extensions are driven primarily by
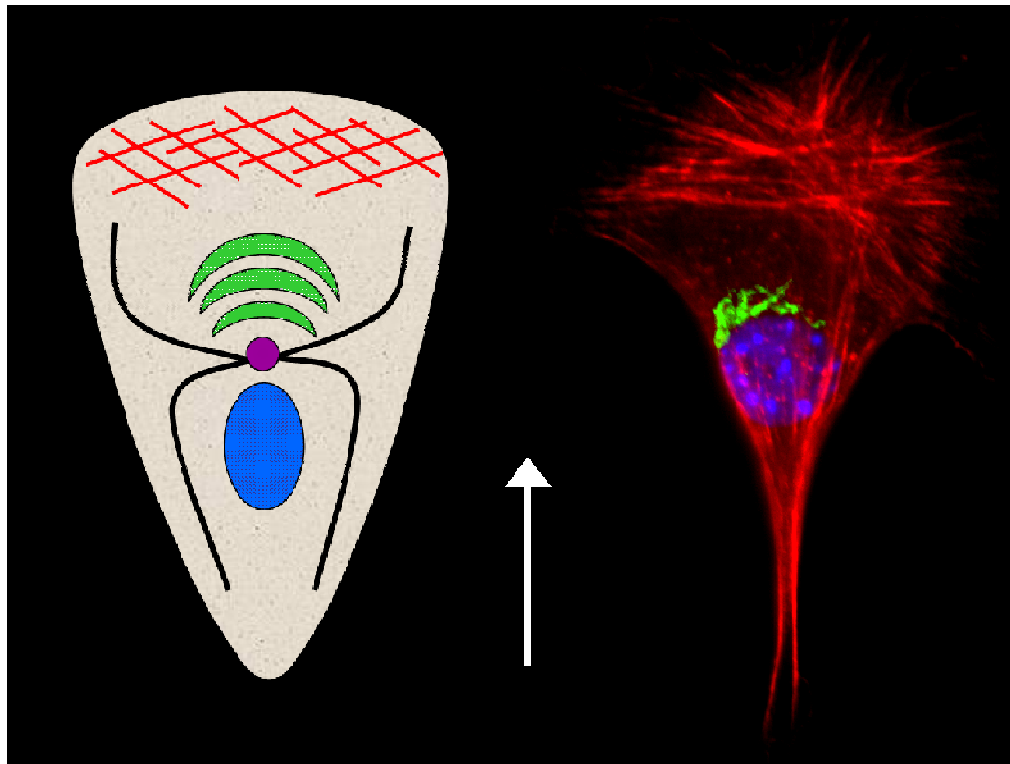
Figure 3.1 (Left) Schematic depiction of a polarized fibroblast. The cell is depicted with a condensed Golgi apparatus (green) and MTOC (purple) located forward of the nucleus (blue), towards the leading edge of the cell. This indicates that there is net cell polarity in the direction of migration (indicated by the white arrow). The microtubule network is shown in black, and the dense concentration of actin cytoskeleton associated with lamellipodial extension is shown in red. **(Right)** Micrograph of a polarized 3T3 Swiss Albino mouse fibroblast showing the nucleus (blue), Golgi apparatus (green), and the actin cytoskeleton (red). As evidenced by the extended morphology, and placement of the condensed Golgi apparatus relative to the nucleus, the cell was migrating in the direction of the white arrow.

actin polymerization, which in turn is dependent on a variety of signaling pathways.[12,13] Several other cytoplasmic organelles are thought to be involved in the development of cell polarization in fibroblasts. These are discussed in more detail below.

3.1.2 Experimental markers of cell polarization in fibroblasts. The flattened protrusions of the cellular plasma membrane know as lamellipodia are typically ~2 – 5 μm in width.[14] This projection is supported by the polymerization of a network of actin filaments that exclude, for the most part, other cytoplasmic organelles. This concentration of actin polymerization at the leading edge of the cell is countered by a decrease in the amount of actin filaments in the rear edge of the cell, which is accomplished by selective depolymerization of existing filaments. The actin filaments in the cell that are not directly involved in lamellopodial extension or retraction of the cell rear are organized in such a way as to support the rest of the cell body.[14,15] The extension of lamellopodia and retraction of the cell rear are all closely involved with cell adhesion, previously discussed in Chapters 1 and 2.

In addition to the actin cytoskeleton, the microtubule network is involved in cell polarization. It has been shown that cell polarization can be disrupted by the use of microtubule-depolymerizing drugs.[1,14] The number and arrangement of microtubules is commonly controlled by a structure known as the centrosome. The centrosome is one type of microtubule-organizing center (MTOC) that is comprised of a pair of centrioles containing γ-tubulin, surrounded by an amorphous collection of proteins.[16,17] The MTOC has been found to be critical in a range of cellular functions and organization. A major example is the arrangement of several membrane-bound

organelles including the nucleus, Golgi apparatus, and endoplasmic reticulum during cytokinesis (cell division), as well as possible connections in cell polarization.[18]

In migrating fibroblasts, both the MTOC and the Golgi apparatus are often reoriented in front of the nucleus, towards the leading edge of the cell. It is thought that the reorientation of the Golgi apparatus in the direction of cell movement is a response to intracellular signals for new membrane components at the leading edge of the cell. These components can be provided through increased vesicular transport from the Golgi apparatus, mediated by the microtubule network.[19,20] However, it has also been shown that some cell lines (*e.g.* mammalian neutrophils and *Dictyostelium* ameobae*)* do not always reorient the MTOC in this manner, inferring dependence on culturing conditions and substrate geometries.[21-23] Regardless, the Golgi apparatus and MTOC are known to co-localize in many cell types, including NIH-3T3 fibroblasts.[24]

The nucleus of cells is known to shift position in the cytoplasm of many cell types, although the mechanism and driving force behind such movements are not always clear. In animal cells, the nuclear membrane is thought to interact with microtubules, which may be involved in the positioning of both the nucleus and the MTOC.[25] The repositioning of the nucleus of cells is also typically used as a marker of cell polarization. The nucleus has been used as a reference point in order to observe the organization of other organelles, including the Golgi apparatus and the MTOC.[13]

3.1.3 Previous studies of cell polarization in fibroblasts. Many of the fundamental studies of cell polarization have been performed using wound-healing assays. In

these experiments adherent cells are grown to confluence on a flat substrate, then the cell monolayer is manually disrupted, creating an artificial wound. The reorganization of organelles, establishment of cell polarization, and subsequent migration of cells at the edge of the experimental wound are then observed through immunofluorescence staining and microscopy.[7,19,20] The Yousaf group has also reported the study of cell polarization on patterns presenting biospecific RGD peptides in gradients.[26] In these studies, the polarization that occurs is due not only to cell-substrate interactions, but also cell-cell interactions. To remedy this, several groups have attempted to produce patterned substrates such that the cell-cell interactions would be reduced or removed completely.

Whitesides and coworkers have produced cell adhesive patterns of various shapes to observe the effect of geometry and surface constraint on lamellipodial extension. Lamellipodia were found to preferentially extend from the corners of the patterns.[27,28] In an extension of this work, Whitesides *et al.* produced asymmetric micropatterns of hydrophobic SAMs on gold to probe the relationship between imposed cell polarity and cell migration direction. In this work, it was demonstrated that the cell migration direction can be controlled by the direction of the imposed cell polarity following electrochemical desorption of the hydrophobic SAMs.[29] Finally, Théry *et al.* have probed the relationship between cell polarization and the position of adhesive and non-adhesive areas in single cells. Various shapes presenting fibronectin, an ECM protein, were produced in order to ascertain how the organelles and cytoskeletal elements reorganize in response to asymmetry in the microenvironment of the cell.[30]

In order to probe the effects of the spatial distribution and ligand affinity of biospecific cell adhesive ligands on single cell polarity, the DPN methodology developed in Chapter 2 will be used to produce symmetric and asymmetric nanopatterns. This technique will be combined with immunofluorescence microscopy of several key organelles, including the nucleus, Golgi apparatus, actin cytoskeleton, and focal adhesions, in order to observe cell polarization in single, adherent fibroblasts. Therefore, the effects of the spatial distribution of biospecific ligands on single cell polarity can be examined in the absence of cell-cell contact.

3.2 Experimental Materials and Methods

3.2.1 Design and production of asymmetric nanoarrays for single cell polarization studies. Square nanoarrays with an asymmetric distribution of spots were produced *via* DPN on bare gold using H_2Q-C_{11}-SH as ink, with a total patterned area of 60 μm x 60 μm, as shown in Figure 3.2. The higher density region was a 20 x 10 nanoarray (3.0 μm pitch), while the lower density region was a 10 x 5 nanoarray (6 μm pitch), both with ~500 nm diameter spots. The nanoarrays were imaged directly following printing at a scan rate of 4 Hz. The remaining exposed areas of gold were passivated by immersing the substrate in a solution of EG_4-C_{11}-SH (1 mM in ethanol, 12 h). The patterned substrates were either stored in H_2O before use, or were hydrated in H_2O for 1 – 1.5 h prior to immediate ligand immobilization. Following electrochemical oxidation of the hydroquinone-presenting asymmetric nanoarrays to the corresponding quinone (750 mV vs. Ag/AgCl, 15 s, 1.0 M $HClO_4$), linear or cyclic RGD peptide was immobilized as previously described.
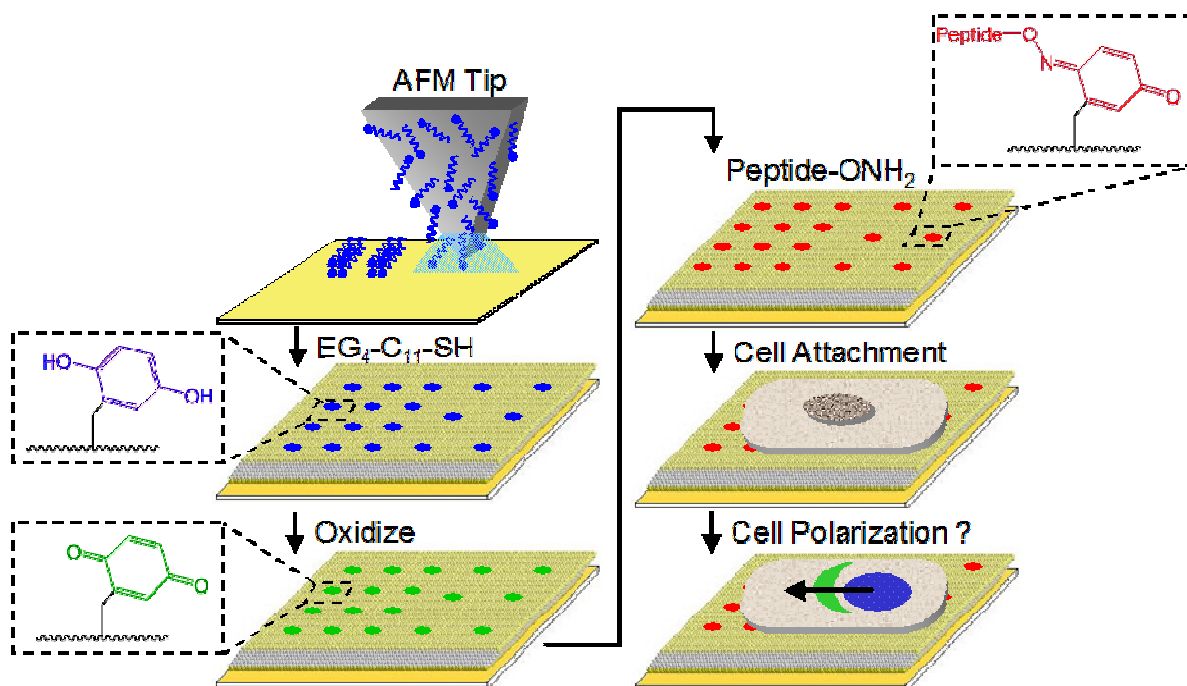
Figure 3.2 Schematic diagram of the production of asymmetric electroactive nanoarrays. An asymmetric nanoarray of H_2Q-C_{11}-SH was produced on gold *via* DPN, and the remaining non-patterned gold surface was passivated by immersion in a solution of EG_4-C_{11}-SH. The H_2Q-C_{11}-SH asymmetric nanoarrays were then electrochemically oxidized to the corresponding quinone, and an oxyamine-terminated peptide ligand was chemoselectively immobilized. Fibroblasts are then seeded and stained with several fluorescent dyes in order to evaluate cell polarization.

3.2.2 Cell seeding and staining techniques. 3T3 Swiss Albino mouse fibroblasts were obtained from the Tissue Culture Facility at the University of North Carolina at Chapel Hill. DMEM, bovine calf serum, Dulbecco's PBS, Triton X − 100, DAPI and phalloidin-TRITC were purchased from Sigma, and paraformaldehyde solution (32%) was purchased from Fisher. Penicillin/streptomycin were purchased from Gibco and mouse anti-paxillin antibody was purchased from B D Biosciences (San Jose, CA). Normal goat serum, FITC-conjugated goat anti-rabbit IgG and Cy-2 conjugated goat anti-mouse IgG were purchased from Jackson ImmunoResearch Laboratories, Inc. (West Grove, PA). Rabbit polyclonal anti-giantin primary antibody was purchased from Covance Research Products (Berkeley, CA), and fluorescence mounting medium was purchased from Dako (Carpinteria, CA).

3T3 Swiss Albino mouse fibroblasts were seeded on the patterned substrates in serum-free DMEM for 3 h, followed by incubation for 5 h in DMEM containing 10% bovine calf serum and 1% penicillin/streptomycin (37 ºC, 5% CO_2 atmosphere). The patterned cells were then fixed with formaldehyde (3.2% in PBS) and permeated in PBS containing 0.1% Triton X − 100. All fluorescent dye mixtures were made in PBS containing 5% normal goat serum and 0.1% Triton X −100. The substrates were placed in a humidified chamber and incubated with the first dye mixture (rabbit anti-giantin, 1:400 dilution; phalloidin-TRITC, 1:250 dilution) for 2 h, washed with PBS (3 x 10 min), and incubated with a second dye mixture (DAPI, 1:500 dilution; phalloidin-TRITC, 1:50 dilution; FITC conjugated goat anti-rabbit IgG, 1:400 dilution). The substrates were then secured gold-coated side down in fluorescence mounting medium on a glass coverslip.

3.2.3 High-resolution fluorescence microscopy. All fluorescence images were taken with a Nikon Eclipse TE2000-E inverted microscope (Nikon USA, Inc., Melville, NY) and a Plan Fluor 40X oil immersion objective (1.30 NA, Nikon USA). Immersion oil was purchased from Carl Zeiss MicroImaging, Inc. (Thornwood, NY) and lens paper was purchased from Fisher. Image analysis was performed using MetaMorph software (Molecular Devices, Downingtown, PA).

3.2.4 Focal adhesion studies on asymmetric nanoarrays. Asymmetric nanoarrays were produced as described above, and linear RGD peptide was immobilized. 3T3 Swiss Albino mouse fibroblasts were seeded and fixed as previously described. The substrates were placed in a humidified chamber and incubated with the first dye mixture (mouse anti-paxillin, 1:200 dilution; phalloidin-TRITC, 1:250 dilution) for 2 h, washed with PBS (3 x 10 min), and incubated with the second dye mixture (DAPI, 1:500 dilution; phalloidin-TRITC, 1:50 dilution; Cy-2 conjugated goat anti-mouse IgG, 1:200 dilution). Following staining, the substrates were secured in fluorescence mounting medium and imaged by fluorescence microscopy.

3.3 Results and Discussion[31]

3.3.1 Design and LFM characterization of asymmetric nanoarrays. Asymmetric nanoarrays of H_2Q-C_{11}-SH were patterned as described above. The biospecific ligands were presented such that there was ~4 fold more cell adhesive area in the higher density region of the nanoarray, as shown in Figure 3.3A. The nanoarray was imaged directly following patterning by DPN at a scan rate of 4 Hz. An expanded region of an asymmetric nanoarray is shown in the LFM image in Figure 3.3B.
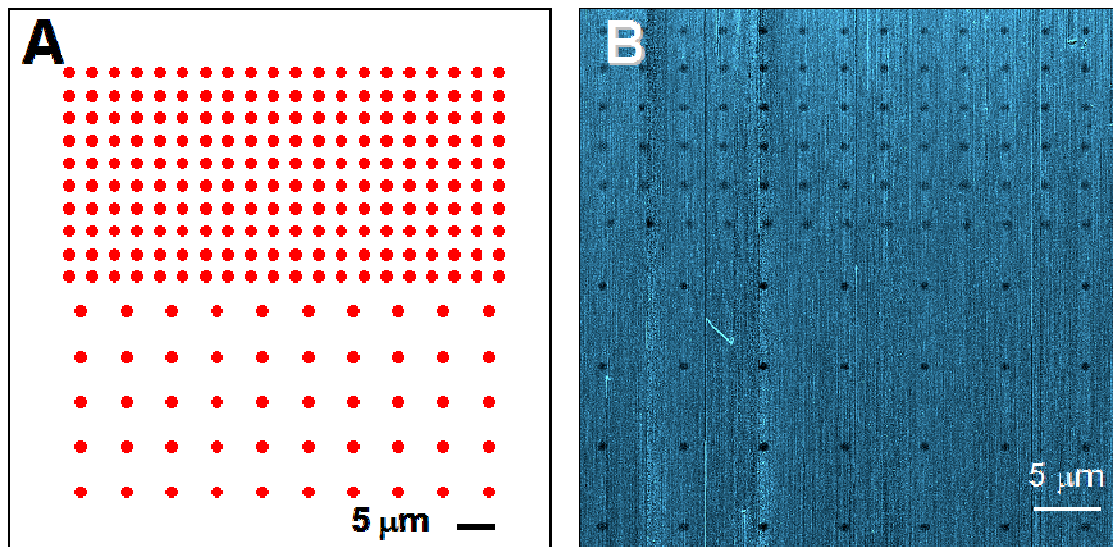
Figure 3.3 Design of asymmetric electroactive nanoarrays for studies of single cell polarization. **(A)** A diagram of the entire asymmetric nanoarray composed of two regions: a higher density region (20 x 10, 3 μm pitch, ~500 nm diameter spots) and a lower density region (10 x 5, 6 μm pitch, ~500 nm diameter spots) for a total patterned area of ~60 μm x ~60 μm. **(B)** A LFM image of an expanded area of this asymmetric nanoarray.

3.3.2 Single cell polarization studies on symmetric nanoarrays presenting linear RGD peptide. It has been proposed that cells can spontaneously polarize in environments that present a certain stimulus in a macroscopically homogenous way.[9] This may be a result of cellular perception of gradients of stimuli in microscopic defects in the homogenous environment. This implies that a population of cells in a homogenous environment would be randomly polarized, with no net cell polarity in any specific direction. In order to test this hypothesis, symmetric nanoarrays of H_2Q-C_{11}-SH were produced (20 x 20, 3 μm pitch, ~500 nm diameter spots), with a total patterned area of ~60 μm x ~60 μm. Linear RGD peptide was immobilized, and 3T3 Swiss Albino mouse fibroblasts were seeded on the surface for a total of 8 h, then fixed and stained for several markers of cell polarization: the nucleus, Golgi apparatus, and actin cytoskeleton. An antibody targeting giantin, an integral membrane protein found in the cisternae of the Golgi apparatus, was used to visualize this organelle.[32]

Figure 3.4 shows representative micrographs of adherent fibroblasts on symmetric electroactive nanoarrays presenting linear RGD peptide. The cells adopt a square morphology, closely corresponding to the total patterned area of the nanoarray (~60 μm x ~60 μm). The nuclei was found approximately in the cell center in cells adhered to symmetric nanoarrays. In some instances the Golgi apparatus was condensed to one side of the nucleus, indicative of cell polarity. However, in most cases the Golgi apparatus was diffusely distributed surrounding the nucleus, strongly suggesting that there was no net directional cell polarization in fibroblasts on symmetric nanoarrays presenting linear RGD peptide. This signifies that the cells
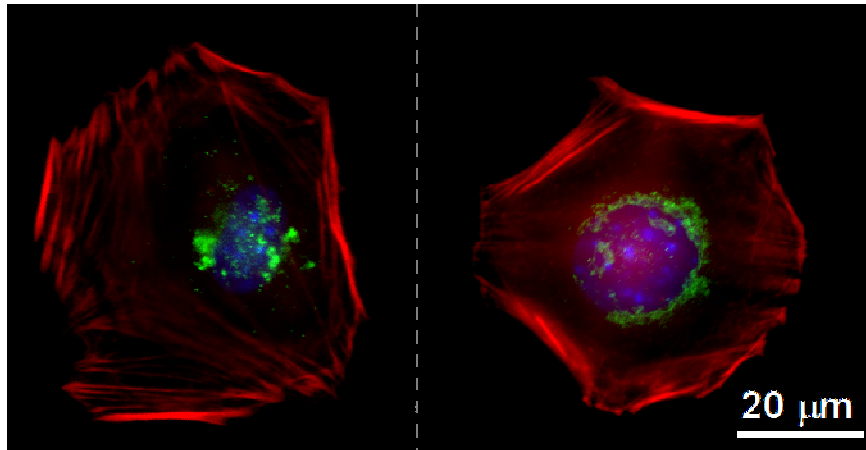
Figure 3.4 Representative micrographs of 3T3 Swiss Albino fibroblasts adhered to symmetric nanoarrays (20 x 20, 3 μm pitch, ~500 nm diameter spots) presenting immobilized linear RGD peptide, and stained for cell polarization. The cells were visualized using three fluorescent dyes: DAPI (nuclei, blue), phalloidin-TRITC (actin cytoskeleton, red), and anti-giantin followed by FITC secondary antibody (Golgi apparatus, green). There was no net directional cell polarity observed, as evidenced by the diffuse distribution of the Golgi apparatus surrounding the cell nuclei.

may polarize in random directions in an effort to escape the constraining nanoarray. However, the lack of net directional polarity also indicates that there is no specific direction that is favored in the case of a symmetric nanoarray presenting the immobilized ligand in a homogenous manner.

3.3.3 Single cell polarization studies on asymmetric nanoarrays presenting linear RGD peptide. The experimental design used to study single cell adhesion on asymmetric nanoarrays is shown in Figure 3.2. Briefly, an asymmetric nanoarray of H_2Q-C_{11}-SH was produced with a higher density region (20 x 10, 3.0 μm pitch, ~500 nm diameter spots) and a lower density region (10 x 5, 6 μm pitch, ~500 nm diameter spots). Following electrochemical oxidation and chemoselective immobilization of ligand, 3T3 Swiss Albino mouse fibroblasts were seeded for 8 h and imaged.

The representative micrographs in Figure 3.5 show single fibroblasts adhered to asymmetric nanoarrays presenting linear RGD peptide. The cells generally adopt a shape and size corresponding to the total patterned area of the nanoarray (~60 μm x ~60 μm). The position of the nuclei and the presence of the concentrated Golgi apparatus forward of the nuclei demonstrate that the cells are polarized towards the higher density region of the nanoarray. When a vector is drawn between the center of the nucleus and that of the condensed Golgi apparatus, the net vector found is directed towards the higher density region of the asymmetric nanoarray, indicating that there is a net directional cell polarization towards the higher density region of the nanoarray. This result, taken in conjunction with the lack of directional cell polarity found on symmetric nanoarrays presenting the same ligand, leads to the
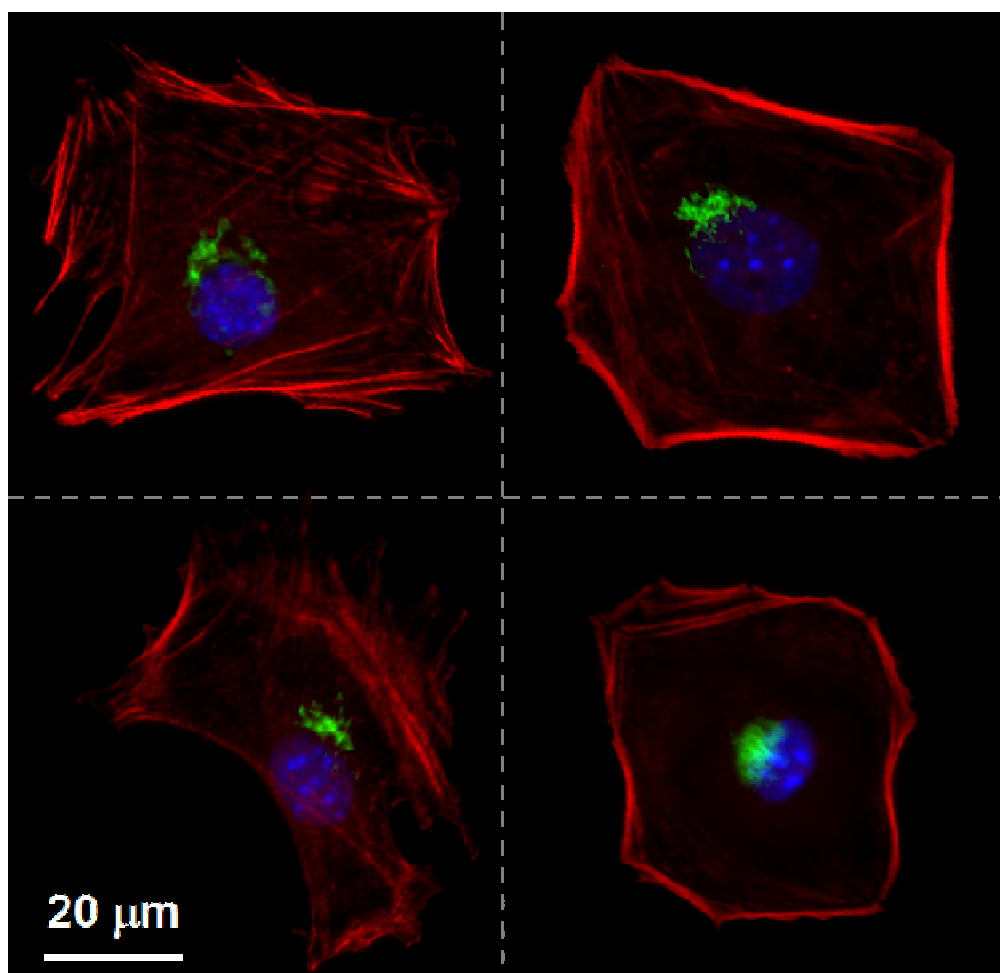
Figure 3.5 Representative micrographs of 3T3 Swiss Albino fibroblasts adhered to asymmetric nanoarrays presenting immobilized linear RGD peptide. The higher density region of the asymmetric nanoarrays was situated toward the top of the figure. The cells have been visualized using three fluorescent dyes: DAPI (nuclei, blue), phalloidin-TRITC (actin cytoskeleton, red), and anti-giantin followed by FITC secondary antibody (Golgi apparatus, green). As can be seen in these micrographs, there is a net directional cell polarity towards the higher density region of the asymmetric nanoarray as evidenced by the relative orientation of the condensed Golgi apparatus structure with respect to the nuclei.

conclusion that the nanoscale spatial distribution of cell adhesive ligands can induce directional cell polarization in fibroblasts.

3.3.4 The effect of ligand affinity on single cell polarization on asymmetric nanoarrays. Integrin receptors are known to have a higher affinity to cyclic RGD peptide than to linear RGD peptide (K_d of nM and μM, respectively).[33] Therefore, cyclic RGD peptide was immobilized to asymmetric nanoarrays were produced with identical features as those described above in order to study the effects of ligand affinity on single cell polarization. 3T3 Swiss Albino fibroblasts were seeded, and stained for cell polarity markers.

Figure 3.6 shows representative micrographs of single fibroblasts adhered to asymmetric nanoarrays presenting cyclic RGD peptide. The cells have assumed a square morphology of approximately the size of the total patterned area of a single nanoarray (~60 μm x ~60 μm). It was found that on single asymmetric nanoarrays presenting cyclic RGD peptide, the Golgi apparatus is found to be diffuse and distributed around the nuclei, with no net directional cell polarization towards the higher density region of array. This is in stark contrast to the net directional cell polarization observed on asymmetric nanoarrays of linear RGD peptide, suggesting that the higher ligand affinity for cyclic RGD peptide overrides the effects of spatial presentation on cell polarization. In order to examine this phenomenon in more detail, a double asymmetric nanoarray was designed and is discussed in more detail below.

3.3.5 The effects of ligand spatial distribution on single cell polarization on double asymmetric nanoarrays presenting cyclic RGD peptide. In order to create a more
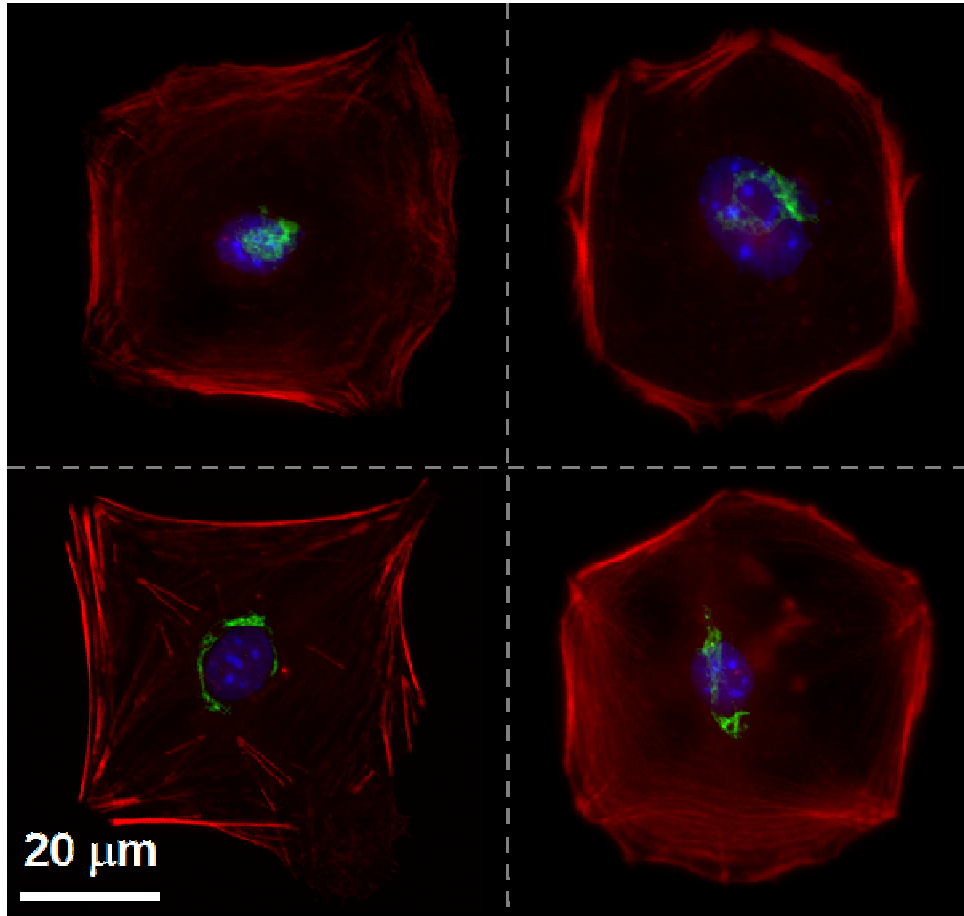
Figure 3.6 Representative micrographs of 3T3 Swiss Albino fibroblasts adhered to asymmetric nanoarrays presenting cyclic RGD peptide. The higher density region of the asymmetric nanoarrays was situated toward the top of the figure. The cells have been visualized using three fluorescent dyes: DAPI (nuclei, blue), phalloidin-TRITC (actin cytoskeleton, red), and anti-giantin followed by FITC secondary antibody (Golgi apparatus, green). As can be seen in these micrographs, there is no net directional cell polarity towards the higher density region of the asymmetric nanoarray as evidenced by the diffuse Golgi apparatus structures surrounding the nuclei.

dramatic difference in cell adhesive area, a double asymmetric nanoarray was designed, consisting of a higher density region (20 x 10, 3 μm pitch, ~500 nm diameter spots), and a lower density region (10 x 5, 6 μm pitch, ~250 nm diameter spots), as shown in Figure 3.7. Double asymmetric nanoarrays were produced *via* DPN and cyclic RGD peptide was immobilized as previously described. 3T3 Swiss Albino fibroblasts were seeded, and stained for cell polarity markers. Several representative micrographs of adherent fibroblasts on double asymmetric nanoarrays are shown in Figure 3.7. The placement of the condensed Golgi apparatus and the nuclei indicate that the cells are polarized toward the higher density region of the double asymmetric nanoarray. Thus, the cells can distinguish the ~8 fold difference in cell adhesive ligand area presented across the nanoarray. This reveals that there may be a subtle relationship between spatial distribution and ligand affinity in the establishment and retention of directional cell polarization in fibroblasts.

3.3.6 The effect of ligand affinity on focal adhesion formation in single cells on asymmetric nanoarrays. Asymmetric nanoarrays were used to examine the influence of both the spatial presentation of immobilized ligand and ligand affinity on focal adhesion formation in adherent cells. Asymmetric nanoarrays were produced with the feature sizes previously described and linear or cyclic RGD peptide was immobilized. 3T3 Swiss Albino fibroblasts were seeded and stained for focal adhesions by visualizing paxillin, a focal adhesion protein.[34]

Figure 3.8 show representative micrographs of fibroblasts adhered to asymmetric nanoarrays of identical feature size, presenting a lower affinity ligand, linear RGD
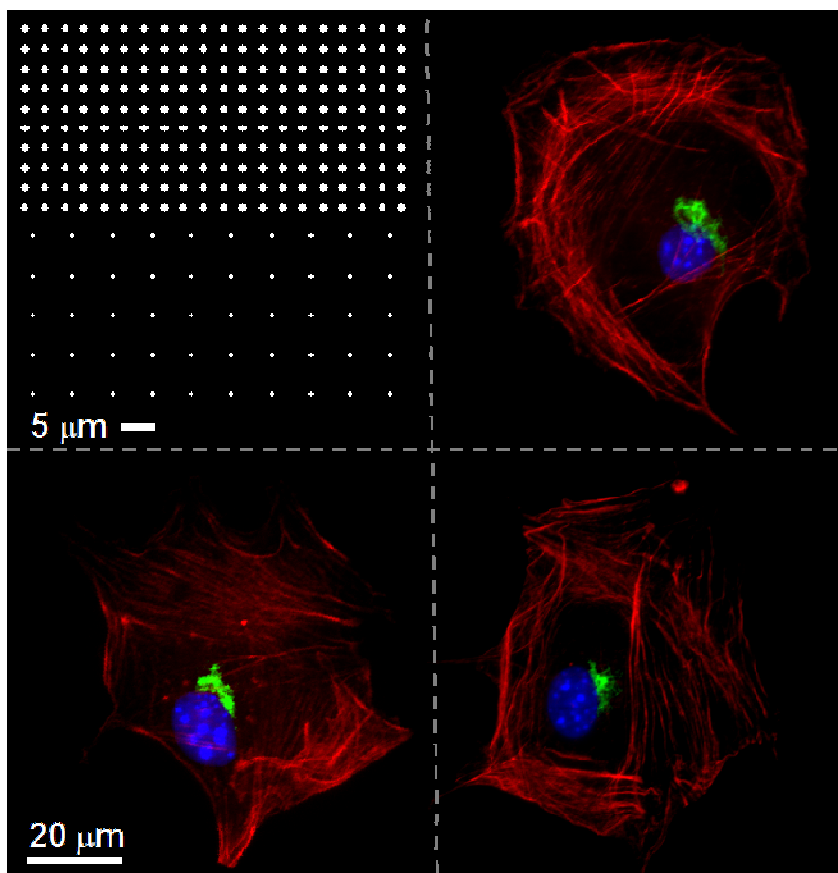
Figure 3.7 Double asymmetric nanoarrays for single cell studies of cell polarization. **(Top left)** The double asymmetric nanoarray is produced with a higher density region (20 x 10, 3 μm pitch, ~500 nm diameter spots) and a lower density region (10 x 5, 6 μm, ~250 nm diameter spots), for a total patterned area of ~60 μm x ~60 μm. Representative micrographs of 3T3 Swiss Albino fibroblasts adhered to double asymmetric nanoarrays presenting immobilized cyclic RGD peptide. The cells have been stained with fluorescent dyes: DAPI (nuclei, blue), phalloidin-TRITC (actin cytoskeleton, red), and anti-giantin followed by FITC secondary antibody (Golgi apparatus, green). Interestingly, there is net directional cell polarity in the direction of the higher density region of the nanoarray.
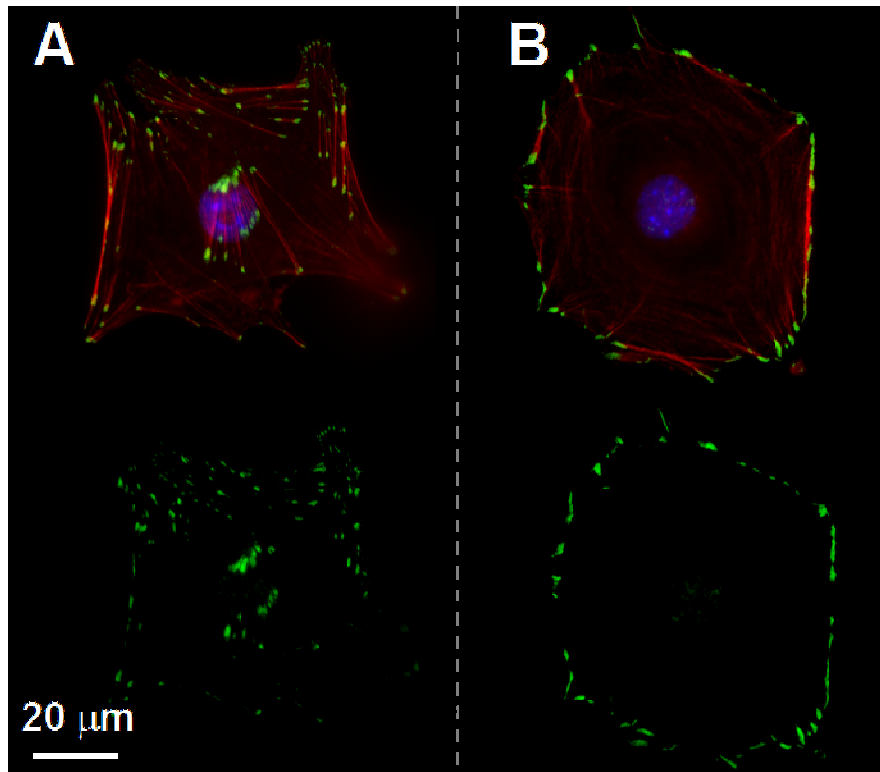
Figure 3.8 Representative micrographs of 3T3 Swiss Albino fibroblasts adhered to asymmetric nanoarrays presenting lower affinity linear RGD peptide **(A)** and higher affinity cyclic RGD peptide **(B)** and stained for focal adhesions. The higher density region of the asymmetric nanoarrays was situated toward the top of the figure. The cells have been visualized using three fluorescent dyes: DAPI (nuclei, blue), phalloidin-TRITC (actin cytoskeleton, red), and anti-paxillin followed by fluorescent Cy-2 secondary antibody (focal adhesions, green). When only the focal adhesion staining is compared (A and B, bottom), the difference in focal adhesion distribution is quite apparent.

(Figure 3.8A), and a higher affinity ligand, cyclic RGD (Figure 3.8B). As can be clearly seen in the lower images showing only the green paxillin staining, there is an increase in focal adhesion formation correlating to the higher density region of the asymmetric nanoarray presenting linear RGD. Interestingly, there is no such increase in focal adhesion formation on an asymmetric nanoarray of the same dimensions presenting cyclic RGD peptide, a higher affinity ligand. This is in agreement with the observations mentioned previously that adherent cells on single asymmetric nanoarrays presenting cyclic RGD peptide did not show directional cell polarization. While asymmetric focal adhesion distribution is not an indication of cell polarization *per se*, it is expected that there will be increased focal adhesion formation at the leading edge of a polarized cell.[9,35]

3.4 Conclusions

Asymmetric nanoarrays with various spot diameters and distributions were produced to study single cell polarization. It was found that while there was no net directional cell polarity found in symmetric nanoarrays presenting linear RGD peptide, asymmetric nanoarrays presenting the same ligand were found to induce net directional cell polarization in adherent fibroblasts. This demonstrates the effect that the spatial distribution of cell adhesive ligand has on the establishment and maintenance of directional cell polarization. There was no net directional cell polarity found on asymmetric nanoarrays presenting cyclic RGD peptide, a higher affinity ligand than linear RGD, thus indicating that ligand affinity also has a profound effect

71

on cell polarization. The relationship between ligand affinity and spatial distribution of immobilized ligand was explored through the development of double asymmetric nanoarrays presenting cyclic RGD, which were shown to impose directional cell polarization. In conclusion, asymmetric nanoarrays produced by DPN, in conjunction with the quinone-based chemoselective immobilization strategy developed, were demonstrated to be a powerful platform for studies aimed at investigating the effects of ligand affinity and ligand spatial distribution on many facets of cell polarization in fibroblasts.

REFERENCES

(1)   Nabi, I. The polarization of the motile cell. *J. Cell. Sci.* **1999**, *112*, 1803-1811.

(2)   Poo, W.-J.; Conrad, L.; Janeway, C. A., Jr. Receptor-directed focusing of lymphokine release by helper T cells. *Nature* **1988**, *332*, 378-380.

(3)   Eaton, S.; Simons, K. Apical, basal, and lateral cues for epithelial polarization. *Cell* **1995**, *82*, 5-8.

(4)   Drubin, D. G.; Nelson, W. J. Origins of cell polarity. *Cell* **1996**, *84*, 335-344.

(5)   Dustin, M. L. Schmoos, rafts, and uropods – the many facets of cell polarity. *Cell* **2002**, *110*, 13-18.

(6)   Etienne-Manneville, S. Cdc42 - the centre of polarity. *J. Cell. Sci.* **2004**, *117*, 1291-1300.

(7)   Euteneuer, U.; Schliwa, M. Mechanism of centrosome positioning during the wound response in BSC-1 cells. *J. Cell Biol.* **1992**, *116*, 1157-1166.

(8)   Yvon, A. C.; Walker, J. W.; Danowski, B.; Fagerstrom, C.; Khodjakov, A.; Wadsworth, P. Centrosome reorientation in wound-edge cells is cell type specific. *Mol. Biol. Cell* **2002**, *13*, 1871-1880.

(9)   Lauffenburger, D. A.; Horwitz, A. F. Cell migration: a physically integrated molecular process. *Cell* **1996**, *84*, 359-369.

(10)   Mañes, S.; Mira, E.; Gomez-Mouton, C.; Lacalle, R. A.; Martinez-A, C. Cells on the move: a dialogue between polarization and motility. *IUBMB Life* **2000**, *49*, 89-96.

(11)   Etienne-Manneville, S.; Hall, A. Rho GTPases in cell biology. *Nature* **2002**, *420*, 629-635.

(12)   Ridley, A. J.; Schwartz, M. A.; Burridge, K.; Firtel, R. A.; Ginsberg, M. H.; Borisy, G.; Parsons, J. T.; Horwitz, A. R. Cell migration: integrating signals from front to back. *Science* **2003**, *302*, 1704-1709.

(13)   Vicente-Manzanares, M.; Webb, D. J.; Horwitz, A. R. Cell migration at a glance. *J. Cell. Sci.* **2005**, *118*, 4917-4919.

(14)   Small, J. V.; Geiger, B.; Kaverina, I.; Bershadsky, A. How do microtubules guide migrating cells? *Nat. Rev. Mol. Cell Biol.* **2002**, *3*, 957-964.

(15) Kole, T. P.; Tseng, Y.; Jiang, I.; Katz, J. L.; Wirtz, D. Intracellular mechanics of migrating fibroblasts. *Mol. Biol. Cell* **2005**, *16*, 328-338.

(16) Joshi, H. C. Microtubule organizing centers and γ-tubulin. *Curr. Opin. Cell Biol.* **1994**, 6, 55-62.

(17) Thyberg, J.; Moskalewski, S. Role of microtubules in the organization of the Golgi complex. *Exp. Cell Res.* **1999**, *246*, 263-279.

(18) Kellogg, D. R.; Moritz, M.; Alberts, B. M. The centrosome and cellular organization. *Annu. Rev. Biochem.* **1994**, *63*, 639-674.

(19) Kupfer, A.; Louvard, D.; Singer, S. J. Polarization of the Golgi apparatus and the microtubule-organizing center in cultured fibroblasts at the edge of an experimental wound. *Proc. Natl. Acad. Sci. U.S.A.* **1982**, *79*, 2603-2607.

(20) Bergmann, J. E.; Kupfer, A.; Singer, S. J. Membrane insertion at the leading edge of motile fibroblasts. *Proc. Natl. Acad. Sci. U.S.A.* **1983**, *80*, 1367-1371.

(21) Magdalena, J.; Millard, T. H.; Etienne-Manneville, S.; Launay, S.; Warwick, H. K.; Machesky, L. M. Involvement of the Arp2/3 complex and Scar2 in Golgi polarity in scratch wound models. *Mol. Biol. Cell* **2003**, *14*, 670-684.

(22) Mellor, H. Cell motility: Golgi signalling shapes up to ship out. *Curr. Biol.* **2004**, *14*, R435.

(23) Bornens, M. Organelle positioning and cell polarity. *Nat. Rev. Mol. Cell Biol.* **2008**, *9*, 874-886.

(24) Chabin-Brion, K.; Marceiller, J.; Perez, F.; Settegrana, C.; Drechou, A.; Durand, G.; Pous, C. The Golgi complex is a microtubule-organizing organelle. *Mol. Biol. Cell* **2001**, *12*, 2047-2060.

(25) Morris, N. R. Nuclear positioning: the means is at the ends. *Curr. Opin. Cell Biol.* **2003**, *15*, 54-59.

(26) Chan, E. W. L.; Yousaf, M. N. A photo-electroactive surface strategy for immobilizing ligands in patterns and gradients for studies of cell polarization. *Mol. BioSyst.* **2008,** *4,* 746-753.

(27) Parker, K. K.; Brock, A. L.; Brangwynne, C.; Mannix, R. J.; Wang, N.; Ostuni, E.; Geisse, N. A.; Adams, J. C.; Whitesides, G. M.; Ingber, D. E. Directional control of lamellipodia extension by constraining cell shape and orienting cell tractional forces. *FASEB J.* **2002**, *16*, 1195-1204.

(28)   Brock, A.; Chang, E.; Ho, C.; LeDuc, P.; Jiang, X.; Whitesides, G. M.; Ingber, D. E. Geometric determinants of directional cell motility revealed using microcontact printing. *Langmuir* **2003**, *19*, 1611-1617.

(29)   Jiang, X.; Bruzewicz, D. A.; Wong, A. P.; Piel, M.; Whitesides, G. M. Directing cell migration with asymmetric micropatterns. *Proc. Natl. Acad. Sci. U.S.A.* **2005**, *102*, 975-978.

(30)   Théry, M.; Racine, V.; Piel, M.; Pépin, A.; Dimitrov, A.; Chen, Y.; Sibarita, J.-B.; Bornens, M. Anisotropy of cell adhesive microenvironment governs cell internal organization and orientation of polarity. *Proc. Natl. Acad. Sci. U.S.A.* **2006**, *103*, 19771-19776.

(31)   Hoover, D. K.; Chan, E. W. L.; Yousaf, M. N. Asymmetric nanoarray peptide surfaces for studies of single cell polarization. *J. Am. Chem. Soc.* **2008,** *130*(11), 3280-3281.

(32)   Linstedt, A. D.; Hauri, H. P. Giantin, a novel conserved Golgi membrane protein containing a cytoplasmic domain of at least 350 kDa. *Mol. Biol. Cell* **1993**, *4*, 679-693.

(33)   Hynes, R. O. The emergence of integrins: a personal and historical perspective. *Matrix Biology* **2004**, *23*, 333-340.

(34)   Turner, C. E.; Glenney, J. R., Jr.; Burridge, K. Paxillin: a new vinculin-binding protein present in focal adhesions. *J. Cell Biol.* **1990**, *111*, 1059-1068.

(35)   Zaidel-Bar, R.; Ballestrem, C.; Kam, Z.; Geiger, B. Early molecular events in the assembly of matrix adhesions at the leading edge of migrating cells. *J. Cell Sci.* **2003,** *116*(22), 4605-4613.

CHAPTER 4

TOTAL INTERNAL REFLECTION FLUORESCENCE MICROSCOPY AS A METHOD TO STUDY CELL ADHESION ON PATTERNED GOLD SURFACES

4.1 Introduction

There are a multitude of vital events that occur at the cellular plasma membrane. These events often occur on a very short temporal timescale, and the components involved are often present in low concentrations. Therefore, a method that is both sensitive, preferably at the single molecule level, and able to be time-resolved on the order of milli- to microseconds is needed to study these transient events.[1,2]

While the total internal reflection (TIR) of light was first predicted by Isaac Newton in his 1717 book *Opticks*,[3] total internal reflection fluorescence microscopy (TIRFM) did not become popular as a method to study interfacial processes until the early 1980s. TIRFM is based on the TIR of light and excitation of fluorophores at surfaces. It has been implemented in the study of a variety of processes at biologically relevant interfaces.[4-6] The following sections will describe the physical basis of TIRFM, the application of TIRFM to questions in cell biology, and the experimental question that will be addressed in this chapter.

4.1.1 Physical basis of total internal reflection (TIR). Consider a beam of light traveling in a higher refractive index medium (n_1) that encounters the interface with a lower refractive index medium (n_2). At incidence angles (θ_i) less than the critical

angle (θ_c), the beam of light will be split. The critical angle is a function of the refractive indices of the two adjoining media, and can be described by the equation

$$\theta_c = \sin^{-1}\left(\frac{n_2}{n_1}\right)$$ (4.1)

A fraction of the beam will be reflected back into the higher refractive index medium at an angle θ_r, and the remainder will be transmitted into the lower refractive index medium at an angle θ_t, as shown in Figure 4.1A. The relative proportions can be described by the Fresnel formulations.[7]

If the angle of incidence θ_i is larger than the critical angle θ_c, total internal reflection (TIR) will occur (Figure 4.1A). In essence, the light will be completely reflected back into the higher refractive index medium, with no transmission of light into the lower refractive index medium. An electromagnetic field known as the evanescent wave will be established at the interface.[8] This wave only propagates parallel to the interface, *i.e.* it does not propagate into the lower refractive index medium, and is the same frequency as the incident light.[9] The intensity of the evanescent wave decays exponentially as shown in the equation

$$I(z) = I_o\, e^{\left(\frac{-z}{d}\right)}$$ (4.2)

where I(z) is the intensity of light at a distance z from the interface, I_o is the intensity of light at the interface, and d is the depth of penetration. This distance is typically where I(z) has fallen to 37% of I_o.[10] The depth of penetration of the evanescent wave is a function of the refractive indices of the media involved, as well as the angle of incidence, shown in the equation

$$d = \frac{\lambda_o}{(4\pi n_2)\sqrt{(n_1^2/n_2^2)\sin^2\theta_i - 1}} \qquad (4.3)$$

where λ_o is the wavelength of the incident light in a vacuum, and all other variables are as defined above.[11] Typical penetration depths range from λ_o / 10 to λ_o.[12]

Figure 4.1B illustrates an example of TIRF. In this system the θ_c for the interface between glass (n_1 = 1.51) and water (n_2 = 1.333) is 62º. The incident angle θ_i (70º) of a 512 nm laser beam is greater than θ_c, and thus, TIR occurs. The calculated d for this system is 87 nm. If there are fluorophores close to the interface where the evanescent wave is established, there is a high probability that the fluorophore will be excited, and fluoresce.

4.1.2 Use of total internal reflection fluorescence microscopy (TIRFM) in cell biology. TIRFM has found many applications in the study of biologically relevant surfaces, such as protein adsorption to surfaces,[13,14] as well as substrate-supported planar membranes.[15] Among the earliest reports of TIRFM used to study cell adhesion involved investigating the adhesion of cells with fluorescently labeled plasma membranes on a glass coverslip.[16] TIRFM has also been used to study other aspects of cell-substrate contacts, including examining the space between the plasma membrane and surface,[11,17-19] observations of the proximity of various organelles to the cell surface,[9] the dynamics of integrin receptor clustering,[20] and the affects of ligand affinity on endothelial cell adhesion.[21,22]

One of the most prevalent uses of TIRFM has been to examine the mechanisms of vesicle fusion with the plasma membrane during endo- and exocytosis in a variety
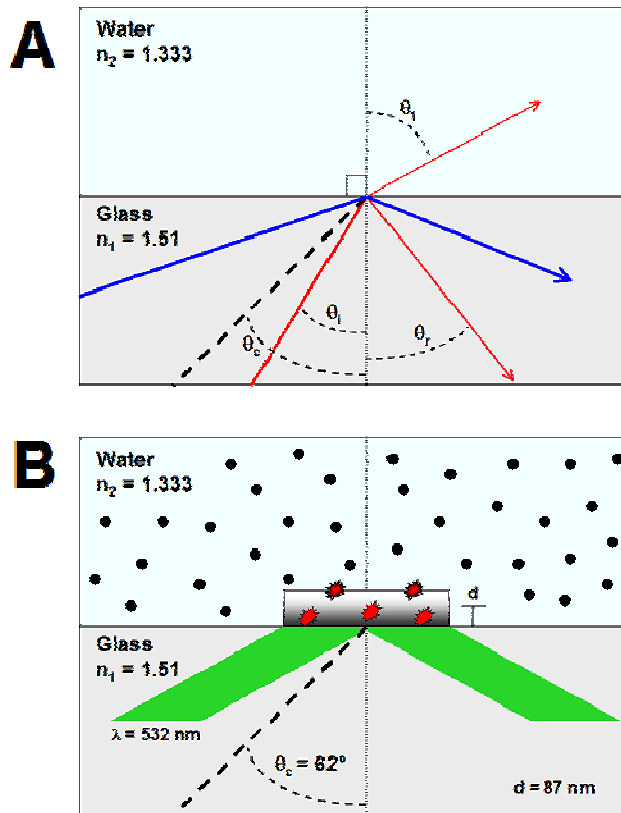
Figure 4.1 The physical basis of total internal reflection fluorescence microscopy (TIRFM). **(A)** At $\theta_i < \theta_c$, an incident beam of light will be split at the interface between two media with dissimilar refractive indices ($n_1 > n_2$, red line). At all $\theta_i \geq \theta_c$, the light beam will achieve total internal reflection (TIR) back into the higher refractive index material (blue line). **(B)** Total internal reflection induced fluorescence. A laser beam ($\lambda = 532$ nm) establishes TIR at $\theta_i > \theta_c$. An evanescent wave is established at the interface (represented by gradient). Fluorophores in the lower refractive index material (black dots) that are within the evanescent field are excited, and can emit observable fluorescence (red stars).

of cell types.[23-30] These reports highlight one of the major advantages of TIRFM over other available visualization techniques. For example, in one- or two-photon confocal fluorescence microscopy the large background fluorescence of out-of-focus fluorophores that is observed due to the larger field of view (~500-800 nm)[31] would obscure the single fusion events at the plasma membrane. However, in TIRFM the range of the evanescent wave is ~3z.[32] Therefore, the optical plane that is viewed is typically ~100-200 nm from the interface. This makes TIRFM an attractive choice for the selective study of events at interfaces.

The short range of the evanescent wave also allows for longer-term studies of living cells, due to the decreased exposure of the whole cell to damaging light, and decreased photobleaching of dyes. Several research groups have exploited this feature by observing living cells for periods up to one week[33,34] and using TIRFM to observe the movement of single fluorescent proteins in living cells.[35,36]

However, given that TIRFM can not produce three dimensional images of a sample, it is often beneficial to use this method in conjunction with other techniques.[37] TIRFM has been successfully used as a complementary technique to alternating-laser excitation (ALEX) spectroscopy,[38] fluorescence correlation spectroscopy (FCS),[39-41] fluorescence recovery after photobleaching (FRAP),[13,42] fluorescence resonance energy transfer (FRET),[43,44] and interference reflection microscopy.[45]

4.1.3 Controversy: can TIRFM be used to study cell adhesion on gold surfaces?
There have been conflicting reports regarding the practicality of TIRFM in the presence of thin metal layers, specifically patterned gold surfaces. Borisy and

80

colleagues have reported that the presence of gold attenuates the fluorescence signal to an unacceptable level, preventing the use of TIRFM to study cell adhesion on gold surfaces.[46] On the other hand, Ariwa and Iwata recently reported the use of TIRFM to study the effects of surface chemistry on cell adhesion by observing the interaction of cells with fluorescently labeled plasma membranes with a variety of SAMs on gold.[47]

The presence of a thin metallic layer at the interface between media with unmatched refractive indices has been shown not to prevent TIRF from occurring.[4] However, there is an effect on the depth of penetration and intensity of the evanescent wave produced near metallic surfaces.[6] The effect of the metallic layer on the excitation and emission of a fluorophore has been found to be very distance-dependent, both by theoretical and experimental studies.[48-51]

The affects of the metal can be roughly divided into three distance regions. When a fluorophore is within the Förster radius distance (typically ~5-7 nm) from the metal surface, the excited fluorophore will undergo a nonradiative transfer of energy to the metal in the form of heat. This is known as 'fluorescence quenching'. On the other extreme, when a fluorophore is relatively far from the surface (typically >20 nm, but no further than the evanescent wave), the result is the emission of observable fluorescence. Fluorophores at intermediate distances (~10 – 15 nm) from the metal layer have shown a coupling of excitation energy with the plasmonic states of the metal, resulting in a complex emission of fluorescence from the metal surface.[52] Some groups have taken advantage of this distance-dependent quenching by using a thin metal film to reduce background fluorescence of non-specifically adsorbed

analytes, while still allowing fluorescence imaging of structures of interest located farther from the surface.[53,54]

The goals for the experiments that will be discussed below were two-fold. The primary goal was to determine if it was possible to observe intracellular structures of interest using TIRFM on patterned gold surfaces. Second, if the methodology proved viable, the next priority would be to verify that TIRFM would be compatible with conventional fluorescence microscopy, a commonly used method to study the nanoarchitecture of adherent cells.

4.2 Experimental Materials and Methods

4.2.1 Preparation of gold-coated quartz substrates. Quartz microscope slides were cleaned with Piranha solution (1:1 (v/v) concentrated H_2SO_4 : 30% H_2O_2). Layers of titanium (6 nm) and gold (24 nm) were thermally evaporated onto the quartz slides using a Thermionics vacuum evaporator system. The gold-coated substrates were stored in ethanol until use.

4.2.2 Substrate patterning by microcontact printing. A PDMS elastomeric stamp with 50 μm features of several shapes (*e.g.* circles, ovals, several polygons, squares, triangles) was produced using soft lithography techniques as previously described.[55] The stamp was inked with hexadecanethiol (C_{16}-SH, 1 mM in ethanol), brought into contact with gold-coated quartz substrates, producing a hydrophobic SAM pattern on the surface. The remaining bare gold region was passivated by immersing the surface in EG_4-C_{11}-SH (1 mM in ethanol) for 12 h. Bovine fibronectin

(Fisher, 0.1 mg/mL in H_2O) was adsorbed to the hydrophobic patterns for 1 h. The surfaces were stored in H_2O until use.

4.2.3 Substrate patterning by DPN. Nanoarrays (20 x 20, 3.0 μm pitch, ~500 nm diameter spots) were patterned as previously described (Chapter 2, Section 2.2.5), followed by immersing the substrate in EG_4-C_{11}-SH (1 mM in ethanol, 12 h). The substrate was then electrochemically oxidized (750 mV vs. Ag/AgCl, 15 s, 1 M $HClO_4$), followed by immobilization of oxyamine-terminated linear RGD peptide (10 mM in H_2O, 2 h).

4.2.4 Cell seeding and staining procedures. 3T3 Swiss Albino mouse fibroblasts were purchased from the Tissue Culture Facility at the University of North Carolina at Chapel Hill. DMEM, bovine calf serum, Dulbecco's PBS, Triton X – 100, DAPI and phalloidin-FITC were purchased from Sigma, and paraformaldehyde solution (32%) was purchased from Fisher. Penicillin/streptomycin were purchased from Gibco. Mouse anti-paxillin antibody was purchased from B D Biosciences (San Jose, CA). Normal goat serum and TRITC-conjugated goat anti-mouse IgG were purchased from Jackson ImmunoResearch Laboratories, Inc. (West Grove, PA).

After the gold-coated quartz substrates were patterned by microcontact printing or DPN, 3T3 Swiss Albino mouse fibroblasts were seeded on the surface in serum-free DMEM for 3 h, followed by incubation in DMEM containing 10% bovine calf serum and 1% penicillin/streptomycin for > 18 h (37 ºC, 5% CO_2 atmosphere). The cells were fixed in 3.2% formaldehyde in PBS, then permeated in PBS containing 0.1% Triton X – 100. All dye mixtures were prepared in 5% normal goat serum in PBS containing 0.1 % Triton X –100.

Substrates that were patterned using microcontact printing were incubated in a humidified chamber with a primary mouse anti-paxillin antibody (1:400 dilution) for 45 min. The surfaces were then rinsed with PBS (3 x 10 min), followed by incubation with TRITC secondary fluorescent antibody (1:400 dilution) for 45 min.

DPN-patterned surfaces were placed in a humidified chamber and stained with a dye mixture (mouse anti-paxillin, 1:400 dilution; phalloidin-FTIC, 1:250 dilution) for 45 min, and then rinsed with PBS (3 x 10 min). The substrates were incubated with a second dye mixture (DAPI, 1:500 dilution; phalloidin-FITC, 1:50 dilution; TRITC secondary fluorescent antibody, 1:400 dilution).

4.2.5 Visualization with TIRFM. Glass cover slips, PBS, and lens paper were purchased from Fisher. Immersion oil (n = 1.4790, type FF) was purchased from Cargille-Sacher Laboratories, Inc. (Cedar Grove, NJ). Quick curing epoxy (Araldite 2043) was purchased from McMaster-Carr (Princeton, NJ). All TIRFM was performed using an Olympus IX51 inverted microscope with an Olympus UPLSAPO 60X (NA 1.2) water immersion objective (Olympus America, Inc., Center Valley, PA). The radiation source was a green diode laser module (GDLM-5030L, Photop Technologies, Chatsworth, CA). A green emission filter (585 nm / 70 nm bandpass, Chroma HQ585/70) was purchased from Chroma Technology (Rockingham, VT) and a CCD camera (Cascade II 512B) was purchased from Photometrics (Tucson, AZ). MatLab R2007b software (The Mathworks, Inc., Natick, MA) was used for image analysis.

Patterned gold-coated quartz substrates were prepared for TIRFM analysis following the staining procedure. A glass cover slip was flamed-dried, allowed to

cool, and placed over the area of patterned cells, trapping a layer of PBS between the glass and quartz. The edges of the cover slip were sealed to retain the PBS medium using 90 second curing epoxy. All TIRFM measurements were made using a prism-based method[56] with an Olympus IX51 inverted microscope and Olympus UPLSAPO 60X water immersion objective. The substrate was placed between a quartz prism and the 60X water immersion objective, using immersion oil and water, respectively, in order to maintain a similar refractive index at each interface. TIR was obtained by adjusting the position of the quartz prism, thus changing the θ_i of the excitation laser beam (λ_{ex} = 532 nm, 30 mW). The emitted radiation of the fluorophores of interest was collected by a 60X water immersion objective, directed through a green emission filter (585 nm / 70 nm bandpass), and finally collected by a CCD camera. Image analysis was performed using MatLab R2007B software.

4.2.6 Visualization with high-resolution fluorescence microscopy. Fluorescence images of DPN patterned substrates were taken following visualization with TIRFM using a Nikon Eclipse TE2000-E inverted microscope (Nikon USA, Inc., Melville, NY). Oil immersion images were obtained using a Plan Fluor 40X oil immersion objective (1.30 NA, Nikon USA). Image analysis was performed using MetaMorph software (Molecular Devices, Downingtown, PA).

4.3 Results and Discussion[57]

4.3.1 Prism-based TIRFM experimental design. A prism-based method of TIRFM was used to examine cells adhered on patterned SAMs on gold-coated quartz surfaces, as shown in Figure 4.2A. A patterned gold-coated quartz slide was

prepared as described above, and placed in contact between a quartz prism and a 60X water immersion objective, using immersion oil and water, respectively, to maintain a similar refractive index between each interface. TIR was established by adjusting the quartz prism, thus changing the θ_i of the incident green diode laser beam (λ = 532 nm).

The interface of interest is shown in more detail in Figure 4.2B. The θ_c for this system was calculated to be ~69.3^o, using equation 4.1 with the refractive index of fused quartz (n_1 = 1.46), and an average refractive index of the cell cytoplasm (n_2 = 1.366). This average refractive index is based on the experimentally determined refractive index range (1.358 – 1.374) of the cytoplasm of 3T3 fibroblasts reported by Lanni, *et al.*[9] The evanescent wave that is created will extend into the cell cytoplasm approximately 120 nm as calculated with equation 4.3 (for θ_i = 75°). The evanescent wave will extend ~80 – 90 nm into the interior of the cell as depicted in Figure 4.2B, taking into account the thickness of the SAM (~2 nm), adsorbed fibronectin layer (~2 nm), cell plasma membrane (~10 nm),[58] and the extracellular domain of integrin receptors (~20 nm).[59] A representative micrograph of a 3T3 Swiss Albino fibroblast grown on bare quartz and stained for the actin cytoskeleton is shown in Figure 4.2C. This demonstrates the visualization of the internal structures of adherent cells by TIRFM in the absence of a thin metal layer.

These estimations, in conjunction with the distance-dependent fluorescence emission of fluorophores near thin metal films that was described in Section 4.1.3, led to the hypothesis that the internal structures of adherent cells on patterned gold
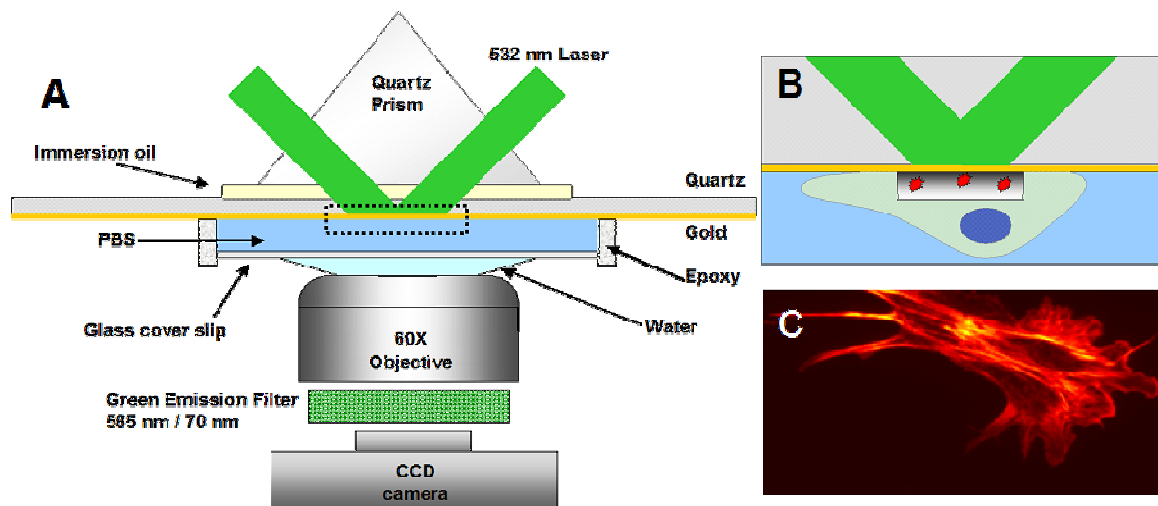
Figure 4.2 Prism-based TIRFM experimental design for cell adhesion studies. **(A)** The patterned gold-coated quartz slide is placed between a quartz prism and a 60X water immersion objective (using immersion oil and water, respectively, to maintain similar refractive indices at each interface). TIR is established by manual adjustment of the quartz prism. TIR induced fluorescence is collected through the objective, sent through a green emission filter, and captured by a CCD camera. The interface of interest is highlighted by the dashed box and is expanded in **(B).** Diagram of the interface of interest (not drawn to scale). The evanescent wave produced by the TIR of the green laser extends into the cytoplasm of adherent cells, enabling the use of fluorescent tags to study internal cellular structures. **(C)** 3T3 Swiss Albino fibroblast grown on bare quartz and stained with phalloidin-TRITC to visualize the actin cytoskeleton (TIRFM signal false colored red).

surfaces could be observed with TIRFM. In the studies discussed below, focal adhesions, the structures of interest, should be within the range of the evanescent wave, allowing for the excitation of fluorescent labels. Also, the fluorophores should be distant enough from the gold surface so that the excitation energy will not be transferred back to the metal film, quenching the fluorescence signal. In order to test this hypothesis, an experiment using microcontact printing to pattern SAMs on gold was conducted.

4.3.2 TIRFM visualization of cell adhesion on microcontact printed patterns. SAMs of C_{16}-SH on gold-coated quartz slides were patterned using microcontact printing, as shown in Figure 4.3A. An elastomeric PDMS stamp with 50 μm features of various shapes (*e.g.* circles, ovals, several polygons, squares, triangles) was inked with a solution of C_{16}-SH and brought into contact with a clean gold surface. Hydrophobic SAMs were formed in the pattern of the stamp, and the remaining non-patterned gold surface was rendered inert to nonspecific cell adhesion by backfilling with EG_4-C_{11}-SH. The ECM protein fibronectin was then adsorbed to the hydrophobic patterns in order to support cell adhesion. 3T3 Swiss Albino mouse fibroblasts were seeded to the surface, fixed, and stained with an antibody targeting paxillin, a protein found in focal adhesions,[60] followed by a TRITC secondary antibody. Several representative micrographs of various shapes are shown in Figure 4.3B (clockwise from top left: circle, square, hexagon, oval). The TIRFM signal (false colored red) demonstrates that paxillin, representing the distribution of focal adhesions, is dispersed throughout the cells. These results indicated that TIRFM is a viable method to examine the internal structures of adherent cells in the presence of
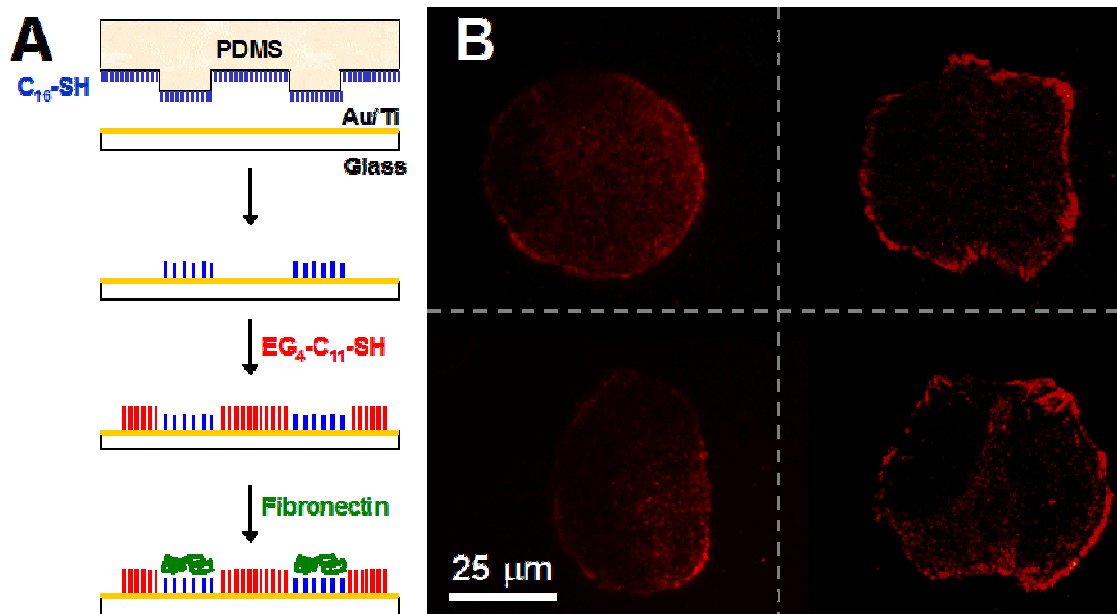
Figure 4.3 TIRFM visualization of cell adhesion on microcontact printed patterns. **(A)** Microcontact printing technique. An elastomeric stamp is inked with C_{16}-SH and placed in contact with a gold surface, producing a patterned SAM. The remaining gold areas are backfilled with EG_4-C_{11}-SH, the ECM protein fibronectin is adsorbed, and fibroblasts are seeded. **(B)** Representative micrographs of 3T3 Swiss Albino fibroblasts adhered to 50 μm microcontact printed patterns of adsorbed fibronectin. Clockwise, from top left: circle, square, hexagon, and oval. The cells were stained with anti-paxillin and a TRITC secondary antibody to visualize the focal adhesions (TIRFM signal is false colored red). Paxillin is shown to be distributed throughout the cells.

a thin metal layer. Next, DPN patterned surfaces were produced in order to demonstrate the use of TIRFM to study biospecific ligand mediated cell adhesion, as well as to investigate the use of TIRFM in combination with high-resolution fluorescence microscopy.

4.3.3 TIRFM and high-resolution fluorescence microscopy of adherent fibroblasts on symmetric nanoarrays presenting biospecific ligands. Symmetric nanoarrays were produced *via* DPN on gold-coated quartz slides as previously described (Chapter 2, Section 2.2.5). Following electrochemical oxidation of the hydroquinone-presenting nanoarray to the corresponding quinone, oxyamine-terminated linear RGD peptide was immobilized (10 mM in H_2O, 2 h). 3T3 Swiss Albino mouse fibroblasts were then seeded to the substrates, fixed, and stained for nuclei, the actin cytoskeleton, and paxillin.

As shown in Figure 4.4A, the TIRFM signal from paxillin is localized primarily to the periphery of the cell. This corroborates well with the results previously discussed (Chapter 2, Section 2.3.4). The same substrates were then visualized with conventional fluorescence microscopy. A representative micrograph of one such cell is shown in Figure 4.4B. Interestingly, there is not a significant amount of photobleaching of the TRITC secondary antibody following extended imaging using TIRFM. This is to be expected, to some extent, based on the theoretical descriptions of the behavior of excited fluorophores near thin metal layers. Essentially, the efficient energy transfer and quenching mechanism of the metal layer will protect a fluorescent molecule by shortening the excitation lifetime of the molecule. This will
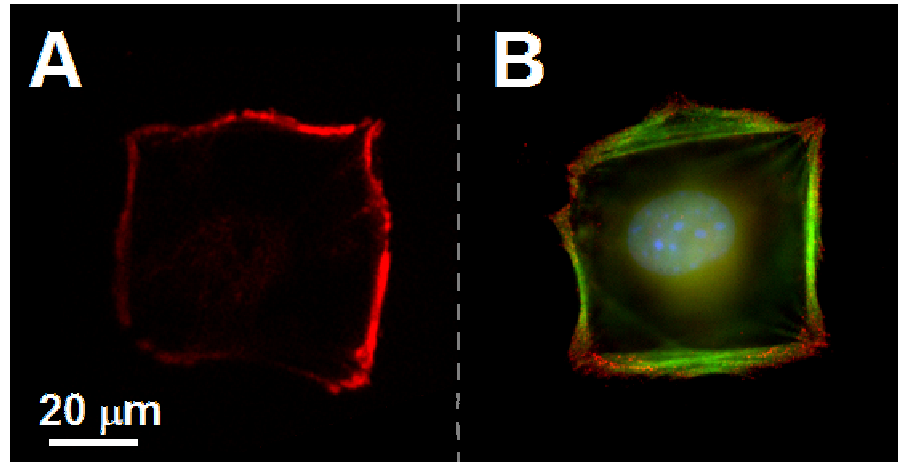
Figure 4.4 (A) Representative TIRFM micrograph of an adherent fibroblast on a symmetric nanoarray presenting immobilized linear RGD ligand. The cell was stained with anti-paxillin with a TRITC secondary fluorescent antibody, DAPI, and phalloidin-FITC. TIRFM signal (false colored red) demonstrates that paxillin is localized primarily to the periphery of the cell. **(B)** Representative fluorescence micrograph of adherent fibroblast on a symmetric nanoarray following TIRFM imaging. The cell was stained with anti-paxillin with a TRITC secondary antibody (focal adhesions, red), DAPI (nuclei, blue), and phalloidin-FITC (actin cytoskeleton, green). The TRITC signal corresponding to paxillin is still visible, suggesting that the fluorescent label has not been photobleached by prolonged viewing with TIRFM.

increase the number of excitation cycles the molecule can undergo before photodamage occurs.[61]

4.4 Conclusions

It was determined that TIRFM is an effective method to visualize the internal structures of cells adhered to patterned SAMs on gold surfaces. This was demonstrated through the use of microcontact printing to produce patterns of nonspecifically adsorbed protein, as well as electroactive nanoarrays presenting biospecific ligands. Secondly, TIRFM imaging can be used in conjunction with more traditional methods of imaging, such as fluorescence microscopy to study cellular nanoarchitecture. The intensity of the signal collected for the fluorophores studied in these cells is decreased compared to those in cells imaged in the absence of a gold layer (see Figure 4.2C). However, it was shown that this technique still yields a sufficient signal to study cell adhesion on patterned gold surfaces, thus TIRFM imaging for cell biology studies is not prohibited in the presence of a thin metal layer, as was previously reported.[46] In the future, TIRFM could be used to explore the intricacies of the cell nanoarchitecture on engineered surfaces presenting various patterns of biospecific ligands. More details descriptions of the potential future directions of this technique will be presented in more detail in Chapter 5.

REFERENCES

(1)   Lippincott-Schwartz, J.; Patterson, G. H. Development and use of fluorescent protein markers in living cells. *Science* **2003**, *300,* 87-91.

(2)   Conner, S. D.; Schmid, S. L. Regulated portals of entry into the cell. *Nature* **2003**, *422,* 37-44.

(3)   Harrick, N. J. *Internal reflection spectroscopy.* Interscience Publishers: New York, 1967; pp 327.

(4)   Axelrod, D.; Burghardt, T. P.; Thompson, N. L. Total internal reflection fluorescence. *Annu. Rev. Biophys. Bioeng.* **1984**, *13,* 247-268.

(5)   Axelrod, D. Total internal reflection fluorescence microscopy in cell biology. *Traffic* **2001**, 2, 764-774.

(6)   Axelrod, D. Total internal reflection fluorescence microscopy in cell biology. In *Methods in enzymology;* Marriott, G.; Parker, I., Eds.; Academic Press: 2003; Vol. 361, pp 1-33.

(7)   Gell, C.; Brockwell, D.; Smith, A. *Handbook of single molecule fluorescence spectroscopy.* Oxford University Press Inc.: New York, 2006; pp 262.

(8)   Thompson, N. L.; Pero, J. K. Total internal reflection fluorescence microscopy: applications in biophysics. In *Fluorescence spectroscopy in biology. Advanced methods and their applications to membranes, proteins, DNA, and cells.* Hof, M., Hutterer, R. and Fidler, V., Eds.; Springer-Verlag: Berlin, Germany, 2005; Vol. 3, pp 79-103.

(9)   Lanni, F.; Waggoner, A.; Taylor, D. Structural organization of interphase 3T3 fibroblasts studied by total internal reflection fluorescence microscopy. *J. Cell Biol.* **1985**, *100,* 1091-1102.

(10)   Steyer, J. A.; Almers, W. A real-time view of life within 100 nm of the plasma membrane. *Nat. Rev. Mol. Cell Biol.* **2001**, *2,* 268-276.

(11)   Weis, R.; Balakrishnan, K.; Smith, B.; McConnell, H. Stimulation of fluorescence in a small contact region between rat basophil leukemia cells and planar lipid membrane targets by coherent evanescent radiation. *J. Biol. Chem.* **1982**, *257,* 6440-6445.

(12)   Krishnan, R. V.; Varma, R.; Mayor, S. Fluorescence methods to probe nanometer-scale organization of molecules in living cell membranes. *J. Fluoresc.* **2001**, *11,* 211-226.

(13)   Burghardt, T. P.; Axelrod, D. Total internal reflection / fluorescence photobleaching recovery study of serum albumin adsorption dynamics. *Biophys. J.* **1981**, *33,* 455-468.

(14)   Thompson, N. L.; Axelrod, D. Immunoglobulin surface-binding kinetics studies by total internal reflection with fluorescence correlation spectroscopy. *Biophys. J.* **1983**, *43,* 103-114.

(15)   Thompson, N. L.; Pearce, K. H.; Hseih, H. V. Total internal reflection fluorescence microscopy: application to substrate-supported planar membranes. *Eur. Biophys. J.* **1993**, *22,* 367-378.

(16)   Axelrod, D. Cell-substrate contacts illuminated by total internal reflection fluorescence. *J. Cell Biol.* **1981**, *89,* 141-145.

(17)   Gingell, D.; Todd, I.; Bailey, J. Topography of cell-glass apposition revealed by total internal reflection fluorescence of volume markers. *J. Cell Biol.* **1985**, *100,* 1334-1338.

(18)   Geggier, P.; Fuhr, G. A time-resolved total internal reflection aqueous fluorescence (TIRAF) microscope for the investigation of cell adhesion dynamics. *Appl. Phys. A: Mater. Sci. Proc.* **1999**, *68,* 505-513.

(19)   Burmeister, J. S.; Olivier, L. A.; Reichert, W. M.; Truskey, G. A. Application of total internal reflection fluorescence microscopy to study cell adhesion to biomaterials. *Biomaterials* **1998**, *19,* 307-325.

(20)   Kawakami, K.; Tatsumi, H.; Sokabe, M. Dynamics of integrin clustering at focal contacts of endothelial cells studied by multimode imaging microscopy. *J. Cell. Sci.* **2001**, *114,* 3125-3135.

(21)   Chan, B. P.; Bhat, V. D.; Yegnasubramanian, S.; Reichert, W. M.; Truskey, G. A. An equilibrium model of endothelial cell adhesion via integrin-dependent and integrin-independent ligands. *Biomaterials* **1999**, *20,* 2395-2403.

(22)   Olivier, L. A.; Yen, J.; Reichert, W. M.; Truskey, G. A. Short-term cell/substrate contact dynamics of subconfluent endothelial cells following exposure to laminar flow. *Biotechnol. Progr.* **1999**, *15,* 33-42.

(23)   Schmoranzer, J.; Goulian, M.; Axelrod, D.; Simon, A. S. Imaging constitutive exocytosis with total internal reflection fluoresence microscopy. *J. Cell Biol.* **2000**, *149,* 23-31.

(24) Jaiswal, J. K.; Andrews, N. W.; Simon, S. M. Membrane proximal lysosomes are the major vesicles responsible for calcium-dependent exocytosis in nonsecretory cells. *J. Cell Biol.* **2002**, *159,* 625-635.

(25) Toomre, D.; Steyer, J. A.; Keller, P.; Almers, W.; Simons, K. Fusion of constitutive membrane traffic with the cell surface observed by evanescent wave microscopy. *J. Cell Biol.* **2000**, *149,* 33-40.

(26) Ohara-Imaizumi, M.; Fujiwara, T.; Nakamichi, Y.; Okamura, T.; Akimoto, Y.; Kawai, J.; Matsushima, S.; Kawakami, H.; Watanabe, T.; Akagawa, K.; Nagamatsu, S. Imaging analysis reveals mechanistic differences between first- and second-phase insulin exocytosis. *J. Cell Biol.* **2007**, *177,* 695-705.

(27) Zhang, Z.; Chen, G.; Zhou, W.; Song, A.; Zu, T.; Luo, Q.; Wang, W.; Gu, X. S.; Duan, S. Regulated ATP release from astrocytes through lysosome exocytosis. *Nat. Cell Biol.* **2007**, *9,* 945-957.

(28) Merrifield, C. J.; Feldman, M. E.; Wan, L.; Almers, W. Imaging actin and dynamin recruitment during invagination of single clathrin-coated pits. *Nat. Cell Biol.* **2002**, *4,* 691-699.

(29) Zenisek, D.; Steyer, J. A.; Feldman, M. E.; Almers, W. A membrane marker leaves synaptic vesicles in milliseconds after exocytosis in retinal bipolar cells. *Neuron* **2002**, *35,* 1085-1097.

(30) Oheim, M.; Stuhmer, W. Tracking chromaffin granules on their way through the actin cortex. *Eur. Biophys. J.* **2000**, *29,* 67-89.

(31) Toomre, D.; Manstein, D. J. Lighting up the cell surface with evanescent wave microscopy. *Trends Cell Biol.* **2001**, *11,* 298-303.

(32) Gingell, D. Advances towards the measurement of cell contacts with surfaces at near nanometer vertical resolution by means of total internal reflection fluorescence. In *Studying cell adhesion.* Bongrand, P.; Claesson, P. M.; Curtis, A. S. G., Eds.; Springer-Verlag: Berlin, Germany, 1994; pp 195-218.

(33) Wang, M. D.; Axelrod, D. Time-lapse total internal reflection fluorescence video of acetylcholine receptor cluster formation on myotubes. *Dev. Dynam.* **1994**, *201,* 29-40.

(34) Manneville, J. B. Use of TIRF microscopy to visualize actin and microtubules in migrating cell.s. *Methods Enzymol.* **2006**, *406,* 520-532.

(35) Mashanov, G. I.; Tacon, D.; Knight, A. E.; Peckham, M.; Molloy, J. E. Visualizing single molecules inside living cells using total internal reflection fluorescence microscopy. *Methods* **2003**, *29,* 142-152.

(36)   He, R.-Y.; Chang, G.-L.; Wu, H.-L.; Lin, C.-H.; Chiu, K.-C.; Su, Y.-D.; Chen, S.-J. Enhanced live cell membrane imaging with surface plasmon-enhanced total internal reflection fluorescence microscopy. *Opt. Express* **2006**, *14,* 9307-9316.

(37)   Holt, M. R.; Soong, D. Y. H.; Monypenny, J.; Dobbie, I. M.; Zicha, D.; Dunn, G. A. Using bioprobes to follow protein dynamics in living cells. In *Cell motility, from molecules to organisms.* Ridley, A., Peckham, M., Clark, P., Eds.; John Wiley & Sons, Inc.: West Sussex, England, 2004; pp 117-134.

(38)   Santoso, Y.; Hwang, L. C.; Le Reste, L.; Kapanidis, A. N. Red light, green light: probing single molecules using alternating-laser excitation. *Biochem. Soc. Trans.* **2008**, *36,* 738-744.

(39)   Hansen, R. L.; Harris, J. M. Measuring reversible adsorption kinetics of small molecules at solid/liquid interfaces by total internal reflection fluorescence correlation spectroscopy. *Anal. Chem.* **1998**, *70,* 4247-4256.

(40)   Hansen, R. L.; Harris, J. M. Total internal reflection fluorescence correlation spectroscopy for counting molecules at solid/liquid interfaces. *Anal. Chem.* **1998**, *70,* 2565-2575.

(41)   Thompson, N. L.; Steele, B. L. Total internal reflection with fluorescence correlation spectroscopy. *Nat. Protoc.* **2007**, *2,* 878-890.

(42)   Lenn, T.; Leake, M. C.; Mullineaux, C. W. Clustering and dynamics of cytochrome bd-I complexes in the Escherichia coli plasma membrane in vivo. *Mol. Microbiol.* **2008**, *70,* 1397-1407.

(43)   Watts, T. H.; Gaub, H. E.; McConnell, H. M. T-cell-mediated association of peptide antigen and major histocompatibility complex protein detected by energy transfer in an evanescent wave-field. *Nature* **1986**, *320,* 179-181.

(44)   Bal, M.; Zaika, O.; Martin, P.; Shapiro, M. S. Calmodulin binding to M-type K^+ channels assayed by TIRF/FRET in living cells. *J. Physiol. (Lond.)* **2008**, *586,* 2307-2320.

(45)   Llobet, A.; Beaumont, V.; Lagnado, L. Real-time measurement of exocytosis and endocytosis using interference of light. *Neuron* **2003**, *40,* 1075-1086.

(46)   Kandere-Grzybowska, K.; Campbell, C.; Komarova, Y.; Grzybowski, B. A.; Borisy, G. G. Molecular dynamics imaging in micropatterned living cells. *Nat. Methods* **2005**, *2,* 739-741.

(47)   Ariwa, Y.; Iwata, H. Effects of surface functional groups on protein adsorption and subsequent cell adhesion using self-assembled monolayers. *J. Mater. Chem.* **2007**, *17,* 4079-4087.

(48)   Weber, W. H.; Eagen, C. F. Energy transfer from an excited dye molecule to the surface plasmons of an adjacent metal. *Opt. Lett.* **1979**, *4,* 236-238.

(49)   Ford, G. W.; Weber, W. H. Electromagnetic interactions of molecules with metal surfaces. *Physics Reports* **1984**, *113,* 195-287.

(50)   Enderlein, J. A theoretical investigation of single-molecule fluorescence detection in thin metallic layers. *Biophys. J.* **2000**, *78,* 2151-2158.

(51)   Mattheyses, A. L.; Axelrod, D. Fluorescence emission patterns near glass and metal-coated surfaces investigated with back focal plane imaging. *J. Biomed. Opt.* **2005**, *10,* 054007-1 – 054007-6.

(52)   Liebermann, T.; Knoll, W. Surface-plasmon field-enhanced fluorescence spectroscopy. *Colloids and Surfaces A: Physicochemical and Engineering Aspects* **2000**, *171,* 115-130.

(53)   Fulbright, R. M.; Axelrod, D. Dynamics of nonspecific adsorption of insulin to erythrocyte membranes. *J. Fluoresc.* **1993**, *3,* 1-16.

(54)   Burghardt, T. P.; Charlesworth, J. E.; Halstead, M. F.; Tarara, J. E.; Ajtai, K. In situ fluorescence protein imaging with metal film-enhanced total internal reflection microscopy. *Biophys. J.* **2006**, *90,* 4662-4671.

(55)   Deng, T.; Tien, J.; Xu, B.; Whitesides, G. M. Using patterns in microfiche as photomasks in 10-μm-scale microfabrication. *Langmuir* **1999,** *15*(19), 6575-6581.

(56)   Truskey, G. A.; Burmeister, J. S.; Grapa, E.; Reichert, W. M. Total internal reflection fluorescence microscopy (TIRFM). II. Topographical mapping of relative cell/substratum separation distances. *J. Cell Sci.* **1992**, *103,* 491-499.

(57)   Hoover, D. K.; Lee, E.-J.; Yousaf, M. N. Total internal reflection fluorescence microscopy of cell adhesion on patterned self-assembled monolayers on gold. *Langmuir* **2009**, *25*(5), 2563-2566.

(58)   Hine, R., Ed. The facts on file dictionary of cell and molecular biology. Facts on File: New York, 2003; pp 248.

(59)   Nermut, M. V.; Green, N. M.; Eason, P.; Yamada, S. S.; Yamada, K. M. Electron microscopy and structural model of human fibronectin receptor. *EMBO J.* **1988,** *7*(13), 4093-4099.

(60)   Turner, C.E.; Glenney, J.R.; Burridge, K. *J. Cell Biol.* **1990,** *111,* 1059-1068.

(61)   Enderlein, J. Single-molecule fluorescence near a metal layer. *Chem. Phys.* **1999,** *247*(1), 1-9.

CHAPTER 5

SUMMARY AND FUTURE DIRECTIONS OF RESEARCH

5.1 Summary of Dissertation Research

Cell adhesion, polarization, and migration are vital to numerous biological phenomena. As such, a greater understanding of the mechanisms of these essential processes will have broad impacts in fields as diverse as developmental biology to medicine. This work has focused on developing a nanoscale model system, based on surface chemistry, which will allow for the study of the spatial presentation of immobilized ligands and their effect on the nanoarchitecture of adherent cells.

In Chapter 2, the development of electroactive nanoarrays of hydroquinone-terminated alkanethiol, produced by dip-pen nanolithography (DPN) is described.[1] These nanoarrays, in conjunction with an oxime-chemistry based chemoselective immobilization strategy and high-resolution fluorescence microscopy, were used to study biospecific-ligand mediated single cell adhesion. The difference in ligand affinity of two cell adhesive peptides (linear and cyclic RGD) was shown to have a dramatic affect on the organization of intracellular nanoarchitecture in adherent fibroblasts.

The production of asymmetric nanoarrays used to study single cell polarization is discussed in Chapter 3.[2] Asymmetric nanoarrays presenting linear RGD peptide were found to induce net directional cell polarization in adherent fibroblasts, while symmetric nanoarrays presenting the same ligand did not induce net polarity. This

demonstrates a direct correlation between the spatial distribution of cell adhesive ligand and the establishment and maintenance of directional cell polarization. It was also shown that there was no net directional cell polarity found on asymmetric nanoarrays presenting a higher affinity ligand cyclic RGD peptide. This indicates that ligand affinity also has a profound effect on cell polarization. The relationship between ligand affinity and spatial distribution of immobilized ligand was further explored through the development of double asymmetric nanoarrays presenting cyclic RGD, which were shown to impose net directional cell polarization.

In order to extend this methodology to examine other aspects of cell adhesion and polarization on electroactive nanoarrays other methods of visualization were considered. There have been conflicting reports regarding the use of total internal reflection fluorescence microscopy (TIRFM) to visualize cells near thin metal layers. In Chapter 4, TIRFM was used to examine the internal structures of cells adhered to patterned SAMs on gold surfaces, using both microcontact printing and DPN SAM patterning methods.[3] The intensity of the signal collected for the fluorophores studied in these cells is decreased compared to those in cells imaged in the absence of a gold layer. However, it was shown that this technique still yields sufficient signal to study cell adhesion on patterned gold surfaces. Thus, TIRFM imaging for cell biology studies is not precluded in the presence of a thin metal layer, as was previously reported.

5.2 Future Directions of Dissertation Research

The research described in this dissertation would best be applied in conjunction with improvements of DPN patterning throughput afforded by several

technological advances described below. One of the major limitations of DPN methodology is serial patterning of consecutive features with a single tip. The development and commercialization of massively parallel AFM cantilever arrays capable of patterning many features concurrently will first be described, followed by the discussion of possible future applications.

5.2.1 Introduction: development of parallel AFM cantilever arrays. From the first report of DPN by Mirkin *et al.* in 1999,[4] the typical DPN experiment has consisted of a single AFM tip patterning in a serial manner. It soon became apparent that in order to fully capitalize on the potential of DPN in a variety of applications, the previous serial patterning method would have to be replaced by a parallel system. An ideal parallel technique would be capable of vastly improving the throughput of DPN. Increasing the effective area that can be patterned by a single DPN probe, which is typically constrained by the scanning window of the AFM model used, would also improve the throughput of DPN.[5,6] For example, the scanning area of the MFP-3D Stand Alone AFM from Asylum Research is 90 μm x 90 μm (0.0081 mm^2).

Parallel arrays of AFM cantilevers have been previously investigated for parallel imaging applications, as well as the development of new data storage media. Quate *et al.* reported the production of AFM images with horizontal distances of 2 mm and 6.4 mm, with 10 x 1 and 32 x 1 linear arrays of cantilevers, respectively.[7] The authors also demonstrated the use of a 50 x 1 linear cantilever array to pattern a 1 cm^2 area through oxidative lithography.[7] The following year a 5 x 5 two-dimensional array of AFM cantilevers capable of patterning a 5 mm x 5 mm area was reported.[8]

These two examples show a vast improvement over the typical scanning area that can be imaged by a single AFM tip.

In another application of massively parallel AFM cantilever arrays, researchers at the IBM Zurich Research Laboratory have been developing a concept known as "the millipede." The millipede is a 32 x 32 two dimensional array of AFM cantilevers that operates by thermomechanical means to write and read bits of data embedded in a thin polymer substrate.[9] The theoretical density of data storage using this method, 0.5 – 1 Terabits / inch^2, is far beyond what is possible with magnetic disc drives now available (<100 Gigabits / inch^2).[10] In order to make full use of such a data storage system, each cantilever must be individually addressable, requiring sophisticated electronics and microfabrication methods.

5.2.2 Introduction: development of massively parallel DPN. Mirkin *et al.* first demonstrated that up to eight commercially available AFM cantilevers could be used in tandem as an array for both parallel, single ink DPN experiments, as well as serial, multiple ink experiments.[11] This report also remarked on the relative independence of DPN-generated feature size on contact force applied at the AFM tip.[11] This important finding reduces one of the major obstacles in the development of parallel DPN experiments; namely, the perceived requirement that each tip must be engaged with the surface identically. The first example of arrays of cantilevers specifically designed for DPN experiments included a 32 x 1 linear array of silicon nitride cantilevers.[12] There have been several subsequent examples of design optimization of cantilever arrays,[13] the generation of multilayer organic thin films by

parallel DPN,[14] the use of parallel DPN to immobilize proteins,[15,16] virus particles,[17] and to pattern silicon nanostructures.[18]

There are several manufacturing aspects that are crucial in the development of massively parallel cantilever arrays, including the design and microfabrication of the cantilevers, as well as the integration of the feedback system for cantilever deflection.[19] This has led to the simultaneous development of two main types of parallel cantilever arrays for DPN, passive cantilever arrays and individually addressable cantilever arrays. In passive arrays, only one cantilever is used for feedback, typically through the optical lever deflection system found in conventional AFM arrangements. Using one cantilever simplifies the electronics required for the cantilever array, allowing for the design and production of very large arrays of cantilevers for DPN.[19] One notable example of this is an array consisting of 55,000 passive cantilevers, arranged with a pitch of 90 μm x 20 μm (x and y, respectively), covering a total area of 1 cm^2. This array was able to replicate 88,000,000 dot features in less than 30 min by printing 40 x 40 dot arrays at each of the 55,000 tips simultaneously.[20] However, in order to produce more intricate patterns or to concurrently pattern motifs with multiple inks, each cantilever must be controlled individually. This calls for more sophisticated cantilever design involving integrated wiring produced during microfabrication, deflection detection systems, and external electronics to process the large amounts of data collected.[21-23] For example, a multifunctional cantilever array including five DPN cantilevers, nine scanning probe contact printing cantilevers, and three imaging cantilevers was designed, with each cantilever capable of being actuated independently of the others.[22]

5.2.3 Whole-substrate nanopatterns for cell migration studies. A linear passive cantilever array could be implemented for the rapid patterning of a relatively large surface area, on the order of several square millimeters to square centimeters. This vast improvement in throughput, combined with the sub-100 nm resolution provided by DPN, would be a great advantage in producing a wide range of feature sizes and spatial distribution in a relatively short amount of time. A variety of oxyamine-terminated cell adhesive ligands could be immobilized to such nanopatterned surfaces through the chemoselective immobilization strategy based on hydroquinone-terminated SAMs, as previously described.

Morphological studies of cell behavior could then be undertaken by observing cell migration on the nanopatterned, biospecific-ligand presenting surface through brightfield microscopy. Alternatively, cells could be allowed to migrate, given specific cues such as the spatial presentation and binding affinity of the biospecifc ligands presented, and then fixed and stained to study internal cellular nanoarchitecture. Another application of these surfaces would be live-cell migration studies conducted using transfected cell lines expressing fluorescently labeled cellular organelles of interest.[24] This would allow for real-time studies of the reorganization of cellular nanoarchitecture during migration on nanopatterns presenting biospecific ligands of interest.

5.2.4 Arrays of nanoarrays: towards single cell assays for drug discovery and mechanistic studies of cell adhesion and polarization. Another application for the use of passive parallel DPN cantilever arrays would be to pattern arrays of nanoarrays over an entire surface. In this study, nanoarrays similar in size to those described in

Chapters 2 and 3 (symmetric and asymmetric nanoarrays, respectively) could be replicated for high throughput, single cell adhesion and polarization studies. The large numbers of nanoarrays capable of confining single cells could subsequently be used as a type of single cell based assay. These assays could then be implemented in the screening of drug candidates, in addition to more complete mechanistic studies of the fundamental aspects of cell adhesion and polarization. This methodology could be particularly powerful in the area of developing more targeted and effective therapies for various cancers.[25-27] Furthermore, such single cell based assays could be used in conjunction with the tissue, protein, and nucleic acid based microarrays currently utilized to study disease and identify drug targets in medical fields as diverse as oncology (*e.g.* breast, lung, ovarian, and colon cancers), infectious disease (*e.g.* methicillin resistant *Staphylococcus aureus* (MRSA), tuberculosis), and neurological disorders (*e.g.* depression, schizophrenia, Parkinson's).[28-30]

5.2.5 Complex nanopatterns presenting multiple, biospecific ligands for cell biology studies. Arrays of individually addressable cantilevers will enable the production of more complex nanopatterns. For example, DPN patterning could be combined with microfluidic lithography, a SAM patterning technique based on the delivery of alkanethiol solution to spatially defined areas through the application of a microfluidic cassette.[31,32] The combination of a nanopatterned surface presenting one biospecific ligand with an overlaid gradient of a second ligand would be of particular interest. This could be possible with the use of a microfluidic lithography generated gradients.[33] The combination of DPN with other SAM patterning

techniques allow for the production of surfaces that are functionalized with two or more biospecific ligands in order to parse apart the complex mechanisms of cell adhesion, polarization, and migration. The application of both technologies would enable the spatial and temporal control of ligand presentation to more closely mimic the complex microenvironments of cells *in vivo*.

5.3 Conclusions

The results presented herein have demonstrated that DPN-generated electroactive nanoarrays, in conjunction with a chemoselective immobilization strategy and microscopy techniques, were shown to be a versatile method for examining various facets of biospecific-ligand mediated cell adhesion and polarization. Specifically, it was determined that the spatial distribution, as well as ligand affinity for two cell adhesive ligands (linear and cyclic RGD) had dramatically different effects on the cellular nanoarchitecture of adherent fibroblasts, as observed through the fluorescent labeling of focal adhesion proteins and the Golgi apparatus. The potential future applications of this work rely heavily on the commercialization of massively parallel DPN cantilever arrays. Thus far, such parallel arrays are only currently available from one source, and are only for use with for a specific DPN instrument.[34] In the future, as such technology is more widely disseminated, the research described here will have a broader impact in diverse fields, including medical and basic biological research.

REFERENCES

(1)   Hoover, D. K.; Lee, E.-J.; Chan, E. W. L.; Yousaf, M. N. Electroactive nanoarrays for biospecific ligand mediated studies of cell adhesion. *ChemBioChem* **2007**, *8,* 1920-1923.

(2)   Hoover, D. K.; Chan, E. W. L.; Yousaf, M. N. Asymmetric peptide nanoarray surfaces for studies of single cell polarization. *J. Am. Chem. Soc.* **2008**, *130,* 3280-3281.

(3)   Hoover, D. K.; Lee, E.-J.; Yousaf, M. N. Total internal reflection fluorescence microscopy of cell adhesion on patterned self-assembled monolayers on gold. *Langmuir* **2009**, *25,* 2563-2566.

(4)   Piner, R. D.; Zhu, J.; Xu, F.; Hong, S. H.; Mirkin, C. A. "Dip-pen" nanolithography. *Science* **1999**, *283,* 661-663.

(5)   Ginger, D. S.; Zhang, H.; Mirkin, C. A. The evolution of dip-pen nanolithography. *Angew. Chem. -Int. Edit.* **2004**, *43,* 30-45.

(6)   Wouters, D.; Schubert, U. S. Nanolithography and nanochemistry: probe-related patterning techniques and chemical modification for nanometer-sized devices. *Angew. Chem. -Int. Edit.* **2004**, *43,* 2480-2495.

(7)   Minne, S. C.; Adams, J. D.; Yaralioglu, G.; Manalis, S. R.; Atalar, A.; Quate, C. F. Centimeter scale atomic force microscope imaging and lithography. *Appl. Phys. Lett.* **1998**, *73,* 1742-1744.

(8)   Lutwyche, M.; Andreoli, C.; Binnig, G.; Brugger, J.; Drechsler, U.; Häberl, W.; Rohrer, H.; Rothuizen, H.; Vettiger, P.; Yaralioglu, G.; Quate, C. F. 5 X 5 2D AFM cantilever arrays a first step towards a Terabit storage device. *Sensors and Actuators* **1999**, *73,* 89-94.

(9)   Vettiger, P.; Despont, M.; Drechsler, U.; Dürig, U.; Häberle, W.; Lutwyche, M. I.; Rothuizen, H. E.; Stutz, R.; Widmer, R.; Binning, G. K. The "Millipede" - more than one thousand tips for future AFM data storage. *IBM J. Res. Develop.* **2000**, *44,* 323-340.

(10)   Vettiger, P.; Cross, G.; Despont, M.; Drechsler, U.; Dürig, U.; Gotsmann, B.; Häberle, W.; Lantz, M. A.; Rothuizen, H. E.; Stutz, R.; Binning, G. K. The "Millipede" - nanotechnology entering data storage. *IEEE Trans. Nanotechnol.* **2002**, *1,* 39-55.

(11)   Hong, S.; Mirkin, C. A. A nanoplotter with both parallel and serial writing capabilities. *Science* **2000**, *288,* 1808-1811.

(12) Zhang, M.; Bullen, D.; Chung, S.-W.; Hong, S.; Ryu, K. S.; Fan, Z.; Mirkin, C. A.; Liu, C. A MEMS nanoplotter with high-density parallel dip-pen nanolithography probe arrays. *Nanotechnol.* **2002**, *13,* 212-217.

(13) Zou, J.; Bullen, D.; Wang, X.; Liu, C.; Mirkin, C. A. Conductivity-based contact sensing for probe arrays in dip-pen nanolithography. *Appl. Phys. Lett.* **2003**, *83,* 581-583.

(14) Lee, S. W.; Sanedrin, R. G.; Oh, B.-K.; Mirkin, C. A. Nanostructured polyelectrolyte multilayer organic thin films generated via parallel dip-pen nanolithography. *Adv. Mater.* **2005**, *17,* 2749-2753.

(15) Lee, S. W.; Oh, B.-K.; Sanedrin, R. G.; Salaita, K.; Fujigaya, T.; Mirkin, C. A. Biologically active protein nanoarrays generated using parallel dip-pen nanolithography. *Adv Mater* **2006**, *18,* 1133-1136.

(16) Martínez-Otero, A.; Hernando, J.; Ruiz-Molina, D.; Maspoch, D. pH-Responsive fluorescent nanoarrays fabricated by direct-write parallel dip-pen nanolithography. *Small* **2008**, *4,* 2131-2135.

(17) Vega, R. A.; Maspoch, D.; Salaita, K.; Mirkin, C. A. Nanoarrays of single virus particles. *Angew. Chem. -Int. Edit.* **2005**, *44,* 6013-6015.

(18) Zhang, H.; Amro, N. A.; Disawal, S.; Elghanian, R.; Shile, R.; Fragala, J. High-throughput dip-pen nanolithography based fabrication of Si nanostructures. *Small* **2007**, 3, 81-85.

(19) Salaita, K.; Lee, S. W.; Wang, X. F.; Huang, L.; Dellinger, T. M.; Liu, C.; Mirkin, C. A. Sub-100 nm, centimeter-scale, parallel dip-pen nanolithography. *Small* **2005**, *1,* 940-945.

(20) Salaita, K.; Wang, Y.; Fragala, J.; Vega, R. A.; Liu, C.; Mirkin, C. A. Massively parallel dip-pen nanolithography with 55000-pen two-dimensional arrays. *Angew. Chem. -Int. Edit.* **2006**, *45,* 7220-7223.

(21) Bullen, D.; Chung, S.-W.; Wang, X.; Zou, J.; Mirkin, C. A.; Liu, C. Parallel dip-pen nanolithography with arrays of individually addressable cantilevers. *Appl. Phys. Lett.* **2004**, *84,* 789-791.

(22) Wang, X.; Liu, C. Multifunctional probe array for nano patterning and imaging. *Nano Lett.* **2005**, *5,* 1867-1872.

(23) Rosner, B.; Duenas, T.; Banerjee, D.; Shile, R.; Amro, N.; Rendlen, J. Functional extensions of Dip Pen Nanolithography[TM]: active probes and microfluidic ink delivery. *Smart Mater. Struct.* **2006**, *15,* S124-S130.

(24)   Lamb, B. M.; Westcott, N. P.; Yousaf, M. N. Live-cell fluorescence microscopy of directed cell migration on partially etched electroactive SAM gold surfaces. *ChemBioChem* **2008,** *9*(14), 2220-2224.

(25)   Bogenrieder, T.; Herlyn, M. Axis of evil: molecular mechanisms of cancer metastasis. *Oncogene* **2003**, *22,* 6524-6536.

(26)   Gibbs, J. T. Mechanism-based target identification and drug discovery in cancer research. *Science* **2000,** *287,* 1969-1973.

(27)   Iiizumi, M.; Liu, W.; Pai, S. K.; Furuta, E.; Watabe, K. Drug development against metastasis-related genes and their pathways: A rationale for cancer therapy. *Biochim. Biophys. Acta* **2008,** *1786,* 87-104.

(28)   Gomase, V. S.; Tagore, S.; Kale, K. V. Microarray: an approach for current drug targets. *Curr. Drug Metabol.* **2008,** *9,* 221-231.

(29)   Stoughton, R. B. Applications of DNA microarrays in biology. *Annu. Rev. Biochem.* **2005,** *74,* 53-82.

(30)   Sauter, G.; Simon, R.; Hillan, K. Tissue microarrays in drug discovery. *Nat. Rev. Drug Discovery* **2003,** *2*(12), 962-972.

(31)   Lamb, B. M.; Barrett, D. G.; Westcott, N. P.; Yousaf, M. N. Microfluidic lithography of SAMs on gold to create dynamic surfaces for directed cell migration and contiguous cell cocultures. *Langmuir,* **2008,** *24*(16), 8885-8889.

(32)   Westcott, N. P.; Yousaf, M. N. Synergistic microfluidic and electrochemical strategy to activate and pattern surfaces selectively with ligands and cells. *Langmuir,* **2008,** *24*(6), 2261-2265.

(33)   Lamb, B. M.; Westcott, N. P.; Yousaf, M. N. Microfluidic lithography to create dynamic gradient SAM surfaces for spatio-temporal control of directed cell migration. *ChemBioChem* **2008,** *9*(16), 2628-2632.

(34)   A-18, A-26, and A-52 (linear arrays of 18, 26, and 52 cantilevers, respectively), 2nd Generation Active Pens[TM], and 2D nano PrintArray (55,000 pen array). Available for use with the NSCRIPTOR[TM] DPN® system from NanoInk, Inc. (Chicago, IL, www.nanoink.net).